Ph.D. DISSERTATION

Chemoresistive gas sensing properties of two-dimensional materials

By

Yeonhoo Kim

February 2018

SEOUL NATIONAL UNIVERSITY

COLLEGE OF ENGINEERING

DEPARTMENT OF MATERIALS SCIENCE AND ENGINEERING

Chemoresistive gas sensing properties of two-dimensional materials

Advisor: Prof. Ho Won Jang

by

Yeonhoo Kim

A thesis submitted to the Graduate Faculty of Seoul National University in partial fulfillment of the requirements for the Degree of Doctor of Philosophy

Department of Materials Science and Engineering

December 2017

Approved

By

Chairman of Advisory Committee: Cheol-Hee Ahn

Vice-chairman of Advisory Committee: Ho Won Jang

Advisory Committee: Byung Hee Hong

Advisory Committee: Jong-Heun Lee

Advisory Committee: Donghwa Lee

Abstract

Semiconducting metal oxides, the most widely used materials in gas sensor applications, still have major problems of high power consumption, thermal safety issues resulting from use of external heaters, poor long-term stability and vulnerability to humidity. To overcome the obstacles, it is of great importance to explore alternative materials and improve their intrinsic properties by diverse strategies such as changing device structures, modification of surface chemistry by noble metal decoration or functionalization and understanding gas sensing mechanisms.

Among the alternative materials for gas sensing applications, two-dimensional (2D) materials including graphene, metal oxide nanosheets, and transition metal dichalcogenides (TMDs) are considered as leading candidates for next-generation gas sensors applicable to future electronics because of their unique properties such as transparency, flexibility, high surface-to-volume ratio, numerous active edge sites, and high sensitivity to gas molecules at room temperature. In addition, 2D materials satisfy special requirements for practical uses like low power consumption, low cost, small size, and easy integration into existing technologies. However, 2D materials have also few drawbacks such as poor selectivity, long response time, and irreversible gas sensing behaviors which must be overcome.

Therefore, this thesis presents chemoresistive gas sensing properties of self-activated graphene, chemically modified graphene oxide, and liquid-exfoliated MoS_2

possessing enhanced sensing characteristics. The sensing mechanisms are identified by first-principles calculations based on density functional theory (DFT).

First of all, self-activated gas sensing operation of all graphene gas sensors with high transparency and flexibility has been achieved using simple photolithography and graphene transfer processes on polymer substrates. The all-graphene gas sensors which consist of graphene for both sensor electrodes and active sensing area exhibit highly sensitive, selective, and reversible responses to NO_2 without external heating. The theoretical detection limit is calculated to be approximately 6.87 parts per billion (ppb). The sensors show reliable operation under high humidity conditions and bending strain, bending radius of 1 mm. In addition to these remarkable device performances, the significantly facile fabrication process enlarges the potential of the all-graphene gas sensors for use in the Internet of Things (IoT) and wearable electronics.

Secondly, we present a facile solution process and the room temperature gas sensing properties of chemically fluorinated graphene oxide (CFGO). The CFGO sensors exhibit improved sensitivity, selectivity, and reversibility upon exposure to NH_3 with a significantly low theoretical detection limit of ~6 ppb at room temperature in comparison to NO_2 sensing properties. The effect of fluorine doping on the sensing mechanism is examined by first-principles calculations based on density functional theory. The calculations reveal that the fluorine dopant changes the charge distribution on the oxygen containing functional groups in graphene oxide, resulting in the preferred selective adsorption and desorption of NH_3 molecules. We believe

that the remarkable NH_3 sensing properties of CFGO and investigation by first-principles calculations would enlarge the possibility of functionalized 2D materials for practical gas sensing applications.

Thirdly, we investigate the oxygen sensing behavior of MoS_2 microflakes and nanoparticles prepared by mechanical and liquid exfoliation, respectively. Liquid-exfoliated MoS_2 nanoparticles with an increased number of edge sites present high and linear responses to a broad range of oxygen concentrations (1–100%). The energetically favorable oxygen adsorption sites, which are responsible for reversible oxygen sensing, are identified by first-principles calculations based on density functional theory. This study serves as a proof-of-concept for the gas sensing mechanism depending on the surface configuration of 2D materials and broadens the potential of 2D MoS_2 in gas sensing applications

Keywords: Chemoresistive gas sensor, graphene, graphene oxide, MoS_2, two-dimensional materials, Functionalization, First-principles calculations

Student Number: 2013-20586

Yeonhoo Kim

Table of Contents

List of Figures

Chapter 1.

Chemoresistive gas sensing of two-dimensional materials: Principles and leading materials

1.1. Introduction

According to growing attention to next-generation technologies such as the Internet of Things (IoT) and smart devices, sensors providing massive information about the internal states of the objects and the external environment have become an attractive research area (Figure 1.1). Especially, gas sensor is considered as one of the most important components in the field of smart phone, health, security, building automation, and energy savings because transmits information about the presence and the concentration of a particular gas in ambient atmosphere. For practical use of gas sensors in future technologies, the sensor should meet special requirements such as low temperature operation, flexibility, transparency, low power consumption, and easy integration into existing electronics.

Semiconducting metal oxides have been extensively used over the past decades for chemoresistive gas sensor due to their advantages of low cost, small size, and high sensitivity to gas molecules. However, metal oxides have major drawbacks like thermal safety issues generated from external heaters, opacity, brittleness, and complex device structure which hinder the use of metal oxides in next-generation technologies such as IoT, smart devices, and wearable devices.

Recently, two-dimensional (2D) materials such as graphene, metal oxide nanosheets, and transition metal dichalcogenides are gaining increasing attention as prospective sensing materials because surfaces without bulk offer high surface-to-volume ratios, and surface configurations including dangling bonds on the edge sites and basal planes can be easily modified by decoration and functionalization process. Moreover, unique properties such as flexibility, high transparency, and easy fabrication process are suitable for high performance gas sensors.

In this thesis, chemoresistive gas sensing properties of 2D materials such as graphene, graphene oxide, MoS_2, and NbS_2 are presented, also the improvement of sensing properties of the 2D materials using functionalization and noble metal decorations are investigated. The thesis not only reports sensing performances of the sensors, but also demonstrates sensing mechanism depending on surface configurations, synthetic methods, and functional groups on surfaces. The observations on chemoresistive sensing properties of various 2D materials with different device designs and the investigations on sensing mechanisms will broaden the potential and lay the groundwork for 2D materials to be applied in practical applications such as the IoT and smart devices.

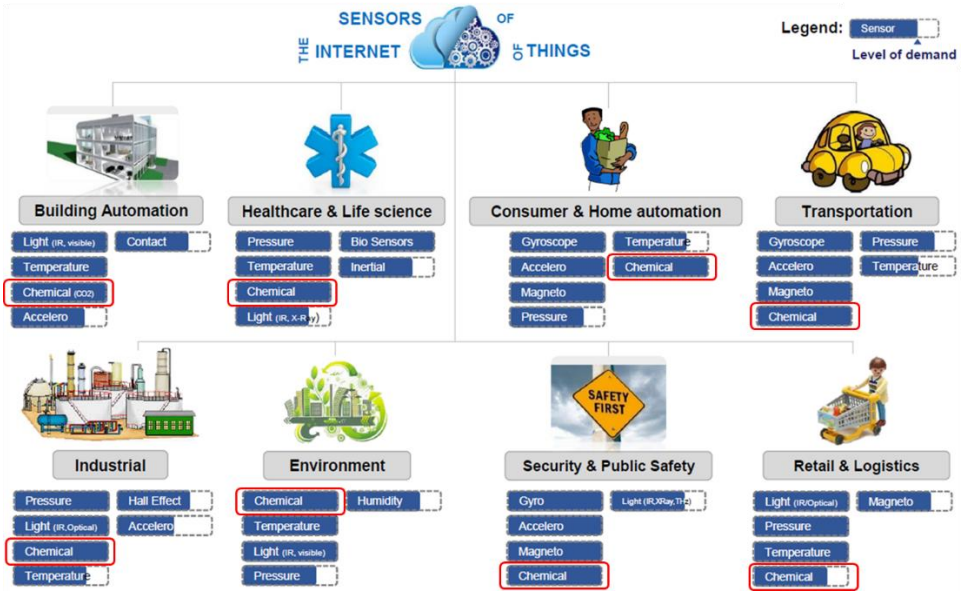

Figure 1.1. Potential use of chemoresistive gas sensors in future technologies such as the IoT and Smart electronics. (Yole development copyright 2014 – MEMS report)

1.2. Fundamentals of chemoresistive gas sensors

1.2.1. Principles of gas sensing mechanisms

Semiconductor gas sensors operate by detecting a change in their electrical conductivity arising from gas adsorption and desorption. In general, the change of electrical properties of the sensor caused by adsorption of gas molecules is primarily connected with the chemisorption of oxygen.[1-3] Molecular oxygen adsorbs on the surface of oxide materials by attracting an electron from the conduction band of the semiconductor as shown in the Equation (1).

$$O_2(gas) + e^- \Leftrightarrow O_2^-(adsorb) \quad (1)$$

At high temperature (100 – 400 ^oC), the oxygen ion molecules are dissociated into oxygen ion atoms with singly (O^-) or doubly (O_2^-) negative electric charges by trapping an electron again from the conduction band.

$$\frac{1}{2}O_2 + e^- \Leftrightarrow O_{ads}^- \quad (2)$$

$$\frac{1}{2}O_2 + 2e^- \Leftrightarrow O_{ads}^{2-} \quad (3)$$

The oxygen ions on the surface of oxide materials are very active, so undergoing chemical reaction with target gas molecule as shown in the Equation (4)

$$X + O_{ads}^{b-} \rightarrow X' + be^{-} \quad (4)$$

where *X* and *X'* is target gas molecule and out gas after chemical reaction, respectively. The *b* means the number of electrons.[4]

Based on charge carriers, semiconducting oxide materials can be classified into two groups: n-type and p-type materials. Target gas species can also be divided into two groups: oxidizing gas (electron acceptors) and reducing gas (electron donor). The chemical reaction causes change of the electric carrier concentration of oxide materials and thus change of gas sensor resistance. The change of gas sensor resistance depends on a type of oxide materials and target gas.

n-type semiconductor gas sensor

Since majority carriers in n-type semiconductors are electrons, the electrons in the conduction band of n-type semiconductors are removed by the adsorbed oxygen ions. This change in charge carrier concentration causes an increase of resistance of n-type semiconductor sensor at operating temperature. When the n-type semiconductor sensor is under reducing gas ambient, then a decrease in resistance of the sensor occurs. Conversely, an oxidizing gas cause depletion of charge carrying electrons, resulting in an increase in resistance.

p-type semiconductor gas sensor

A p-type semiconductor is one where the majority charge carriers are positive holes. When the oxygen ions are adsorbed on the surface, p-type semiconductor generates holes via the excited electrons from valence band resulting in decreasing the sensor resistance (opposite to n-type). The opposite effect of n-type is also observed showing an increase in resistance in the presence of reducing gas and a decrease in resistance in the presence of oxidizing gas (Figure 1.2).[4]

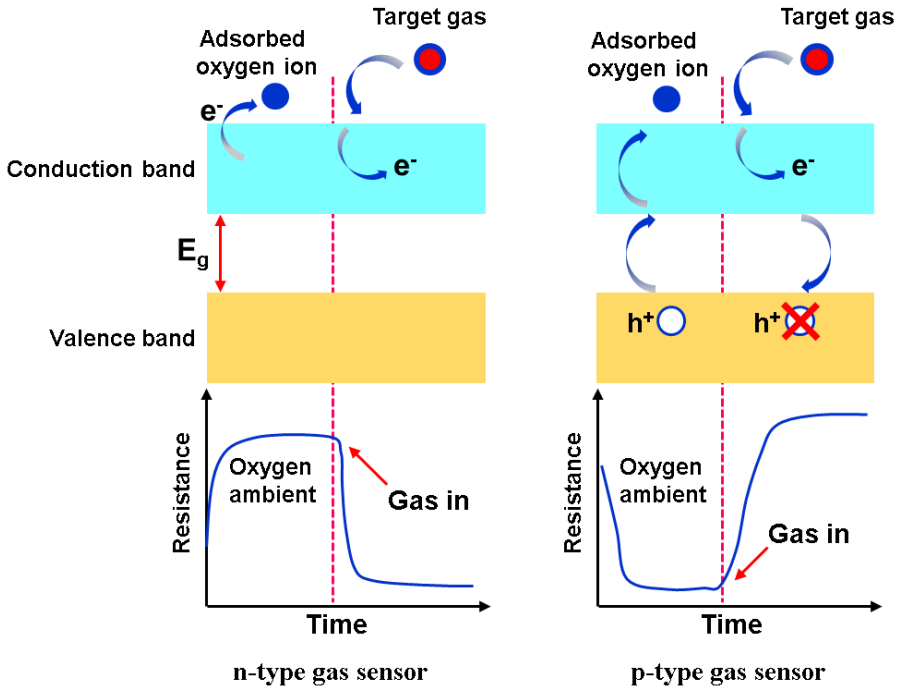

Figure 1.2. Schematic diagram for change of the sensor resistance upon exposure to reducing gas (target gas) in the cases of n-type and p-type semiconductor sensors.[4]

1.2.2 Parameters for gas sensor

In order to characterize sensor performance, some parameters are used. The most important and essential parameters for gas sensor and their definitions are listed below.

Response and Sensitivity

Response of semiconductor gas sensors is defined as the ratio of the resistance before and after sensing performance as shown the Equation (5);

$$Response = \frac{R_g}{R_a} \quad \text{or} \quad Response = \frac{R_a}{R_g} \tag{5.1}$$

$$Response\ (\%) = \frac{\Delta R}{R_g} \times 100\ (\%) \tag{5.2}$$

where R_a is the sensor resistance in ambient air, R_g is the sensor resistance in the target gas, and $\Delta R = |R_a - R_g|$.

Sensitivity (*S*) of gas sensor is a change of measured signal (i.e. response) per analyte concentration; it can be represented by slope of a calibration graph. This parameter is sometimes confused with the limit of detection.

Response and recovery time

Response time is the time it takes for sensor to undergo resistance changing from 10% to 90% of the value in equilibrium upon exposure to target gas. Recovery time is the time required for the sensor signal to return to 90% of its initial value upon removal of the target gas (Figure 1.3).

Limit of detection

Limit of detection is defined as the lowest concentration of the target gas that can be detected by the gas sensor under given conditions. Limit of detection is estimated via extrapolating of sensitivity versus concentration curve and using the following equation. (6)

$$Limit\ of\ detection = \frac{3.3 \times \sigma}{Slope\ (s)} \quad (6)$$

where σ is standard deviation of the regression line (Figure 1.4).[5]

Selectivity

Selectivity represents characteristics that determine whether a gas sensor can respond selectively to a specific analyte or a group of analytes.

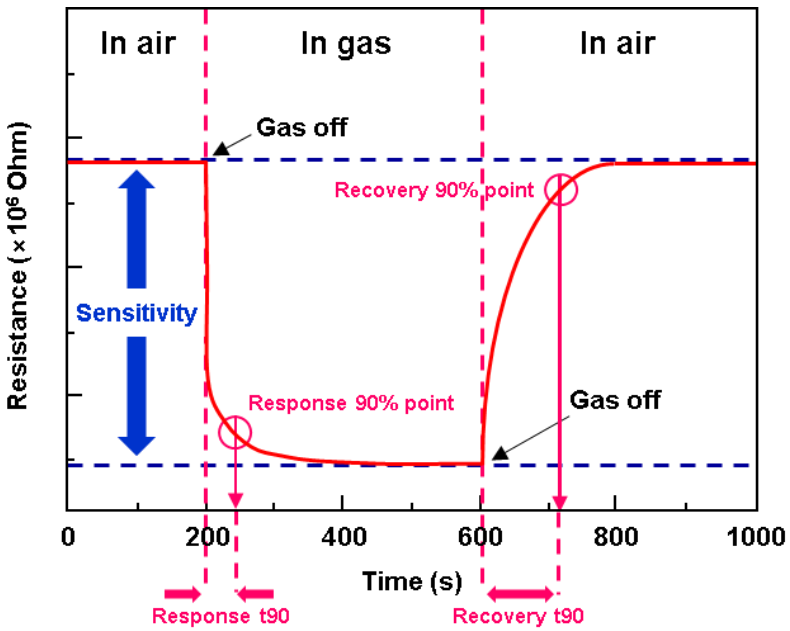

Figure 1.3. Definition of response and recovery time.

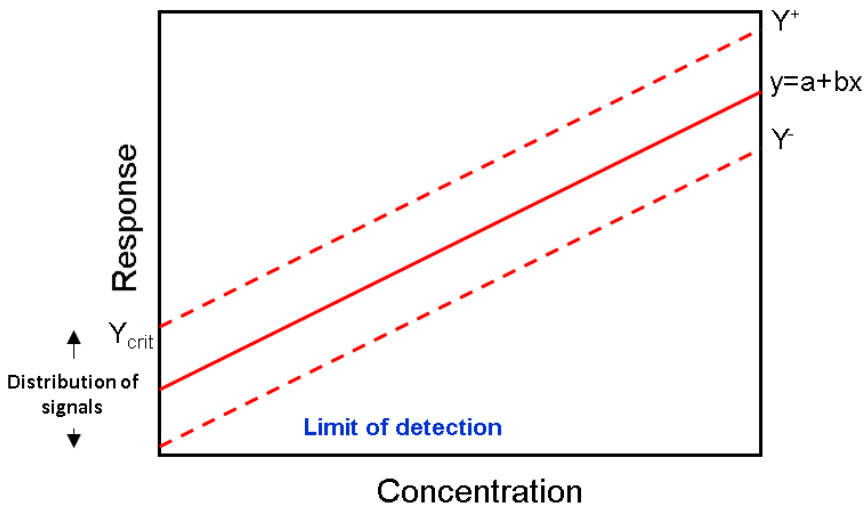

Figure 1.4. Limit of detection estimation. Extrapolating line (y=ax+b) and graphical deduction of limit of detection. The arrow on the y axis reflects the maximum future signal (responses) height.[5]

1.2.3. Three basic factors for chemoresistive gas sensing

Gas sensing properties of chemoresistive gas sensors are influenced by three basic factors, namely, receptor function, utility factor, and transducer function. Figure 1.5 shows the schematic diagram for concept of three basic factors. The receptor functionn refers to how the surface of sensing materials interact with gas molecules. It is possible to enhance sensing responses by modification of surface chemistry. Particularly, surfaces of 2D materials with numerous active edge sites and defects can be easily modified by simple functionalization and surface decoration processes, which enhance gas selectivity. Since the nanoscale noble metals have catalytic effect for preferred selective detection of specific gas species, they effectively enhance the receptor function. Utility factor is the ability of inner sites of sensing materials to access the target gas which have relevance to porosity of sensing layers and diffusion depth of gas molecules. For instance, the sensing ability can be lower when the sensing layer is too thick and the pore size is too small at the same time because gas molecules cannot pass through the sensing body. Transducer function expresses the ability to convert the signal generated by gas adsorption into an electrical signal like current, and resistances. Shape and configuration of sensing layers can tune transducer function. Hence, in order to achieve high gas sensing performance, the three basic factors should be properly controlled.

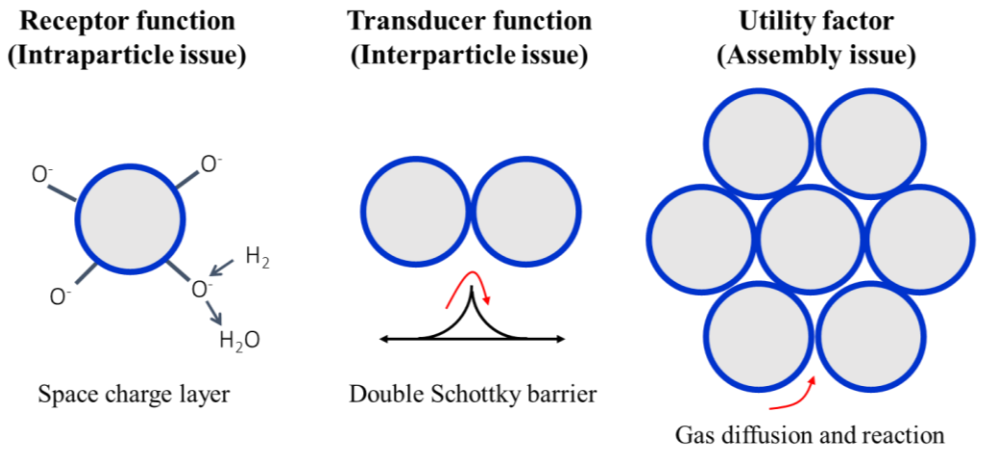

Figure 1.5. Schematic diagram of three basic factors in chemoresistive gas sensing

1.3. Two-dimensional materials for chemoresistive gas sensing

1.3.1. Graphene-based gas sensors

Graphene comprised of a monolayer of carbon honeycomb lattice is regarded as a prospective material for next-generation high performance sensing applications because every atom of graphene is a surface atom, electrical noise level is extremely low, and pristine natures can be easily modified *via* simple processes. For these reasons, many research groups have explored chemoresistive gas sensing applications based on graphene derivatives such as graphene, graphene oxide, and reduced graphene oxide.

Shedin *et al*.[6] reported capability of detecting individual gas molecules using microscale graphene gas sensor (Figure 1.6). In the report, Shedin *et al*. found that the initial undoped state could be recovered by annealing at 150 °C in vacuum (region IV in Figure 1.6). Repetitive exposure–annealing cycles showed no 'poisoning' effects of these chemicals (that is, the devices could be annealed back to their initial state). Lu *et al*.[7] reported reduced graphene oxide (rGO) gas sensor employing a back-gated field-effect transistor platform as the conducting channel. These sensors exhibited an increase in response when exposed to NO_2 and NH_3 in air (Figure 1.7). Fowler *et al*.[8] reported the development of monolayer graphene chemical sensor using spin coated graphene dispersions on interdigitated electrode arrays. The graphene layers

are reduced by anhydrous hydrazine from graphene oxide. Response curves of NO_2, NH_3, and 2,4-dinitrotoluene are exhibited for the sensors (Figure 1.8.). Dan *et al*.[9] demonstrated that the contamination layer chemically dopes the graphene, enhanced carrier scattering, and acted as an absorbent layer that concentrates analyte molecules at the graphene surface, thereby enhancing the sensor response.

Above this, there are many studies on chemoresistive gas sensors based on graphene derivatives.[10-13] Although the studies attempt to achieve high performance gas sensors with high sensitivity, reversibility, and selectivity, it still remains an unsolved problem. Sluggish response and recovery, high power consumption, complex structure, inflexible and non-transparent natures of the devices are hindering the practical use of the sensors. Hence, I report diverse approaches like self-activation, functionalization, surface decoration, and the first-principles calculations for investigating sensing mechanisms to enhance sensing properties of graphene-based materials.

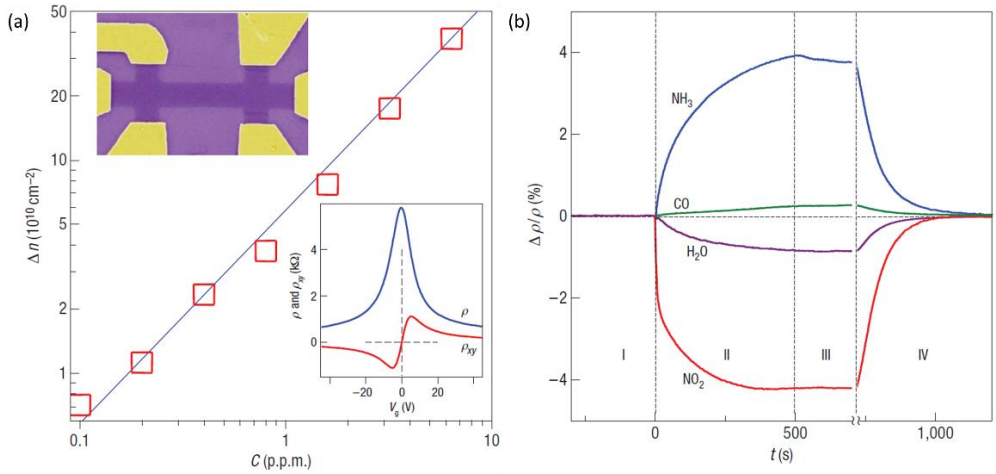

Figure 1.6. Sensitivity of graphene to chemical doping. (a) Concentration of chemically induced charge carriers in single-layer graphene exposed to different concentrations of NO_2. Upper inset: SEM. Lower inset: Characterization of the graphene device by using the electric-field effect. (b) Changes in resistivity upon exposure to various gases of 1 ppm.[6]

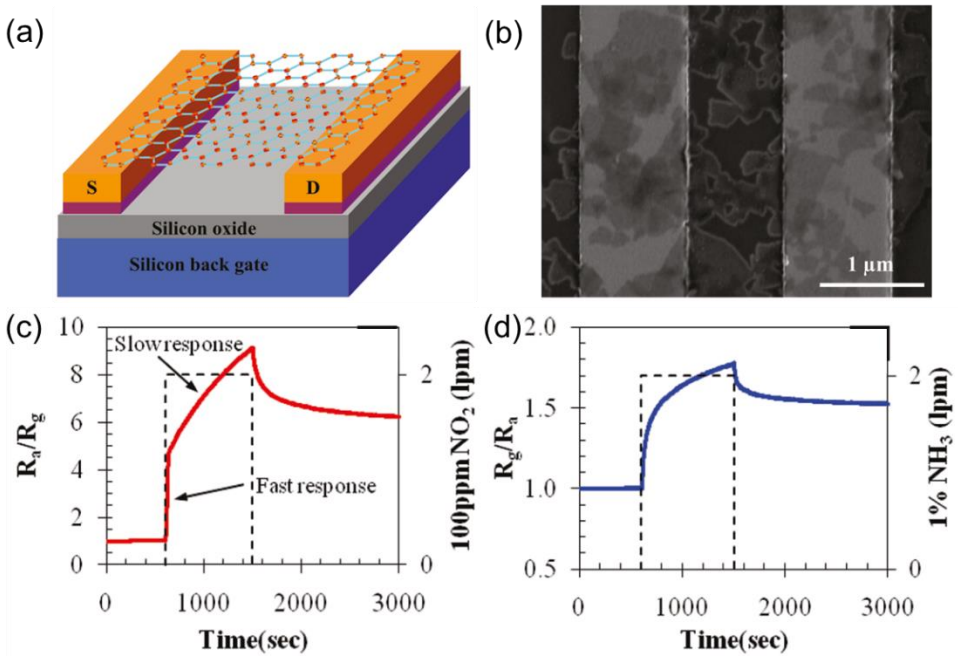

Figure 1.7. (a) Schematic of the R-GO device with an FET platform (b) SEM image of a sensing device composed of R-GO platelets that bridge neighboring Au fingers. (a) Representative dynamic behavior of R-GO sensors for (c) 100 ppm NO_2 and (d) 1% NH_3 detection.[7]

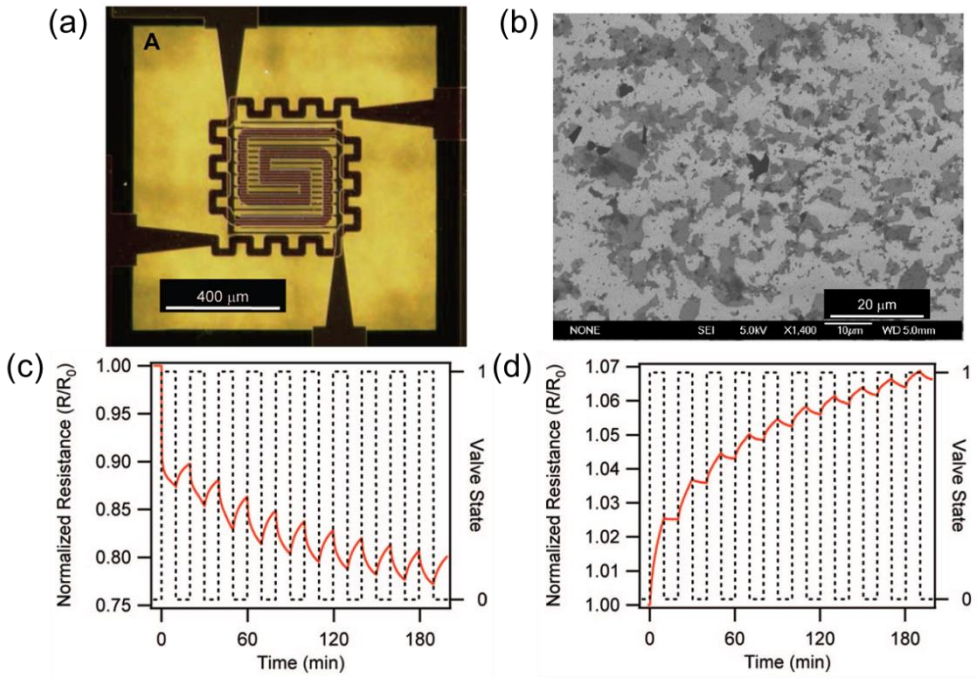

Figure 1.8. (a) Photograph of the sensor device. (b)Spin-coated graphene film on the chemical sensor. Response curves upon exposure to (c) NO_2 and (d) NH_3.[8]

1.3.2. Transition metal dichalcogenides

According to the growing attention on two-dimensional materials, transition metal dichalcogenides (TMDs) such as MoS_2, SnS_2, WSe_2, and $NbSe_2$ have been explored for gas sensing materials.[14-21] On the contrary to graphene-based materials, TMDs have other advantages such as semiconducting nature, and numerous active edge sites.

Ou *et al*.[14] demonstrated reversible and selective sensing properties of 2D SnS_2 flakes to NO_2 exposures at low operating temperatures of less than 160 °C (Figure 1.9). Medina *et al*.[15] reported wafer-scale growth of WSe_2 monolayers and sup-ppb level of NO_2 detection using Hybrid WO_x/WSe_2 films prepared by plasma assisted selenization process. Late *et al*.[16] reported gas sensing behavior of few MoS_2 layers using transistor geometry. The sensor exhibited excellent sensitivity, and recovery. The sensing mechanism was investigated by DFT calculations (Figure 1.10). Cho *et al*.[20] presented chemoresistive gas sensing properties of 2D $NbSe_2/WSe_2$ layered junction which is applicable on wearable devices. They showed high endurance to mechanical bending and doing laundry as well.

As described above, many researchers have been exploring chemoresistive gas sensors based on TMDs because they show impressive chemoresistive sensing characteristics such as higher selectivity, sensitivity, and reversibility

comparing with other 2D materials. Despite the significant potential to achieve high performance gas sensors, proof-of-concepts studies on gas sensing mechanisms of 2D TMDs are not well defined. For the reasons, this thesis reports here the sensing properties and sensing principles of TMDs using both of experiments and theoretical studies.

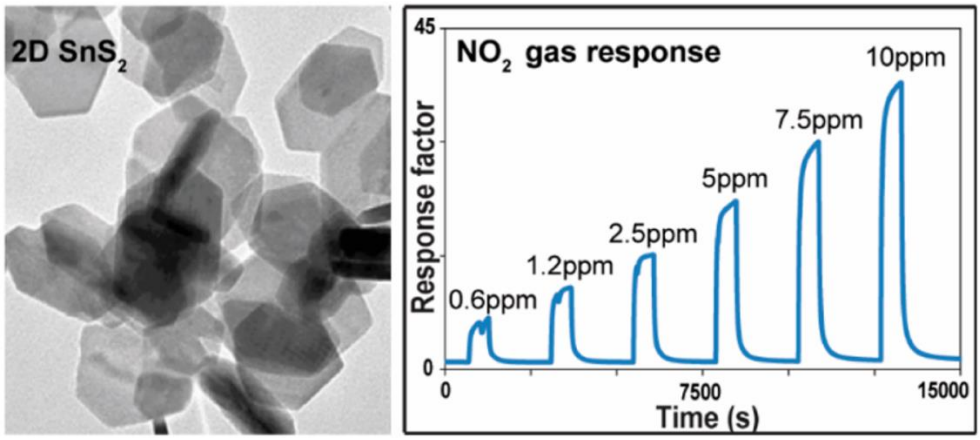

Figure 1.9. TEM image of 2D SnS_2 and the sensing responses to NO_2 gas.[14]

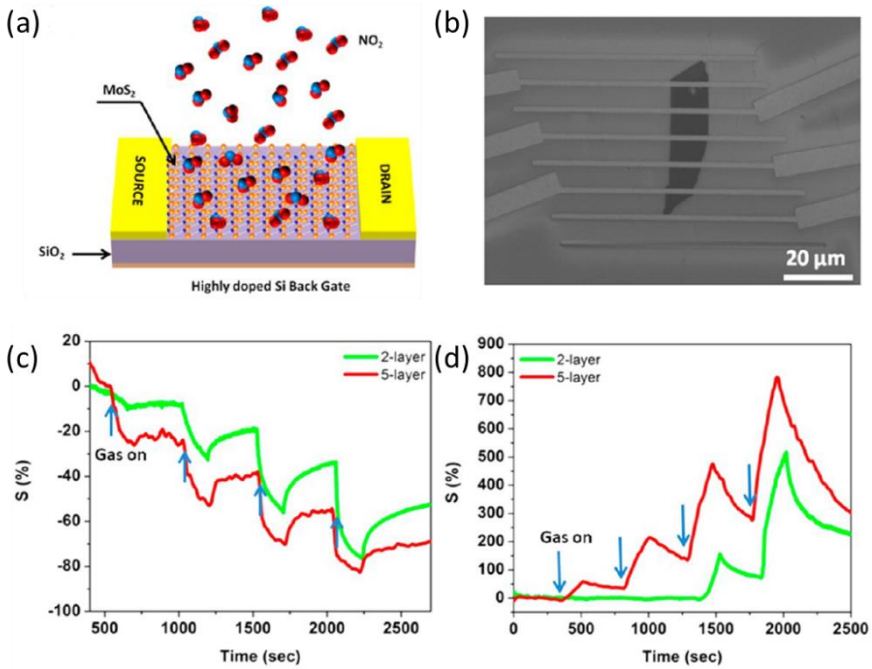

Figure 1.10. (a) Schematic of the MoS_2 transistor-based NO_2 gas-sensing device. (b) SEM image of two-layer MoS_2 transistor device. Sensing curves to (c) NH_3 and (d) NO_2.[16]

Chapter 2

Self-activated Transparent All-Graphene Gas Sensor with Endurance to Humidity and Mechanical Bending

2.1. Introduction

Internet of things (IoT) refers to the interconnected network of physical objects that contain embedded technology to exchange information or processed data with operators, manufacturers, or other connected devices.[22] One of the most important constitutes of the IoT is sensors, as they offer massive information about the internal states of the objects and the external environment.[23] Gas sensors that transmit information about the presence and the concentration of a particular gas in the ambient have attracted enormous attention for the key to innovations in the fields of comfort, security, health, environment, and energy savings.[3, 24-26] Gas sensors required by the IoT should meet special requirements such as low power consumption, low cost, small size, and easy integration into existing technologies.[27] Among various types of gas sensors, chemoresistive gas sensors based on semiconducting materials have been considered as suitable candidates for the IoT due to low cost and small size.[27-30] Gas sensors based on nanostructured semiconducting metal oxides lead to high responses to various gases, but they operates with external heaters for maintaining the materials at elevated temperatures.[27, 31] The use of an external heater not only increases the power consumption but also causes thermal safety problem, hindering practical applications for the IoT.

Graphene, a two dimensional (2D) carbon monolayer crystal, is considered as a candidate material for the next-generation high-performance gas sensors operating at room temperature, since the surface without bulk is highly sensitive to the adsorption and desorption of gaseous molecules.[6-13, 32] However, the main drawback of graphene-based sensors is extremely sluggish response and incomplete recovery to the initial state after a sensing event, thus making the sensors incapable of producing repeatable sensing signals even upon exposure to the same analyte concentration at room temperature.[7, 8, 33-35] The long response and recovery time of the graphene-based sensors originates from the slow process of NO_2 adsorption on the graphene surface at room temperature.[36, 37] Fowler *et al.*[8] showed that a gas sensor based on reduced graphene oxide required an elevated operation temperature of 149 ^{o}C for reversible sensor response and recovery. In addition to the sensing material itself, stable contact between graphene and sensor electrodes is also required for reliable sensor operation. When chemical vapor deposited graphene is transferred to sensor electrodes or reduced graphene oxide flakes are drop-casted on sensor electrodes, weak binding between graphene and noble metals such as Pt and Au can be the origin of low signal-to-noise ratios in graphene-based gas sensors. To fulfill these requirements, the development of self-

activated gas sensors consisting of only graphene for both active area and sensor electrodes is vital.

Here we report self-activated all graphene gas sensors which can detect NO_2 reversibly without external heating. The sensing properties of the all graphene gas sensors are significantly enhanced by self-activation, Joule heating in a micro patterned graphene channel that depends on sensor geometry and applied bias voltage. The self-activation is clarified by infrared imaging and comparison with external heating. The voltage dependence of sensor response to NO_2 is presented. We also present the linearity between NO_2 concentration and the sensor response and the high selectivity of the sensor response to NO_2. As both active sensing area and sensor electrodes consist of only graphene, the fabrication process is quite simple and the sensors fabricated on polyimide (PI) substrate are entirely transparent and highly flexible.

2.2. Experimental section

2.2.1. Graphene synthesis, and multiple stacking processes

Graphene was synthesized on a Cu foil (purity: 99.99%) using thermal chemical vapor deposition method at 1,000 °C with hydrocarbon source (CH_4, 30 sccm) and hydrogen (H_2, 3 sccm). After one side of the as-synthesized sample was coated with PMMA, the graphene on the other side was removed

by oxygen plasma using the reactive ion etcher. The Cu foil was etched with ammonium persulfate solution and the graphene was subsequently rinsed with distilled water. The floating graphene was transferred on another as-synthesized sample to fabricate multilayered graphene. Finally, PMMA supporting polymer on the graphene was removed by acetone treatment.

2.2.2. Graphene patterning and transferring process

3LG on the Cu foil was patterned by photolithography and O_2 plasma treatment (6 sec) with 50 W plasma power. Additional PMMA layer was coated on top of the patterned graphene to transfer the sample on a desired substrate. The patterned graphene with polymer was transfer on a transparent PI film and the sample was soaked in acetone to remove the supporting polymer (PMMA and PR) layers.

2.2.3. Sensor measurements

The gas sensing properties of the fabricated graphene sensors were measured without external heating. As the flow gas was changed from dry air to a calibrated test gas (balanced with dry air, Sinjin Gases), the variation in sensor resistance was monitored using a source measurement unit (Keithley 2365B). A constant flow rate of 1000 sccm was used for dry air and the test gas. The sensor resistance was measured under a DC bias voltage of 1–60 V. The response of the sensors ($\Delta R/R_0$) was accurately determined by measuring the

baseline resistances of the sensors in dry air and the fully saturated resistances after exposure to the test gas. Gas flow was controlled using mass flow controllers, and all measurements were recorded to a computer over a GPIB interface. The current–voltage characteristics of the fabricated sensors were measured to check the contribution of the contact resistance to the overall performance.

2.3. Result and discussion

2.3.1. Fabrication process, optical and electrical properties

Three layer graphene (3LG) was grown on a Cu foil using chemical vapor deposition (CVD) method. The 3LG was patterned directly on the Cu foil because of difficulties in patterning on a flexible polymer substrate. Polymethylmethacrylate (PMMA) was coated on top of the patterned graphene to transfer the sample on a target substrate. The Cu foil was etched using $FeCl_3$ and the patterned graphene with PMMA was transferred on a PI substrate (Figure 2.1a). The PI substrate was employed since it is transparent, flexible, and thermally more stable than other polymer substrates. The key idea of this work is inducing current crowding in the micropatterned narrow electrical channel of 3LG on the transparent and flexible substrate, resulting in the self-activation. Such a self-activation in the narrow graphene channel is

analogous to Joule heating in typical platinum-based micro heaters. Figure 2.1b shows optical microscopic images of patterned graphene with the narrow electrical channel of 5 μm width and 5 mm length on a Cu foil. The width of the channel was limited to 5 μm because the channels under 5 μm could not be made reproducibly in our technique.

The final devices are entirely transparent and flexible as shown in the photograph of a final sensor device on a PI substrate in Figure 2.1c., which have not been achieved yet since typical sensors contain non-transparent and non-flexible parts such as sensor electrodes or heaters.[38, 39] The transmittance spectra of a PI substrate and the substrate with 3LG over the wavelength range of 300−800 nm are shown in Figure 2.1d. The transmittance of the PI substrate and the substrate at 550 nm with 3LG is ~88% and ~80%, respectively. Owing to this high transmittance, the fabricated sensors are barely visible, suggesting that the sensors can be applied to next generation transparent electronics. The as-grown (non-patterned) and patterned 3LG was characterized by Raman spectroscopy. The absence of a measurable D-band in Figure 2.1e denotes the low-defect density of the 3LG.[40] Since low-energy binding sites, like the carbon sp^2-bonds, result in a fast gas reaction and high-energy binding sites such as point defects offer a slow gas reaction, superior sensing performance of our device is expected by the absence of D-band.[41] As the sensors are

composed of only graphene, there is no heterogeneous junction between sensor electrodes and active sensing layer so that the both patterned (5 μm × 5 mm sensing area) and non-patterned (1 cm × 1 cm sensing area) sensors display linear current-voltage (*I*-*V*) characteristics as shown in Figure 2.1f. Such an Ohmic behavior is very important for reliable sensor performance because resistance changes in the active region can be exactly measured without attenuation. The similar resistances of 10 patterned sensors indicate the reproducibility of the fabrication procedure (Figure 2.2). The length of the patterned graphene channel was fixed to be 5 mm, which is moderate for making the sensor resistance appropriate for chemoresistive gas sensing.

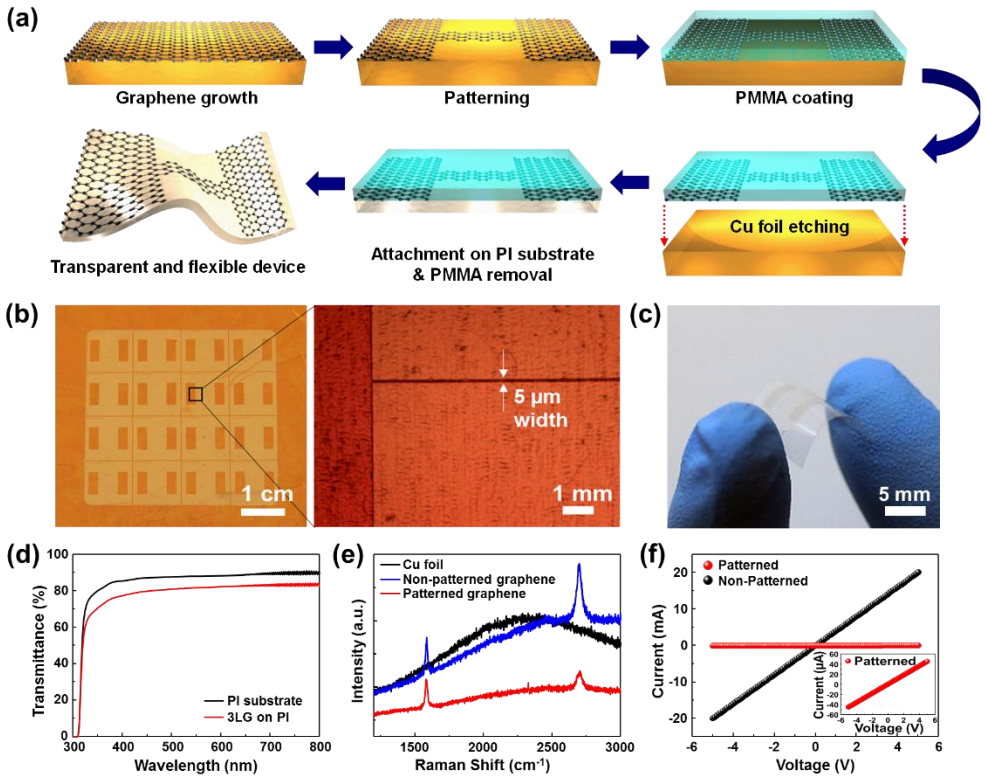

Figure 2.1. (a) Fabrication procedure of an all graphene sensor. (b) Optical microscopic images of patterned graphene on a Cu foil. (c) Photograph of a fabricated all graphene gas sensor on a PI substrate. (d) UV-Vis transmittance spectra of PI substrate and final device. (e) Raman spectra of a Cu foil and graphene on the Cu foil before and after patterning. (f) Current-voltage characteristics of non-patterned and patterned all graphene sensors.

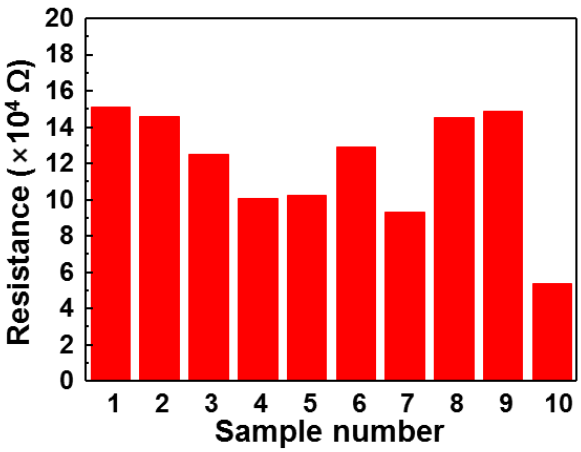

Figure 2.2. Baseline resistances of 10 different all graphene sensors.

2.3.2. Gas sensing properties of all-graphene sensor

Figure 2.3a shows dynamic sensing transients of the patterned and non-patterned all graphene sensors. The devices were exposed to three consecutive pulses of 5 ppm NO_2 balanced with dry air. The patterned graphene sensor shows a dramatic enhancement in response with increasing the bias voltage. Since the interval time between each exposure is not enough for full recovery, the base resistance is slightly shifting for multiple exposures. The response of the patterned graphene sensor (defined here as $(R_{gas} - R_{air})/R_{air} \times 100\%$, where R_{air} and R_{gas} denote the resistance of the sensor in dry air and the resistance of the sensor by exposure to the test gas) is 4.47% at 1 V and 12.49% at 60 V. In the previous works,[6, 33, 42-45] the graphene-based gas sensors show response about ~5% to 1–20 ppm NO_2 at room temperature, while our device exhibits response of ~12% to 5 ppm NO_2. With increasing the bias voltage, the sensor also shows improved response and recovery (Figure 2.4a, b). For the non-patterned sensor, measurements were only available with the bias voltage under 10 V due to the power limit of the source measurement unit (Keithley 2635B), and the response to 5 ppm NO_2 is not enhanced by applying 10 V. The response of the non-patterned sensor is 4.67% and 4.35% at 1 V and 10 V, respectively. The non-patterned sensor shows a larger deviation of the responses than that of the patterned graphene sensor to the consecutive three

time pulses of 5 ppm NO_2 (Figure 2.4c). In contrast, the deviation of continuative responses to 5 ppm NO_2 was relatively small for the patterned sensor. Because the patterned sensor reached the resistances very close to the original baseline value after each exposure to NO_2, the patterned sensor could have the smaller deviation in the responses compared with that for the non-patterned sensor. This reliable and repeatable sensing performance of the patterned sensor holds promise in practical applications. For the patterned sensor, response and recovery time (response t_{50} and recovery t_{50} are the time for the sensor's resistance to reach 50% of its steady state value in the gas response and the recovery to original state, respectively) were calculated at each applied voltage. By increasing the bias voltage from 1 V to 60 V, the response t_{50} decreases from 328 s to 89 s and the recovery t_{50} decreases from 1941 s to 579 s (Figure 2.4d).

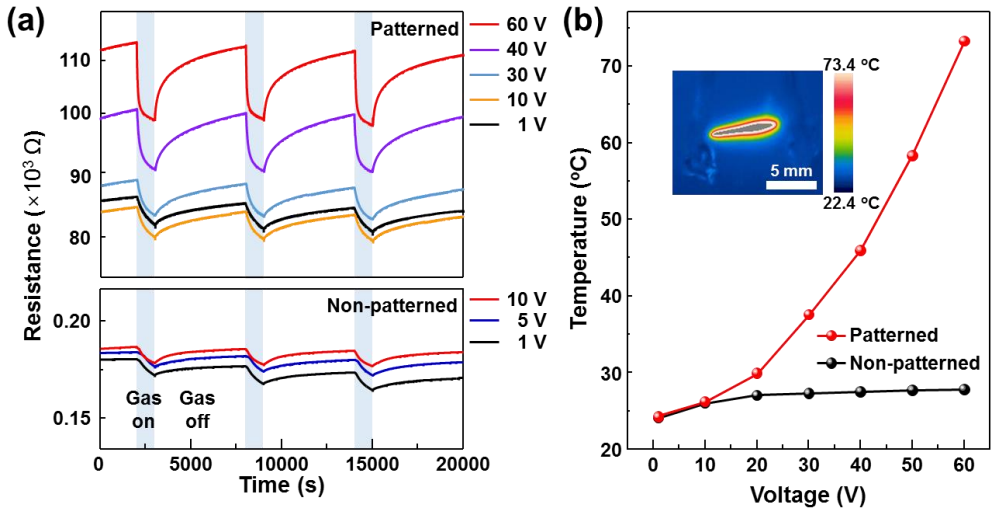

Figure 2.3. (a) Response curves of patterned and non-patterned graphene sensors to three pulses of 5 ppm NO_2. (b) Thermographic image and thermal characteristics with different bias voltages.

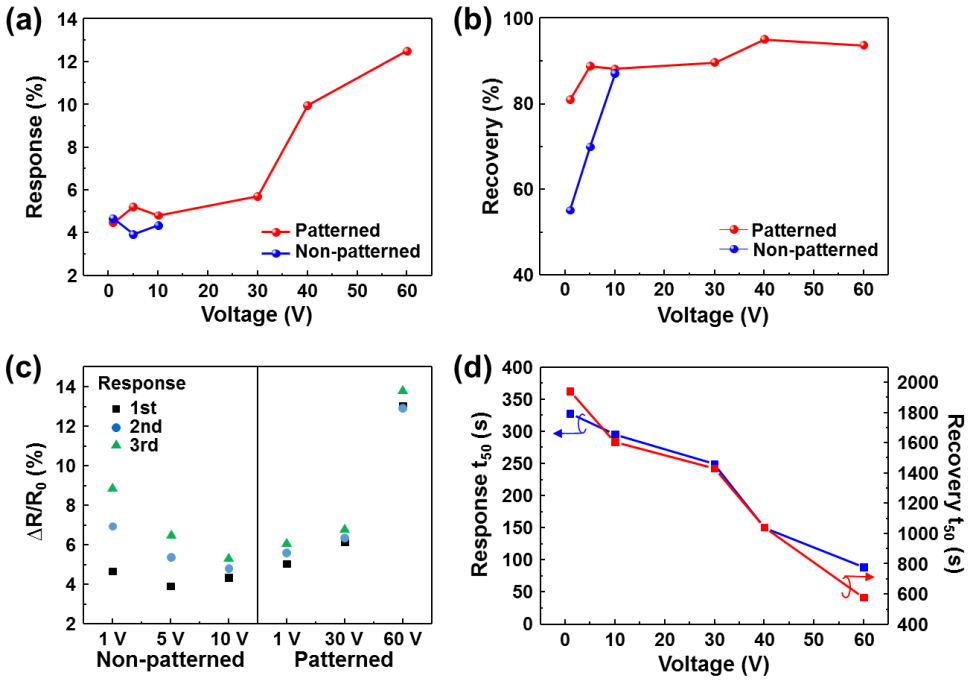

Figure 2.4. (a) Response characteristics of patterned and non-patterned graphene sensor with various applied voltages. (b) Recovery characteristics of patterned and non-patterned graphene sensor with various applied voltages. (c) Response stability to three repeated pulses of 5 ppm NO_2 (d) Response and recovery time (t_{50}) analysis as a function of applied bias voltage for the patterned graphene sensor.

2.3.3. Influence of self-activation on gas sensing properties

It is noteworthy that the baseline sensor resistances increase for both the patterned and non-patterned sensors when the applied voltage is increased from 1 to 60 V. One relevant scenario to explain this result is that the temperature of the active regions in the sensors increases with increasing the bias voltage. Since graphene is metallic, the resistance of the material increases with increasing temperature, which is an indirect evidence of self-activation in the sensors. To confirm the voltage-dependent self-activation, thermographic images of the sensors were obtained with an infrared camera (FLIR SC660). The temperature of the active region in the patterned sensor was measured to 73.4 ^{o}C at the applied bias voltage of 60 V (ODA Technologies EX200-6). On the contrary, the temperature of the non-patterned sensor stays below 30 ^{o}C even at 60 V (Figure 2.3b). In the previous work, graphene-based gas sensors required the minimum temperature of 149 ^{o}C for the fast response and full recovery.[8] However, in this work, the fast response and full recovery of the patterned graphene sensor were observed at the relatively low temperature of 73.4 ^{o}C. We presumed that the actual temperature on locally heated spots would be higher than the apparent temperature of 73.4 ^{o}C. Hence, additional experiments were conducted to prove the presumption.

The response of the non-patterned graphene sensor to 5 ppm NO_2 was measured at various temperatures from 27 to 180 ^oC with the constant applied voltage of 1 V (Figure 2.5a). The sensor resistance increases to ~240 Ω with increasing temperatures as shown in the patterned graphene sensor with increasing bias voltage. As the temperature increases, the sensor shows faster response and improved recovery. The non-patterned sensor exhibits full recovery to the original state at 180 ^oC. However, the response time of the non-patterned sensor at 180 ^oC looks still longer than that of the patterned sensor operating at 60 V. To clarify this, the response curves of the patterned and non-patterned sensors were fit by the exponential decay formula, $\Delta R/R_0\,(t) = \exp(-t/\tau) + R_\infty$, where τ is the time constant and R_∞ the steady state resistance, as shown in Figures 2.5b,c. For each fit curve, we extracted the τ value and plotted the τ values as a function of the applied bias voltage for the pattern sensor (Figure 2.5d) and temperature for the non-patterned sensor (Figure 2.5e). The τ value gradually decreases with the voltage for the pattered sensor, while it exponentially decreases with temperature for the non-patterned sensor. However, the τ value of the patterned sensor with 60 V (82 s) is still lower than that of the non-patterned sensor at180 ^oC (168 s). From this result, it is suggested that imperceptible heating over 180 ^oC occurred at local spots on the patterned graphene sensor by applying 60 V. We believe that the local

heating spots are invisible within the resolution of the infrared camera. Recently, Yasaei *et al*.[46] reported the influence of graphene grain boundaries on gas sensing properties of graphene. They showed that the grain boundaries acting as dominant gas adsorption sites in polycrystalline graphene have higher resistances and ~300 times higher sensitivity than a single-crystalline graphene grain. When the voltage is applied to the patterned sensor, voltage drop occurs mainly in the narrow channel. Since the CVD graphene is polycrystalline, the narrow channel is a series connection of graphene grains and grain boundaries. As a result, voltage drop across the grain boundaries is much larger than that through the grains. Therefore, Joule heating could be predominant in the grain boundaries, which are attributed to the local heating spots in the patterned all graphene sensor. Further studies are needed to investigate the influence of graphene grain boundaries for adsorption and desorption of gas molecules in our graphene sensors.

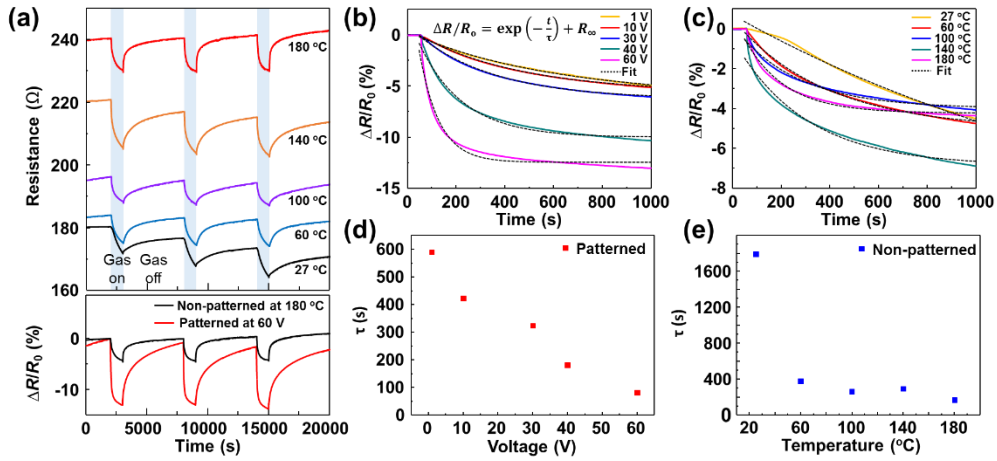

Figure 2.5. (a) Response curves of the non-patterned sensor to three pulses of 5 ppm NO_2 at different temperatures (top) and comparison of the response curve at 180 ^oC with that of the patterned sensor at 60 V (bottom). (b) Normalized response curves with fits to the exponential decay formula for the patterned and (c) non-patterned sensors. (d) Decay time, τ, as functions of applied bias voltage for the patterned sensor and (e) temperature for the non-patterned sensor.

To evaluate the detection limit of the patterned graphene sensor to NO_2 under the self-activated state, the response of the sensor was measured to 1−10 ppm NO_2 as shown in Figure 2.6a. The $\Delta R/R_0$ values proportionally increases with increasing the NO_2 concentration. The base resistance is shifting with increasing the NO_2 concentration because the longer time is required for full recovery. The response values were plotted as a function of the gas concentration in Figure 2.6b. A simple linear regression fit was applied to find the linear relationship between the responses and the concentrations. The linear regression equation is expressed as $y = 1.067x + 5.01$, where y is the response, x is the concentration of NO_2. The measure of goodness-of-fit of the linear regression, r^2, was calculated to be 0.943. The responses of the sensor are 5.13, 8.04, 11.35, 13.36, and 14.94 to 1, 2.5, 5, 7.5, and 10 ppm NO_2. Although the NO_2 concentration of 1 ppm was the lowest examined experimentally in the present study, the theoretical detection limit was calculated to be approximately 6.87 parts per billion (ppb).[5, 47] (see Supporting Information for details). This sub-ppb level of the detection limits to NO_2 suggests its potential for use in various applications such as environmental monitoring and breath analysis, especially for diagnosing asthma. For the practical use of chemoresistive sensors in various applications, the water vapor poisoning effect has to be overcome. Typically chemoresistive sensing

properties of gas sensors based on semiconducting metal oxides are deteriorated in humidity condition.[48, 49] We have measured dynamic sensing transients of the patterned graphene sensor to 5 ppm NO_2 in dry (0% relative humidity) and humid (50% relative humidity) atmosphere (Figure 2.6c). Although the sensing properties were slightly deteriorated in terms of response and recovery, the degradation was less than ~5% in the humidity condition, which has not been reported for graphene-based gas sensors. It is noted that the degradation level is much lower than those of semiconducting metal oxide gas sensors which were depicted in previous works.[50, 51] This result suggests that the self-activation plays a role in reducing the humidity effect.

Figure 2.6d shows responses ($|\Delta R/R_0|$) of the patterned all graphene sensor to 5 ppm NO_2, 50 ppm NH_3, 50% relative humidity air, 50 ppm C_2H_5OH, and 50 ppm CH_3COCH_3 at the applied voltage of 60 V. Even the NO_2 concentration is the lowest as 5 ppm, the sensor shows the highest response to NO_2 (~13%). The responses to 50 ppm NH_3, C_2H_5OH, CH_3COCH_3, and 50% RH air are 5.4, 1.71, 0.17, and 0.9%, respectively. The dynamic sensing transients to each gas are displayed in Figure 2.7. This result demonstrates the high selectivity of the all graphene sensor to NO_2.

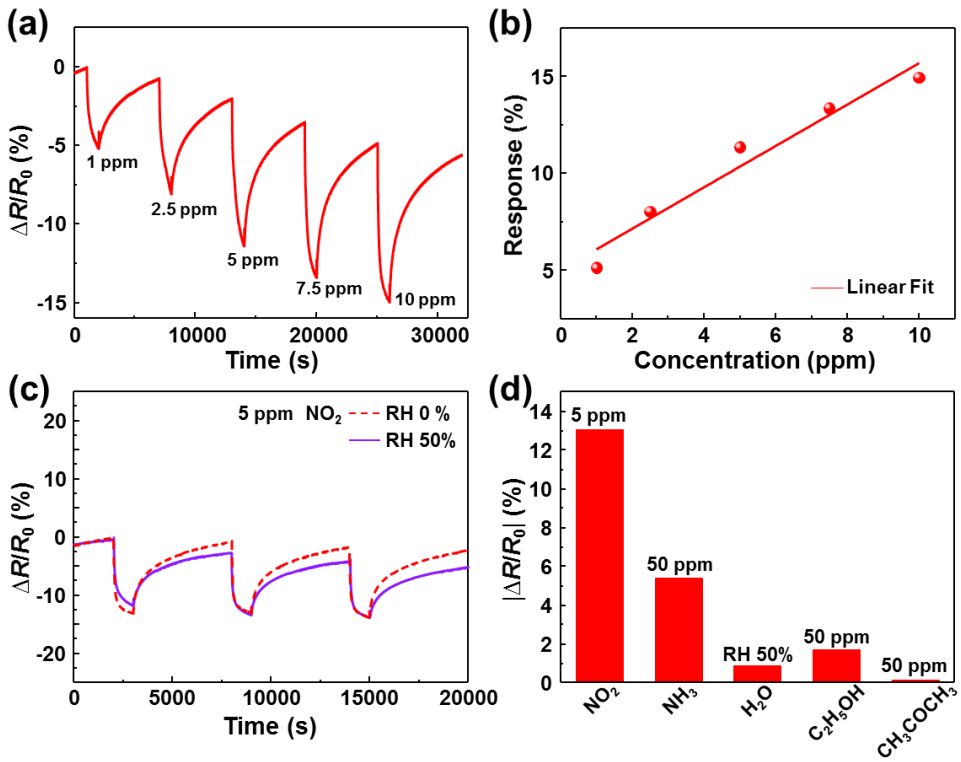

Figure 2.6. (a) Response curves to different NO_2 concentration at 60 V. (b) Linear fit of the responses as a function of NO_2 concentration at 60 V. (c) Response curves upon exposure to NO_2 5 ppm in 0% and 50 % of relative humidity atmosphere at 60 V. (d) Responses of the all graphene sensor to 5 ppm NO_2, 50% wet air, 50 ppm ammonia, ethanol, and acetone at room temperature 60 V.

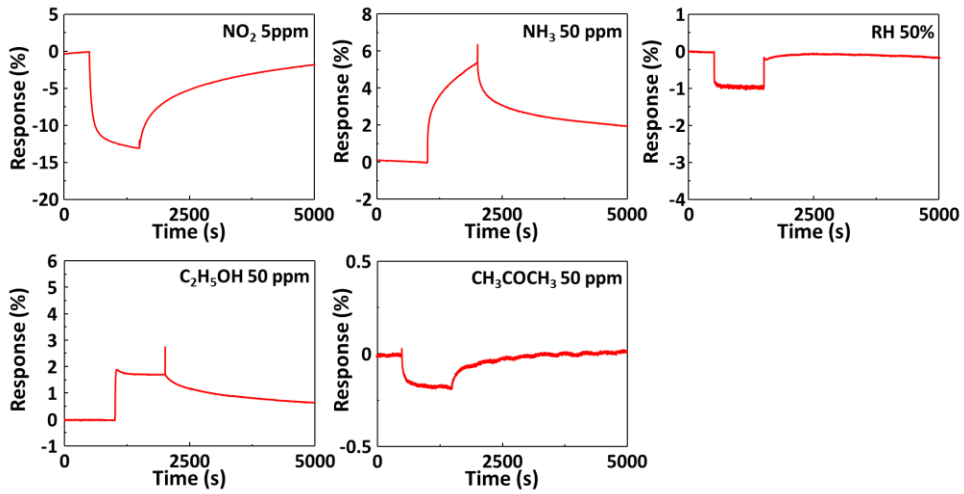

Figure 2.7. Response curves of the patterned graphene sensor to 5 ppm NO_2, 50% RH air, 50 ppm ammonia, ethanol, and acetone gases at 60 V.

2.3.4. Sensing performance with endurance to mechanical bending

The sensing performance with high bending strain was also investigated, which broadens the applications of the possibility of the self-activated all graphene gas sensor applications to wearable electronics. To validate stable sensing operation under bending strain, the patterned graphene sensor was attached on two ball pen leads (bending radius of 1 mm). The bent sensor was fixed on a glass substrate and then was loaded to the chamber of the gas sensing measurement system (Figures 2.8a,b; see Figure 2.9. for detailed photographs of the bent sensor). Figure 2.8c shows the sensing curves of the all graphene sensor without and with the bending strain (flat and bent). When the sensor was bent, the sensor still worked owing to the high flexibility of the graphene.[52] It is known that the resistance of graphene is increased by mechanical bending strain.[53, 54] As a result, the lowered current density in the micro patterned graphene channel can weaken the self-activation that influences the sensing response. Despite this, the bent sensor shows only ~3% degradation in the response compared with the flat sensor. In our best knowledge, nobody has shown gas sensors working under such a high bending strain (bending radius of 1 mm).

In addition to resistance to humidity condition and stability over long-term operation, low power consumption is required for practical applications of the all graphene sensor as a component in handheld IoT devices such as mobile phones, smart watches, and tablet personal computers. To handle this issue, we have measured the power consumption of the sensor. By increasing the applied voltage from 1 to 60 V, the power consumption increases from 12 μW to 14.2 mW (Figure 2.10). These values are comparable or even lower than the power consumption of micromachined thin film chemoresistive sensors (5−200 mW).[55, 56] We believe that lower power consumption of the self-activated all graphene sensors can be obtained by nanostructuring or functionalizing the graphene channel and making the narrow channel free-standing, which enable the self-activation with reduced voltages or currents. Since the fabrication process of the all graphene sensors is very simple, this superior performance of the all graphene sensor demonstrates the feasibility of embedding them into portable and wearable devices.

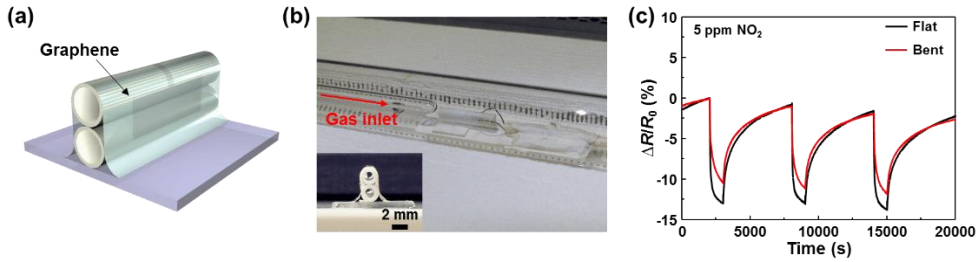

Figure 2.8. (a) Schematic for the patterned all graphene sensor attached on ball pen leads. (b) Optical image of the gas sensing set-up for the sensor under bending strain. The inset shows a side-view photograph of the sensor bent with a bending radius of 1 mm. (c) Response curves of the sensor without and with the bending strain.

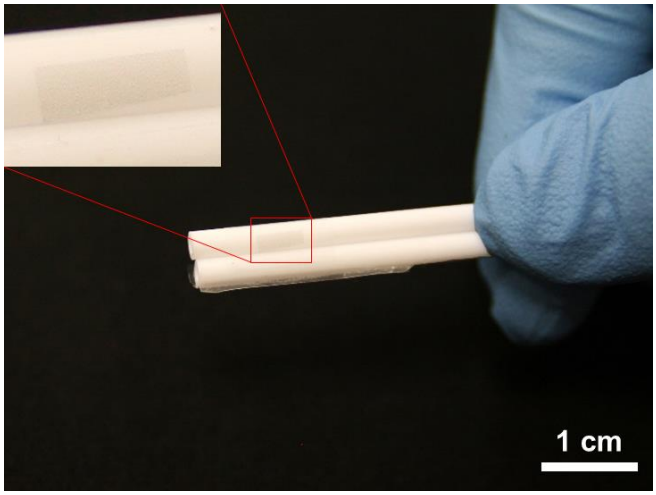

Figure 2.9. The bent all graphene sensor on linked two ball pen leads.

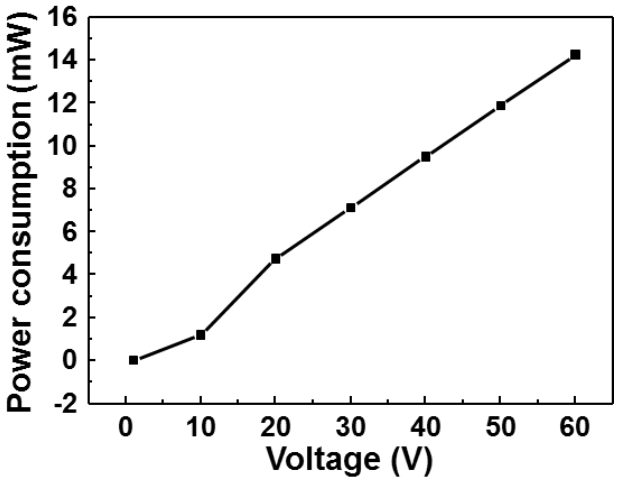

Figure 2.10. Power consumption of the all graphene sensor as a function of applied bias voltage.

2.4. Conclusion

We have developed the self-activated all graphene NO_2 sensors with high transparency, flexibility, and low power consumption. The all graphene sensor showed the self-activation by increasing the bias voltage and the consequent enhancement of gas sensing properties such as fast response and reversible sensing behavior without external heating. The reliable room temperature operation guarantees the stability of graphene sensing layer which could be distorted and eliminated by high temperature operation.[57] Moreover, the sensor composed of single material, graphene, enables having an entirely transparent and flexible device structure leading to reliable sensing performances under extremely high bending strain. We believe that the remarkable device performance, achieved with a simple fabrication process, significantly enlarges the potential of gas sensor applications to the next-generation technologies, such as the IoT and wearable electronics.

Chapter 3

Chemically Fluorinated Graphene Oxide for Room Temperature Ammonia Detection Capability at ppb Levels

3.1. Introduction

Two-dimensional (2D) materials such as the graphene-based materials and transition-metal dichalcogenides have been receiving increasing attention in gas sensing applications, because the single-atomic-layer structure is considered ideal for the adsorption and desorption of gas molecules.[6, 7, 16, 58-63] Especially, the graphene-based materials have been actively researched for chemoresistive gas sensors owing to their unique electrical and gas sensing properties such as low noise level, high surface-to-volume ratio and response to gas molecules at room temperature.[6-13, 32-35, 64, 65] However, pristine graphene-based materials have also several drawbacks such as low sensitivity, long response time, poor selectivity, and irreversible gas sensing behaviors at room temperature. Hence, various approaches such as the use of external heaters, self-activation, hybrid composites with metal oxides or polymers, and surface modifications using metal decoration or functionalization have been explored to operate sensor at low or room temperatures.[7, 8, 12, 34, 35, 66-69] Among the approaches, functionalization has dual advantages that not only serves as a receptor for selective sensitization, but also changes responses by tuning the electronic structures. However, it is still unclear how different functional groups interact with various gas molecules. Thus it is strongly believed that the realization of graphene-based sensor can only be achieved by a thorough

investigation on the relationship between functionalization and sensing capability of graphene.

In the last years, the fluorination of graphene-based materials has attracted many scientists and researchers because fluorine could successfully modify electronic and chemical properties of graphene.[70-78] The incorporation of fluorine into graphene-based materials such as graphene, graphene oxide (GO), and reduced graphene oxide (rGO) is likely to be appropriate to improve gas sensing properties because the fluorine adatom can modify both surface chemistry and electrical nature of the graphene-based materials.[75, 79] Zhang *et al.*[79] showed reversible NH_3 detection of monolayer fluorinated graphene functionalized by a SF_6 plasma treatment, but the sensor response was not much improved (~3%), in comparison with the response (~2.5%) of pristine graphene, to 50 ppm of NH_3. Probably, this result is attributed to the plasma treatment, affecting only the surface of the material, resulting in a low degree and small amount of fluorination. Tang *et al.*[80] reported a theoretical study about strong NH_3 adsorption on the GO surface by active functional groups such as hydroxyl and epoxy groups forming hydrogen bonding. This suggests us that the fluorine adatom which is more electronegative than oxygen would influence on the hydrogen bondings in GO and plays a critical role in NH_3 detection. However, no theoretical work combined with experiments has been

reported how the fluorine adatom on GO alter the electronic structure and influence on intermolecular reactions in the fluorine adatom and also the adjacent functional groups.

Turning to the fluorination process, in the case of chemical vapor deposited (CVD) graphene, surface treatments such as plasma or reactive gas exposures are essential to produce defects, which act as functionalization sites. Thus, the functionalization of CVD graphene has several limitations such as complicated processes and low productivity. In contrast, GO and rGO can be treated by facile solution processes, which have potential for mass production. Also, they have numerous preexisting defects such as oxygen functional groups, dangling bonds, Stone–Wales defects, and holes from the basal plane acting as active sites leading to a sufficient degree of functionalization.[81-83] Despite the advantages of GO for efficient functionalization, studies on the functionalization of GO and their application are not well achieved yet. In this study, thus we have thoroughly investigated the effect of fluorination on the interaction of GO with NH_3 and NO_2 molecules by both experiments and calculations. First-principles calculations were conducted to design experiments, but also estimate the adsorption energies, charge distributions, and the configurations of NH_3 and NO_2 molecules on the GO and chemically fluorinated graphene oxide (CFGO) surfaces. The calculations reveal the

critical role played by the fluorination of GO, resulting in highly sensitive, selective, and fully reversible NH_3 detection at room temperature.

Herein, density functional theory (DFT) calculations are applied to examine the effect of fluorination on intermolecular reactions. We chose the fluorination of GO, because the most electronegative element, fluorine has strong interactions with other functional groups or molecules, which is favorable for gas sensing applications. Our DFT study predicts that the fluorination enhances the binding of GO with NH_3 molecule by decreasing electron density on GO. On the guidance of our DFT results, experimental studies are performed to verify theoretical findings. Our experiment results show that CFGO indeed enhances the interaction with NH_3 molecule. Furthermore, CFGO synthesized by a facile solution process enables a ppb level NH_3 detection. The CFGO sensor exhibited highly sensitive, selective, and reversible response upon multiple exposures of NH_3 with a good linearity and detection limit of ~6 ppb at room temperature. In this study, we have successfully showed the effect of the fluorination on sensing capability of GO by combined approaches of DFT calculations and experiments.

3.2. Experimental section

3.2.1. Preparation of graphene oxide

Natural flake graphite (Lot #: 17425HO, +100 mesh), potassium persulfate ($K_2S_2O_8$, 98%), phosphorus pentoxide (P_4O_{10}, 98%), and potassium permanganate ($KMnO_4$, 98%) were purchased from Sigma-Aldrich. Sulfuric acid (H_2SO_4, 98%), hydrogen peroxide (H_2O_2, 30%), and hydrochloric acid (HCl, 35–37%) were purchased from Daejung Chemicals & Metals. All the chemicals were used as received.

Graphene oxide (GO) was prepared by the conventional Hummers method.[84, 85] First, natural graphite flakes were pretreated with $K_2S_2O_8$ and P_4O_{10} for the easier exfoliation. 10.0 g of $K_2S_2O_8$ and 10.0 g of P_4O_{10} were fully dissolved in 50 mL of 98% H_2SO_4 while vigorously stirring at 80 °C. 5.0 g of graphite was slowly added to the mixture. The mixture was continuously stirred over 12 hr at the same temperature and poured in 2 L of DI. The pretreated graphite was washed with excess water using repeated vacuum filtrations until pH of graphite became neutral, then dried in a vacuum oven at room temperature. This pretreated graphite (2.0 g) was dispersed in 92 mL of H_2SO_4 already cooled to 0 °C. $KMnO_4$ (12.0 g) was very carefully added to prevent explosion. The reaction mixture was transferred to 35 °C and stirred at 300 rpm. After 2 hr, the solution was mixed with 200 mL of water slowly so as to prevent the

temperature from rising above 50 °C and stirred at 45 °C for 2 hr, and 10 mL of H_2O_2 was added. After complete oxidation, this mixture was ultra-centrifuged thrice at 13,000 rpm with 3.4% HCl. The precipitant was repeatedly washed with and completely neutralized by exchanging the solvent with water in repeated ultra-centrifugations at 13,000 rpm 5 times. For eliminating un-exfoliated graphite, the precipitant was centrifuged at 4,000 rpm, and the supernatant was used.

3.2.2. Fabrication of chemically fluorinated graphene oxide gas sensor

2 g of XtalFluor-E and 2 mL of 2 mg/mL GO solution were dissolved in 48% HF solution. The solution was boiled at 180 °C for 2 hr. The mixed solution was completely dried, and the synthesized CFGO particles were collected and diluted to 0.2 mg/mL in deionized (DI) water. Subsequently, the sample was ultrasonicated for enough time to be well dispersed. Pt interdigitated electrodes (IDEs) spaced 5 μm apart were fabricated on the SiO_2/Si substrate using photolithography process, and the final products were drop-casted on the Pt IDEs to evaluate gas sensing properties.

3.2.3. Sensor measurements

The gas-sensing properties of the CFGO sensors were measured at room temperature. As the flow gas was changed from dry air to a calibrated test gas (balanced with dry air, Sinjin Gases), the variation in the sensor resistance was monitored using a source measurement unit (Keithley 2365B). A constant flow rate of 1000 sccm was used for dry air and the test gas. The sensor resistance was measured under a DC bias voltage of 0.5 V. The response of the sensors ($\Delta R/R_0$) was accurately determined by measuring the baseline resistances of the sensors in dry air and the saturated resistances after exposure to the test gas. Gas flow was controlled using mass flow controllers, and all the measurements were recorded using a computer over a GPIB interface.

3.2.4. Calculations

First-principles DFT calculations were performed with projector augmented wave (PAW) method and the generalized gradient approximation of Perdew, Burke, and Ernzerhof (PBE) for the exchange-correlation potential and implemented in Vienna Ab-initio Simulation Package (VASP) code.[86, 87] Monkhorst-Pack k-point sampling with a grid of 4×4×1 was used for the Brillouin zone integration.[88] An energy cutoff of 500 eV was used for the plane-wave representation of the wavefunctions, and atomic structures were relaxed until all the Hellman-Feynman forces were <0.01 eV/Å. The graphene

was constructed by 60 carbon atoms (5 × 3 rectangular supercell). We adapted the GO model in which the graphene surface was functionalized by three hydroxyl (OH) groups and two epoxy (O) groups, as reported in the literature.[89] More than 15 Å of vacuum space was employed along the perpendicular direction to prevent artificial interaction between the periodic images.

3.3. Result and discussion

3.3.1. Surface interaction of GO and CFGO with NH_3 and NO_2

The first- principles DFT calculations were performed in order to investigate the effect of fluorination on the gas sensing of GO. In this study, we identified how the surface interaction of GO with either NH_3 or NO_2 molecules is modified by the fluorination. We first investigated whether fluorine (F) adatom on the GO surface can directly interact with NO_2 or NH_3 molecules and enhance the binding. Our DFT calculations predict that the binding energy of NO_2 and NH_3 molecule with F adatom is only 0.06 and 0.11 eV, respectively, indicating that direct interaction of F adatom with NH_3 molecule is not significant. Therefore, it is reasonable to think that the fluorination indirectly affects the sensing capability of GO surface. Since previous study has shown that the hydroxyl (OH) group attached on the GO surface acts as an active site

for the gas sensing, the effect of fluorination on the sensing capability of other surface functional groups on the GO surface was investigated.[65] Figure 3.1a shows the energetically preferred configurations of NO_2 (i and ii) and NH_3 molecules (iii and iv) on GO surface; the second and fourth figures represent the change in the geometry under the existence of a nearby F adatom. In this study, the energetically favorable GO configuration, reported previously, was used to reveal the interaction of functional groups with either NO_2 or NH_3 molecules on the GO surface.[65] From a rigorous search on various adsorption geometries, the most energetically preferred configuration of NO_2 was identified as one O of NO_2 molecule interacting with two OH groups on the GO surface, as shown in Figure 3.1a–i. For the adsorption of NO_2, the nearby fluorine atom does not change the adsorption geometry significantly (Figure 3.1a-ii). Unlike the case of NO_2, the adsorption geometry of NH_3 molecule was significantly affected by F adatom. Without the F adatom, the N of NH_3 is mainly interacting with one OH group (Figure 3.1a–iii). With the existence of F adatom, the epoxy (O) group moves toward the H of NH_3 and forms an additional binding with NH_3 (Figure 3.1a–iv).

Further the intermolecular distance between surface functional groups and the adsorbed molecule was investigated to understand the effect of the F adatom (Figure 3.1b). For NO_2, the distances between the two OH groups and

O of NO_2 are 1.61 (left) and 1.72 Å (right). Thus, NO_2 forms a strong binding with the left-side OH group. Placing an F adatom near the left-side OH group, the intermolecular distances changed to 1.64 Å (left) and 1.69 Å (right), indicating that strong binding between the left-side OH group and NO_2 is weakened by the F adatom. Our DFT calculations show that the binding energy of NO_2 on rGO reduced from 0.55 eV to 0.43 eV with the F adatom. Thus, fluorination weakened the binding between GO and NO_2. In contrast, the F adatom reduces intermolecular distances for NH_3. The distance between the O group and the H of NH_3 significantly reduced from 2.06 to 1.66 Å with the nearby F adatom. This atomic motion represents that the O group actively participates in the adsorption of NH_3 by breaking one of its two bindings on the GO surface (Figure 3.2). As the O group moves close to the H of NH_3, the hydrogen binding enhances the adsorption. Similarly, the distance between the H of OH group and the N of NH_3 also reduced from 1.74 to 1.64 Å, and thus the hydrogen bonding between them is strengthened. Hence, with F adatom, the NH_3 adsorbed on the GO surface binds strongly with both the O and OH groups and forms the hydrogen bond network that connects the OH group to the O group (–OH···N– H···O). Consequently, the binding of NH_3 with surface functional groups is enhanced with the F adatom.

The variation in the electron charge density of GO induced by the F adatom was investigated in order to understand the physical origin of the change in the binding energy (Figure 3.1c). The blue and red isosurfaces represent the regions where the charge density increased or decreased by the F adatom. The addition of F adatom increases the electronic charge density on the O group, while decreases the charge density on the H of OH group. The Bader charge analysis shows that the charge density on the O group increased by 0.103e, whereas the charge density on the H of OH group decreased by –0.046e. Since the O group does not affect the adsorption of NO_2, the decreased charge density on the H of the OH group weakens the bonding with the O of NO_2 molecule. As a result, the bonding distance between the OH and NO_2 molecule increases, and thus the binding energy is reduced. For the case of NH_3 adsorption, the decreased charge density on the H of OH group strengthens the bonding with the N of NH_3 molecule because of negative polarization on N. In contrast, the increased charge state on the O group enhances the bonding with H of NH_3, because of positive polarity of H. As a result, NH_3 binds strongly with the OH and O groups and forms a hydrogen bond network (–OH···N–H···O).

To verify our findings on the effect of the charge density on the binding energy of NO_2 and NH_3 molecules, additional calculations were performed by

directly adding or subtracting an electron to GO. Figure 3.1d shows the change in the binding energies under different electronic conditions of GO. Under reducing conditions, the binding energies of the NO_2 and NH_3 are 0.55 and 0.47 eV, respectively, and thus NO_2 more strongly binds with rGO. However, the binding energies of NO_2 and NH_3 vary in the opposite direction when electrons are subtracted. The binding energy of NO_2 decreases to 0.32 and 0.01 eV under neutral and oxidizing conditions, respectively. In contrast, the binding energy of NH_3 increases to 0.59 and 0.77 eV under neutral and oxidizing condition, respectively. Thus, under neutral and oxidizing conditions, GO binds more actively with NH_3 than NO_2. The electronic state dependence of the binding energy is comparable to the case of fluorination. Similar to the case of F adatom, subtracting one electron reduces the electron density on OH groups by –0.04e. As a result, the interaction of the OH groups with the N of NH_3 is enhanced, whereas that of the O of NO_2 is weakened. Notably, the O group does not participate in the adsorption of either NH_3 or NO_2 under oxidizing condition, because it is energetically less favorable by 0.24 eV. However, it is still valid to conclude that the decreased charge density on the OH group enhances the binding of NH_3 and weakens the binding of NO_2. Consequently, the rGO sensor is more sensitive to NO_2 than NH_3, and the CFGO sensor exhibits higher responses to NH_3. Therefore, the DFT

calculations are in agreement with the experimental data of superior sensing characteristic of CFGO sensor for NH_3 molecule.

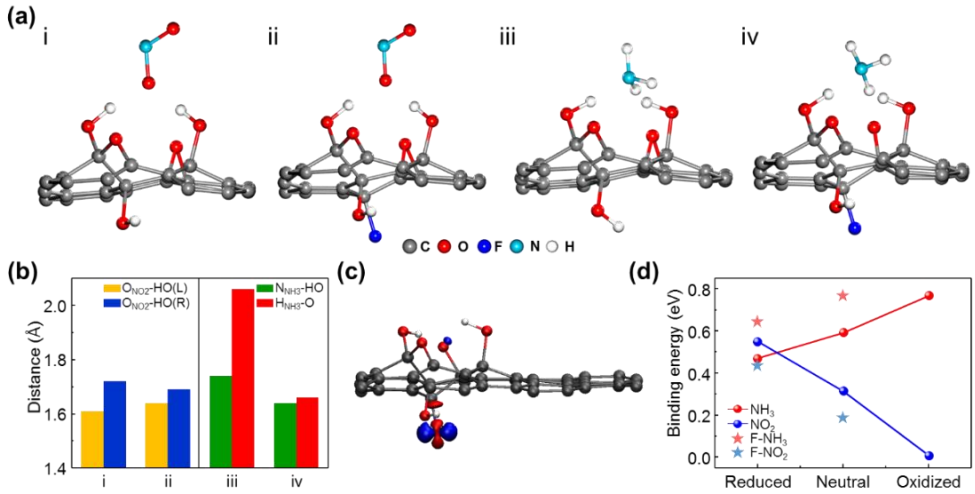

Figure 3.1. (a) Configurations of GO and CFGO after adsorption of (i, ii) a NO_2 molecule and (iii, iv) a NH_3 molecule. (b) The distance between the oxygen functional groups and gas molecules. The left and right sides are marked as (L) and (R), respectively. (c) Variation of charge density after fluorination; blue and red colors show the regions where charge density is increased and decreased after fluorination. The isosurfaces are plotted at ±0.17 e/Å^3. (d) Binding energies of NO_2 and NH_3 molecules on GO under electron deficiency (1h$^+$, oxidized), electron neutral (neutral), and electron excess (1e$^-$, reduced). The binding energies of NH_3 and NO_2 on GO with fluorination are expressed as F-NH_3 and F-NO_2 under each electron state (reduced, GO).

3.3.2. Adaptive motion of NH_3

Comparing before and after the fluorination of GO, oxygen containing groups and NH_3 molecule rotate and change their absolute positions in Figure 3.2. The O group basically has two bonds and is not significantly involved in the adsorption of NH_3 molecule before fluorination. However, after fluorination, O group loses one of the bonds, and the oxygen moves closer to H of NH_3. As explained previously, these adaptive motions play crucial roles in the adsorption mechanisms by adjusting the distance between gas molecules. Our DFT calculations successfully explain the experimental observations. The closer distances and consequent increase in the binding energies are responsible for the high response to NH_3. In addition, full recovery can be explained by optimal fluorination and reduction procedures. When the mixed solution was boiled in the CFGO fabrication process, not only fluorination but also reduction occurred at elevated temperature of 180 °C. Since the reduction process decreased the binding energies of NH_3 and increased the binding energies of NO_2 in direct opposition to the fluorination process, optimal degree of reduction and fluorination may occur and lead to moderate binding energies of NH_3 for full and fast recovery recovery in the entire system of the device. However, reversible behaviors in sensing materials cannot be explained by only binding energies, but also other factors like modified surface chemistry,

structures or other inherent natures of sensing materials. For instance, although adsorption energies between target gas and sensing material are much higher in our previous work, full recovery has been reported.[61] To the best of our knowledge, recovery behaviors of two-dimensional sensing materials are not well defined yet. Further studies are essential to confirm and establish the sensing mechanisms including recovery stage.

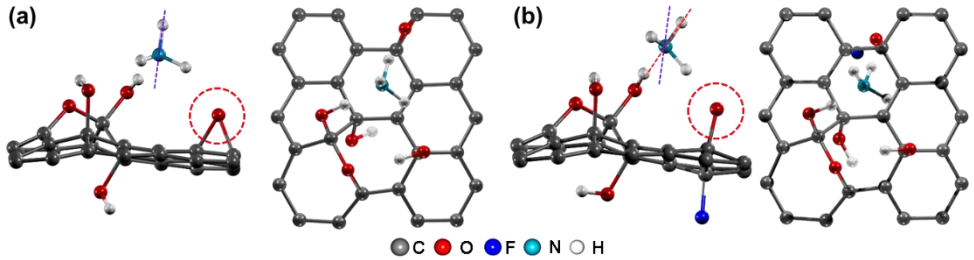

Figure 3.2. Ball and stick models of GO with adsorption of a NH_3 molecule (a) before and (b) after doping of a fluorine molecule. The rotation of the NH_3 molecule with the doping of a fluorine molecule is highlighted by dotted lines.

3.3.3. Density of State of CFGO

The electronic structures of graphene, GO and CFGO were investigated. Figure 3.3 presents the band structures and density of states (DOS) of GO and CFGO. We emphasize that DFT on fluorinated GO has not been reported yet. We found that the bandgap energy of GO and CFGO is nonzero, which reflects its semiconducting nature. This semiconducting behavior seems to be an essential feature of chemoresistive materials that possess high response to a target gas, and is related to ratio between the number of total carriers in the material and the number of carriers involved in charge transfer between the material and adsorbed gas molecules. Field-effect transistor (FET) characteristics are measured to check electrical behaviors of CFGO and rGO (Figure 3.4.). The rGO device shows a p-type FET behavior and the CFGO device shows ambipolar behavior with a Dirac point at Vg = 15 V. While the metallic graphene with abundant charge carriers would be relatively insensitive to the charge transfer (Figure 3.5.). Fluorine does not significantly change electronic band structure near Fermi level. However, the actual Fermi level position has been shifted by F adatom as can be seen from DOS. The F adatom shifts the Fermi level to 0.24 eV lower than valance band maximum. As a result, the addition of F adatom yields similar effect to oxidation, which represents electron deficiency and leads to high sensitivity to NH_3. This is

consistent with the calculation result in Figure 3.1d. In previous studies, DFT calculations are exploited for investigating intermolecular reactions only between doped atoms and gas molecules by calculating binding energies.[13, 17, 79, 90] We emphasize here that investigation of electronic structure changes by a fluorine atom and the consequent variations in intermolecular reactions between the adjacent functional groups and gas molecules are more realistic to estimate the fluorination effect on gas sensing behaviors. Moreover, DFT calculation study on gas sensing properties of fluorinated graphene oxide has never been reported yet.

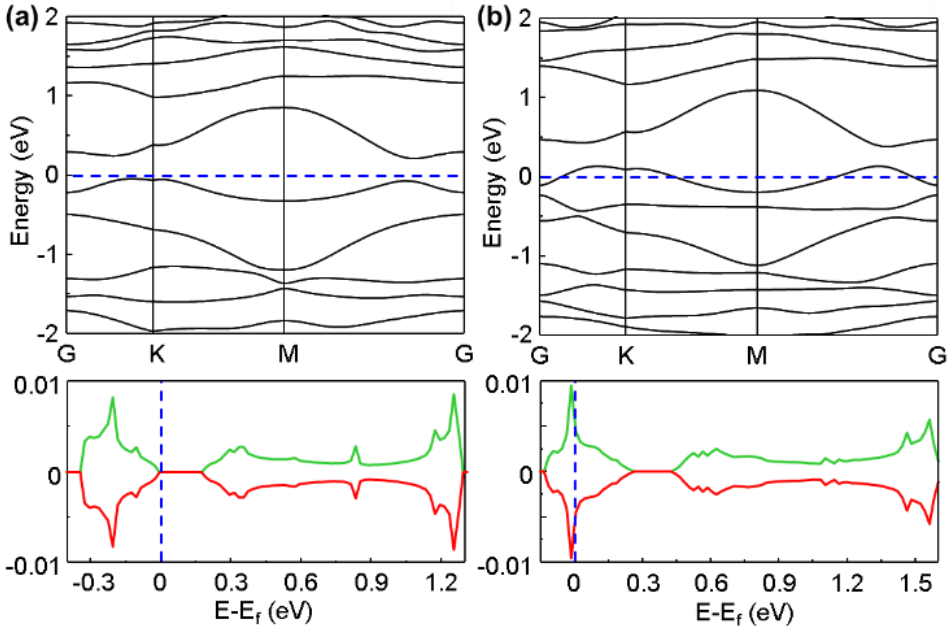

Figure 3.3. Electronic band structure (upper) and density of states (lower) of (a) GO, and (b) CFGO. The electronic band structures are plotted along the high symmetric k-points of the primitive graphene cell. The green and red lines correspond to the spin-up and spin-down states, respectively. The blue dashed lines show the Fermi level of the systems.

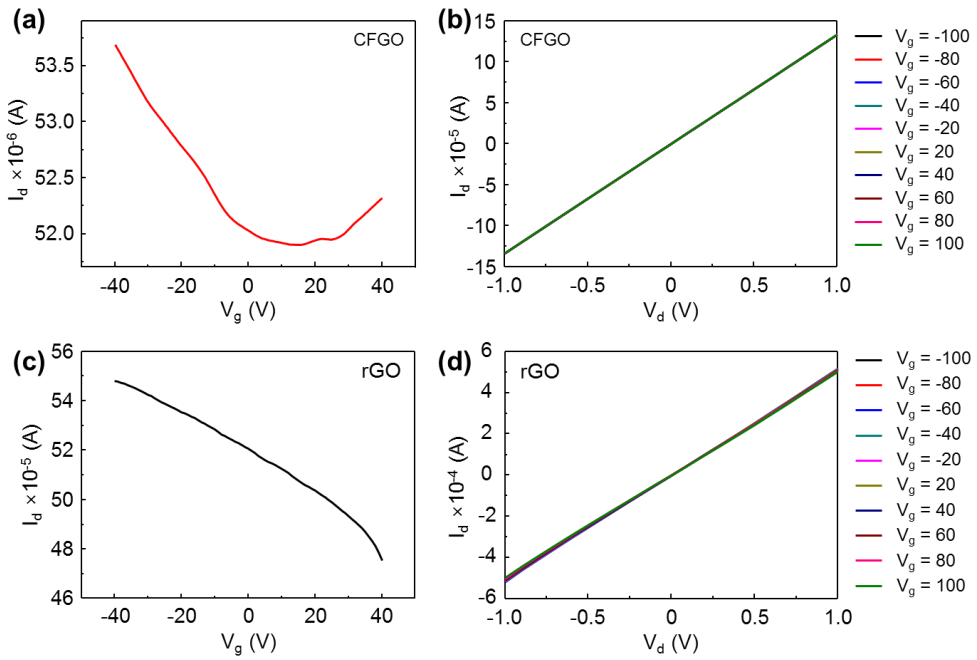

Figure 3.4. Transfer and output characteristics of (a-b) CFGO and (c-d) rGO FETs.

FET characterization

The channel length and width of the fabricated FETs were 100 and 2000 μm, respectively. Current-voltage characteristics of all devices were measured using a Keithley 4200-SCS and a probe station operated under air condition. After deposition of source and drain electrodes, each device was isolated by a mechanical scratch. In order to collect transfer characteristics, the gate voltage was swept from $V_g = 40$ V to $V_g = -40$ V in increments of −1 V, while the source-drain voltage was kept unchanged at $V_d = -0.1$ and 1 V for CFGO and rGO devices, respectively.

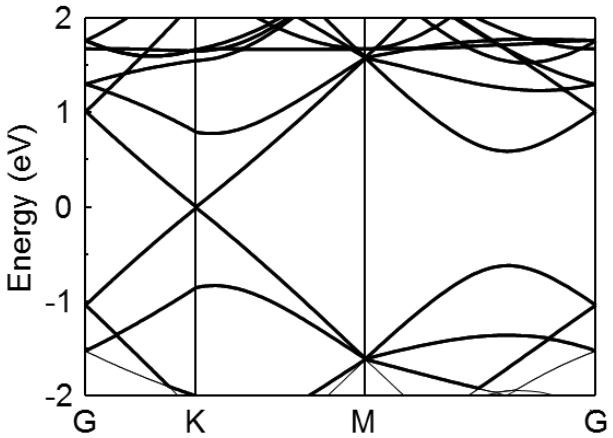

Figure 3.5. Electronic band structure of graphene.

3.3.4. Synthesis and characterization of CFGO

The CFGO sample used in this study was synthesized by a facile solution process. XtalFluor-E (2 g) and 2 mL of 2 mg/mL GO solution were dissolved in 48% HF solution. The solution was boiled at 180 °C for 2 hr. After the mixed solution was completely dried, the synthesized CFGO particles were collected and diluted to 0.2 mg/mL in deionized (DI) water. Subsequently, the sample was ultrasonicated for enough time to be well dispersed (Figure 3.6a). The optical images of 0.2 mg/mL GO and CFGO solutions in DI water are shown in Figure 3.6b. Pt IDEs spaced 5 μm apart were fabricated on the SiO_2/Si substrate using photolithography process, and the final products were drop-casted on the Pt IDEs to evaluate gas sensing properties (Figure 3.6b, c). Figure 3.6d shows the scanning electron microscopy (SEM) image of the drop-casted CFGO film on Pt IDEs. The drop-casted CFGO film exhibited a porous structure, favorable for gas sensing owing to its high surface-to-volume ratio. As surface-to-volume ratio of sensing materials increases, response of the materials is increased. In order to verify and compare the porosity between CFGO and rGO films, SEM image of the rGO film is obtained as shown in Figure 3.7. The overall high responses of CFGO to various gases attribute to not only influence of fluorination but also higher porosity of the CFGO film.

X-ray photoemission spectroscopy (XPS) was carried out to confirm the fluorination degree of CFGO sample. Figure 3.8a shows the XPS survey spectra of CFGO, rGO, and GO. The fluorine-related peak (F1s peak) was recorded at 688.7 eV only for the CFGO, whereas O1s and C1s peaks were recorded for all the three samples. A tiny N1s peak in the survey scan is observed but the intensity is too low to discuss nitrogen doping effect comparing to F1s peak. The content of fluorine and ratio of C to F was calculated from the XPS survey scan spectra based on the atomic sensitivity factors.[91] The atomic percentage of fluorine and the ratio of C to F in this study were calculated as 25.21 and $C_{2.38}F$, respectively. In comparison with other previous studies as shown in Table 3.1., the content and ratio are rather high, considering the simplicity of this synthetic method.[71, 72, 77, 79, 92] Carbon and oxygen contents of CFGO, rGO and GO samples are shown in Table 3.2. The high-resolution C1s spectrum provides detailed information about the surface functional groups of rGO and CFGO. For the C1s peak of rGO, deconvolution reveals the presence of C-C (284.5 eV), C-OH (285.7 eV), and C=O (287.0 eV), and O=C−OH (288.5 eV) species, and low peak intensities of the oxygen-containing functional groups (Figure 3.8b). These results are in excellent agreement with previous study.[93] In the case of CFGO sample, the high-resolution C 1s XPS spectrum was deconvoluted into four peaks with the

binding energies of 284.5, 285.4, 286.5, and 288.5 eV, corresponding to the C sp^2, C−C−F, C−CF_2, and C−F bonds, respectively (Figure 3.8c).[71, 79, 94, 95] The chemical mapping of CFGO was obtained by energy dispersive X-ray spectroscopy (EDS) in the scanning transmission electron microscopy mode (Figure 3.8d). Each image shows the mapping of O, C, and F elements, for the selected area (upper left corner image in Figure 3.8d). Because Xtalfluor-E was exploited to induce substitutional doping by replacing oxygen atoms with fluorine atoms, the fluorine and oxygen atom sites are very adjacent in the mapping images, verifying direct replacement of oxygen by fluorine.[96] The TEM images of CFGO at different magnifications are shown in Fig 3.8e and f, and the upper inset exhibits the corresponding electron diffraction pattern. The electron diffraction pattern obtained from the CFGO reveals the amorphous nature. Each D and G peak in fifteen times of rGO and CFGO Raman spectra was analyzed with Lorentzian functions (Figure 3.9). I_D and I_G denote peak intensities of D and G peak, respectively. Increase of the intensity ratio I_D/I_G indicates increase of defect density in graphene-based materials.[41, 97] Figure 3.9 reveals high defect density of CFGO which would enhance the gas sensing performances.

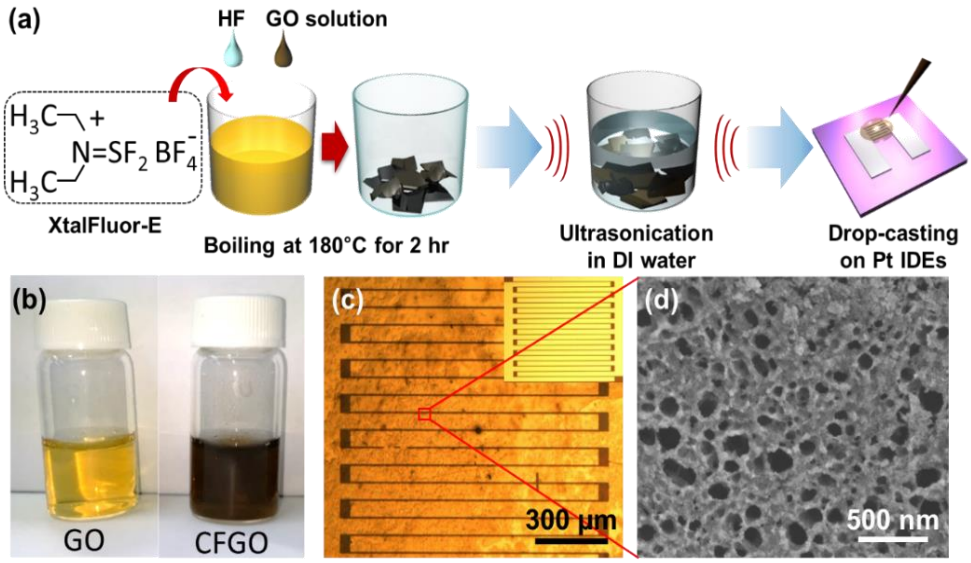

Figure 3.6. (a) Fabrication process of CFGO ammonia gas sensor. (b) Photographic images of GO and CFGO solutions. (c) Optical and (d) SEM images of drop-casted CFGO on Pt IDEs.

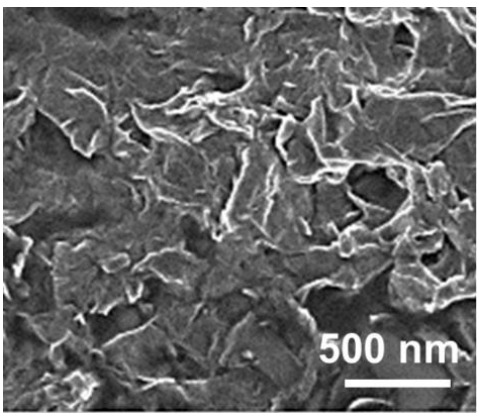

Figure 3.7. SEM image of a rGO film.

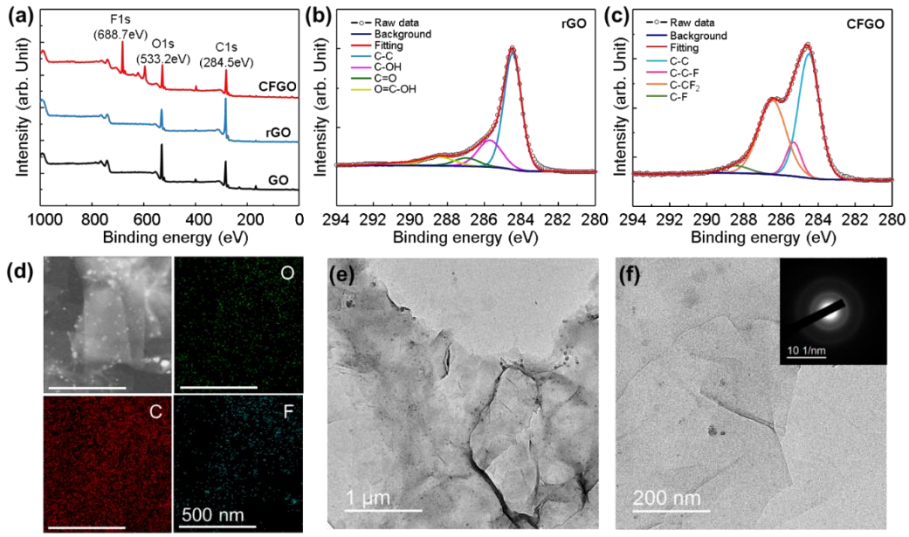

Figure 3.8. (a) XPS survey scan of CFGO, rGO, and GO films. High-resolution C1s spectra of (b) rGO and (c) CFGO films. (d) EDS element maps of CFGO. (e-f) TEM images of CFGO in different magnifications.

Synthetic method	Fluorine content (atomic %)	C/F ratio	Reference
Facile solution process	25.21 (Carbon: 60.10, Oxygen: 14.69)	$C_{2.38}F$	This work
Hydrothermal method	-	$C_{2.1}F$	71
Annealing with gas exposure	33.41 – 48.11	$C_{1.65\text{-}0.98}F$	72
Gas exposure	4.94 – 34.36	$C_{11.49\text{-}1.56}F$	77
Plasma treatment	24.6	$C_{3.1}F$	79
Improved hummer's method	23.00	$C_{2.81}F$	92

Table 3.1. The content of fluorine and ratio of C/F in this work and the previous works.

Product	Carbon and oxygen content (atomic %)	C/O ratio
CFGO	Carbon: 60.10, Oxygen: 14.69 (Fluorine: 25.21)	$C_{4.09}O$
rGO	Carbon: 86.86, Oxygen: 13.14	$C_{6.61}O$
GO	Carbon: 70.33, Oxygen: 29.67	$C_{2.37}O$

Table 3.2. The content of carbon and oxygen in CFGO, rGO and GO.

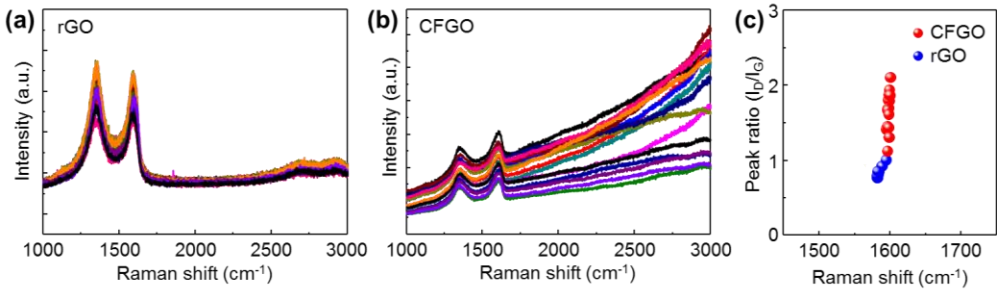

Figure 3.9. Raman spectra of (a) rGO and (b) CFGO films for fifteen different spots on SiO_2 substrates. (c) Intensity ratio I_D/I_G of CFGO (red) and rGO (blue) film.

3.3.5. Gas sensing properties of CFGO

The experimental results indicate that the fluorination of GO strongly affects the gas sensing properties. Figure 3.10a shows the dynamic sensing transients of the CFGO gas sensor. The device was exposed to five consecutive pulses of 500 ppm of NH_3 balanced with dry air at room temperature. The response ($|\Delta R/R_0|$) to 500 ppm NH_3 is 121%. Figure 3.10b shows the responses of the CFGO sensor to 500 ppm of NH_3, 5 ppm of NO_2, 500 ppm of H_2, and C_2H_5OH, 50 ppm of C_7H_8, and 100 ppm of CH_3COCH_3. The CFGO sensor shows a high response to NH_3 (~120%). The responses to 5 ppm of NO_2, 500 ppm of H_2, and C_2H_5OH, 50 ppm of C_7H_8, and 100 ppm of CH_3COCH_3 are 76.3, 54, 18, 4.96, and 24.1%, respectively. The response curves to each gas are exhibited in Figure 3.11. To check for the linearity of responses with different NH_3 concentrations, the response of the sensor was measured over a wide range of NH_3 concentrations from 20 to 500 ppm (Figure 3.10c). As the NH_3 concentration increases, the response of the CFGO sensor proportionally increases. The response values were plotted as a function of the gas concentration as shown in Figure 3.10d. The linear regression equation is expressed as $y = 0.08404x + 70.07697$, where y is the response and x is the concentration of NH_3. The measure of goodness-of-fit of the linear regression, r^2, was calculated to be 0.9115. The responses of the sensor are 67.23, 74.66,

83.39, 93.87, 97.114, and 115.13% to 20, 50, 100, 250, 400, and 500 ppm NH_3, respectively.

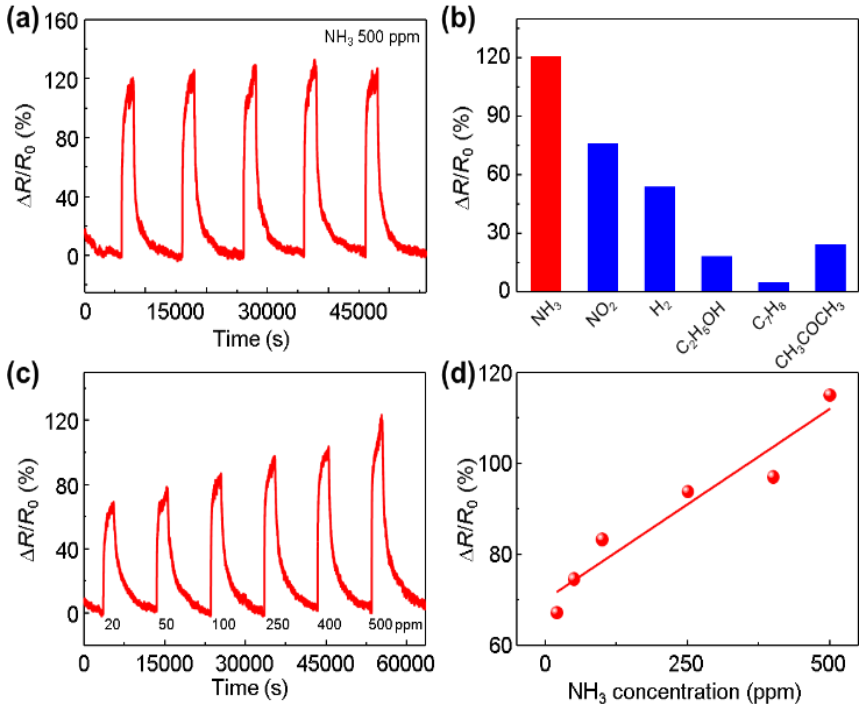

Figure 3.10. (a) Response curves of the CFGO sensor to five pulses of 500 ppm of NH_3. (b) Responses of the CFGO sensor to 500 ppm NH_3, H_2, C_2H_5OH, 5 ppm NO_2, 50 ppm C_7H_8, and 100 ppm CH_3COCH_3. (c) Response curves to different NH_3 concentrations from 20 to 500 ppm. (d) Linear fit of the responses as a function of NH_3 concentration.

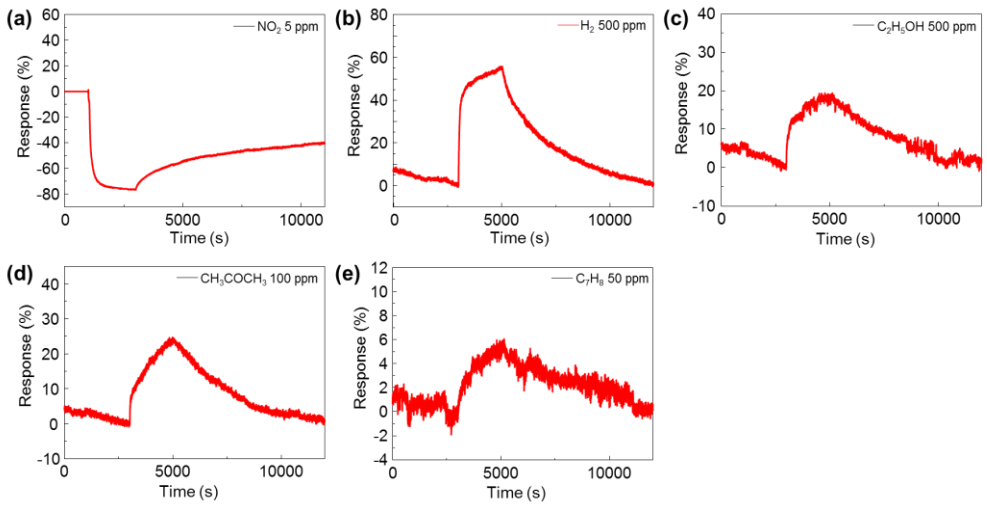

Figure 3.11. Response curves of the CFGO sensor to (a) 5ppm NO_2, (b) 500 ppm H_2, 500 ppm C_2H_5OH, 100 ppm CH_3COCH_3 and 50 ppm C_7H_8.

The performance of rGO sensor as a reference was measured to compare the gas sensing performances with the CFGO sensor. Inset in Figure 3.12a shows the slow response and irreversible recovery of the rGO sensor. However, the CFGO sensor exhibits fast response and full recovery. For both the sensors, response time and recovery time (response t_{50} and recovery t_{50} are the time for the sensor's resistance to reach 50% of its steady state value in the gas response and the recovery to original state, respectively) were calculated. The response t_{50}s were 419 and 86 s, and the recovery t_{50}s were the infinite time, and 116 s for the rGO and CFGO sensors, respectively (Figure 3.12b). The CFGO sensor exhibited not only short response and recovery times, but also high response and reversible sensing behavior to NH_3 and NO_2. In Figure 3.12c, the percentage response and recovery for the rGO and CFGO sensors upon exposure to NO_2 and NH_3 are displayed. The percentage responses for the CFGO sensor to NO_2 and NH_3 are ~5.5 and ~20 times higher than those of the rGO sensor, respectively. Particularly, after NH_3 exposure, complete recovery was achieved for the CFGO sensor. These results demonstrate extremely enhanced sensing performances to NH_3.

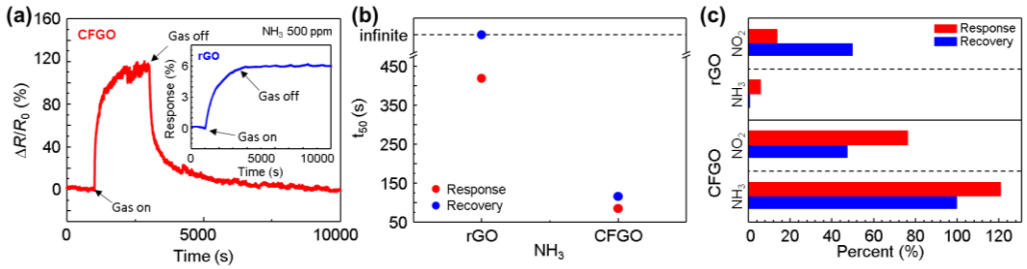

Figure 3.12. (a) Response curves of CFGO and rGO sensors to 500 ppm of NH_3. (b) Response and recovery t_{50} of the rGO and CFGO sensor to 500 ppm of NH_3. (c) Percentage responses and recoveries for rGO and CFGO sensors to NO_2 and NH_3.

3.3.6. NH_3 sensing properties at ppb level and comparison with previous literatures

In addition, the NH_3 sensing properties of the CFGO sensor at ppb levels were investigated. Also, in order to investigate influence of humidity, the CFGO sensor was measured in 50 to 90% of relative humidity atmosphere (Figure 3.14). Detection limit down to ppb levels broadens the potential application fields of gas sensor such as breath analysis.[98] The sensor was exposed to different concentrations of NH_3 from 100 to 500 ppb (Figure 3.13a). The responses of the sensor are 29.78, 28.95, 28.06, 26.94, and 25.86% to 500, 400, 300, 200, and 100 ppb NH_3, respectively. It is worth notice that the CFGO showed still very high response of 25.86% to 100 ppb NH_3. To compare the NH_3 sensing properties of the CFGO sensor with those of conventional gas sensors based on graphene materials, the response ($|\Delta R/R_0|$) values versus the NH_3 concentration (ppm) was plotted, as shown in Figure 3.13b.[8, 42, 47, 64, 79, 99-104] Although gas sensors based on pristine graphene, structured graphene, graphene composites, and functionalized graphene have been investigated, the NH_3 sensing performance is conspicuously lower than that of the CFGO sensor. The linearity from Figure 3.10d can be recalculated over wide range of NH_3 concentration, including the response upon 100 ppb of NH_3 (Figure 3.13c). The responses as a function of NH_3 concentration exhibited very good

linearity with the linear regression r^2 values of 0.9969. The theoretical detection limit (signal-to-noise ratio > 5) was calculated as 6.12 parts per billion (ppb).[5, 47] To the best of our knowledge, this appears to be the first report, presenting room temperature NH_3 gas sensors using graphene-based materials with an extremely low detection limit, down to ~6 ppb.

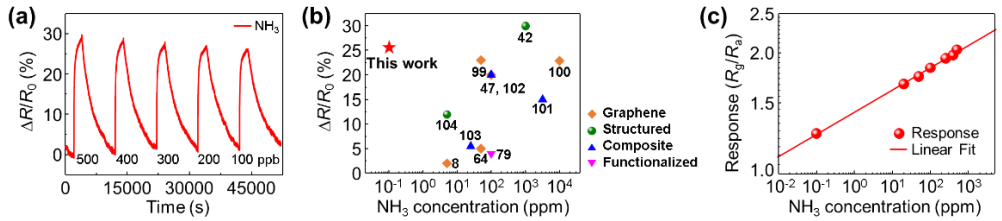

Figure 3.13. (a) Response curves to different NH_3 concentrations at ppb levels. (b) Comparison of NH_3 detection ability of the CFGO with the previously reported graphene-based materials such as graphene (Ref. 8, 47, 64, 99-100), functionalized graphene (Ref.79), nanostructured graphene (Ref. 42, 104), and graphene composites (Ref. 101-103). (c) Linear fit of the responses as a function of NH_3 concentration.

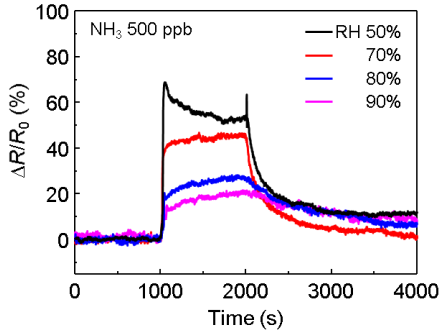

Figure 3.14. Response curves of the CFGO sensor to NH_3 500 ppb in 50 to 90 % of relative humidity (RH) atmosphere.

3.4 Conclusion

In summary, significantly enhanced NH_3 detection of CFGO sensor prepared by a facile solution process was demonstrated. The CFGO sensor showed selective, reversible and rapid NH_3 sensing behaviors with a detection limit of 6.12 ppb at room temperature. The gas response of CFGO on NH_3 exposure was ~20 times higher than that of rGO. To investigate the interrelationship between the fluorine doping on GO surface and the effect on the gas sensing behaviors, the interaction of functional groups with either NO_2 or NH_3 molecules on the CFGO surface was investigated by DFT calculations. Our calculations revealed that F adatom extremely enhances NH_3 sensing capabilities through the changes of the charge distributions on the functional groups, resulting in the variation in the gas adsorption energies. These results not only demonstrate the effect of functionalization on the gas sensing mechanism, but also lay the groundwork for functionalized 2D materials to be applied to practical applications such as IoT.

Chapter 4

Ultrasensitive Reversible Oxygen Sensing in Liquid-Exfoliated MoS_2 Nanoparticles

4.1. Introduction

In the modern society, managing air quality is essential for enhancing the quality of human life. The high concentrations of fine dust, CO, NO_2, SO_2 and CO_2 causes complex respiratory diseases and hampers the productivity and learning ability at work places.[105] Furthermore, as Internet of Things (IoT), interconnected devices capable of exchanging their own information about the internal state and the external environment with users or other devices, attracts attention, monitoring air quality becomes a requisite function for next-generation electronics.[23]

Until now, concentrations of CO, NO_2, SO_2, and CO_2 have been measured in parts-per-million (ppm) level for monitoring air quality, because exposure to small portions of these gases can have a detrimental effect on human health. Detecting oxygen concentration in percentage terms is also important because low levels of oxygen can produce negative symptoms in humans. The symptoms of increased heart and breathing rates and impaired attention are caused by oxygen concentrations >16%. In a harsh environment, workers can become asphyxiated at oxygen concentrations below 12% (Table 4.1).[106] Moreover, oxygen concentration should be maintained at a certain level for particular applications like incubators for premature infants, and cell culture

media. The development of oxygen gas sensors that can detect oxygen over a broad concentration range is desired for varied applications.

Chemoresistive gas sensors based on semiconducting materials are considered promising candidates for emerging applications such as IoT and flexible electronics due to facile fabrication process, small sizes, low costs, and easy integration into integrated circuits. However, commercialized oxygen sensors are mostly based on electrochemical gas sensors. These sensors have complex structures and hardly provide high reliability and linearity over a wide range of oxygen concentration, which limits their applicability to IoT and flexible electronics.[107]

2D materials are gaining increasing attention in this field as prospective sensing materials because surface without bulk offers high surface-to-volume ratio, and surface configurations including dangling bonds on the edge sites and basal planes can be easily modified. Moreover, facile surface modification with charge-transfer doping effects readily improves the gas sensing properties.[108-110] Particularly, MoS_2, a layered semiconducting transition metal dichalcogenide, has shown interesting gas sensing properties owing to its high surface-to-volume ratio, semiconducting nature, and numerous active edge sites.[16, 21, 58, 59, 63, 111] However, despite the increasing attentions and the

diverse researches, studies on the relationship between the gas sensing mechanism and the edge sites of 2D MoS_2 have not been achieved yet.

Herein, we report the comparative oxygen sensing behaviours of liquid-exfoliated MoS_2 nanoparticles and mechanically exfoliated MoS_2 microflakes. The sensors prepared by drop-casting methods on Pt interdigitated electrodes (IDEs) exhibit high and linear response to a wide range of oxygen concentrations due to the increased number of active edge sites. The adsorbed oxygen promotes the interaction kinetics between the reducing gases and the sensing materials, resulting in high sensitivity to ethanol at a parts-per-billion (ppb) level under ambient conditions.[112-118] First-principles calculations were conducted to estimate the oxygen adsorption energies based on the surface configuration of the 2D materials. The calculations reveal the critical role played by the specific adsorption sites in the reversible and high oxygen response.

Table 4.1. Effects of oxygen-deficient exposure.[106]

Oxygen concentration (% vol)	Health effects of persons at rest
19	Some adverse physiological effects occur, but they may not be noticeable.
15–19	Impaired thinking and attention. Increased pulse and breathing rate. Reduced coordination. Decreased ability to work strenuously. Reduced physical and intellectual performance without awareness.
12–15	Poor judgment. Faulty coordination. Abnormal fatigue upon exertion. Emotional upset.
10–12	Very poor judgment and coordination. Impaired respiration that may cause permanent heart damage. Possibility of fainting within a few minutes without warning. Nausea and vomiting.
below 10	Inability to move. Fainting almost immediate. Loss of consciousness. Convulsions. Death.

4.2. Experimental section

4.2.1. Preparation of MoS_2 nanoparticles

The procedures for exfoliating MoS_2 into nanoparticles were adapted from a previous report and slightly modified.[119] Briefly, natural molybdenum sulfide powder (MoS_2, Sigma-Aldrich) was immersed into N,N-dimethylformamide (DMF, Sigma-Aldrich) at an initial concentration of 10mg mL^{-1} followed by ultrasonication at 60 Hz for 12 hours. The mixture was washed by centrifugation at 14,000 rpm for 15 minutes 4 times, changing DMF into distilled water. The obtained solution was centrifuged at 2,000 rpm for 30 minutes, and the top 2/3 of the supernatant was collected. The precipitated solid was re-dispersed in distilled water at concentration of ~2mg mL^{-1}.

4.2.2. Sensor fabrication

IDEs of 4 μm interspacing were prepared on SiO_2/Si substrate using photolithography followed by metal (Pt/Ti) deposition by e-beam evaporation. A 2 μg drop of 2 mg mL^{-1} MoS_2 nanoparticle solution was cast onto a Pt IDEs/SiO2/Si substrate and was then dried for 30 minutes at 100 °C. The fabricated sensors were annealed at 300°C for 20 minutes. To prepare SnO_2 nanosphere sensors, an aqueous suspension of 300-nm-diameter polystyrene (PS) beads was used. The PS beads were spin-coated on O_2 plasma treated Pt IDEs/SiO_2/Si substrate. A 70 nm-thick

SnO_2 film was deposited onto the PS template by room-temperature radio frequency sputtering. The sample was calcined in air at 500 °C for 1 hour to burn out the polymer beads and simultaneously crystallize the SnO_2 film, resulting in a nanosphere film on the substrate.

4.2.3. Characterizations

MoS_2 nanoparticles on Si substrate were characterized by a scanning electron microscope (FE-SEM, MERLIN Compact, ZEISS) using 1 kV. For TEM study, MoS_2 nanoparticles were deposited on quantifoil Cu grids (300–mesh holey carbon). The TEM experiments were performed by JEM-2100F. The AFM image (NANO Station Ⅱ, Surface Imaging system) was obtained in non-contact mode. Raman scattering was performed on a Raman spectrometer with excitation by 640 nm laser light. XPS was carried out at 4D beamlines at Pohang Accelerator Laboratory (PAL).

4.2.4. Sensor measurements

The gas sensing properties of the fabricated MoS_2 nanoparticle sensor and the SnO_2 nanosphere sensor were measured at 300 °C by monitoring the variation in sensor resistance on changing the flow gas from dry air to a calibrated test gas (balanced with dry air). The sensor resistance was measured under a DC bias voltage of 3 V using a source measurement unit

(Keithley 236). A constant flow rate of 500 sccm was used for dry air and the test gases. The response of the sensors was accurately determined by the ratio of the fully saturated resistances after exposure to the test gases to the base resistances in dry air.

4.2.5. Calculations

All first-principles calculations in this study were performed using Vienna *ab Initio* simulation package (VASP).[120] The electron-ion interaction is described by projected-augmented wave (PAW) pseudopotential.[87] We employ PBE for exchange-correlation functional.[86] A plane-wave cutoff of 350 eV and a 40×1×1 k-point grid was used for the unit cell of semi-infinite stripe of MoS_2. All the atomic coordinates were relaxed within 0.03 eV/Å. For modeling edge sites, the semi-infinite stripe of MoS_2 ribbon having the width of 6 Mo atoms was used. To investigate how the width of MoS_2 flake affects the simulation, the density of states of each layer for MoS_2 flakes with widths of 12 unit cells and 6 unit cells, and bulk MoS_2 layer of infinite unit cells was investigated (Figure 4.1). The effect of O_2 coverage on G_{ad} was studied by multiplying the periodicity of O_2 adsorption given in Figure 4.8 by two or four times but G_{ad} changes within 0.01 eV

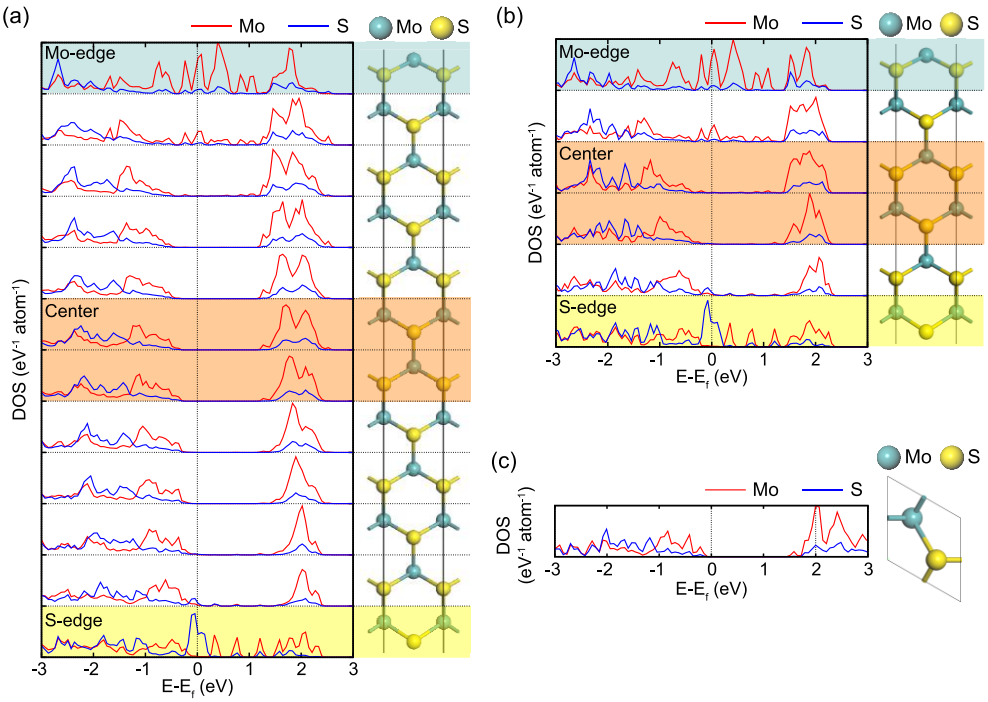

Figure 4.1. Density of states of each layer for MoS_2 flakes with widths of (a) 12 unit cells and (b) 6 unit cells, and (c) bulk MoS_2 layer of infinite unit cells.

Figure 4.1 shows the density of states (DOS) of each layer for MoS_2 flakes with widths of 12 unit cells (uc) and 6 uc, and bulk MoS_2 layer of infinite uc. 12 uc and 6 uc models have the Mo-terminated edge on the top, the S-terminated edge on the bottom and bulk-like uc at the center. The DOS of Mo- and S-terminated edges of 12 uc and 6 uc models are exactly same. Also the center uc of 12 uc and 6 uc models are almost same electronic structure as the bulk. Therefore, we suggest that 6 uc model is enough to investigate the sensing mechanism.

4.3. Result and discussion

4.3.1. Mechanical and liquid exfoliation of MoS_2 single crystal

For comparative analysis of the gas sensors prepared by different exfoliation methods, two types of MoS_2 gas sensors were fabricated by mechanical and liquid exfoliation methods from the same MoS_2 single crystal (Figure 4.2a). Over the entire fabrication process, any chemicals which could modify chemical sensing properties of MoS_2 were not added. Figure 4.2b,c show scanning electron microscopy (SEM) and atomic force microscopy (AFM) images of the mechanically exfoliated MoS_2 microflakes and Figure 4.2d,e. show the images of the liquid-exfoliated MoS_2 nanoparticles deposited between the Pt IDEs. The mechanically exfoliated MoS_2 sensor was prepared by the scotch tape method,[121] in which the MoS_2 microflakes with an average size of 5 μm were sparsely attached to the substrate(Figure 4.3). On the other hand, the liquid-exfoliated MoS_2 nanoparticles were deposited on the Pt IDEs by drop-casting method and the nanoparticles were uniformly distributed with smaller sizes (~100 nm wide and ~15 nm high). These particle shapes imply a higher ratio of edge sites for the liquid-exfoliated MoS_2 nanoparticles.

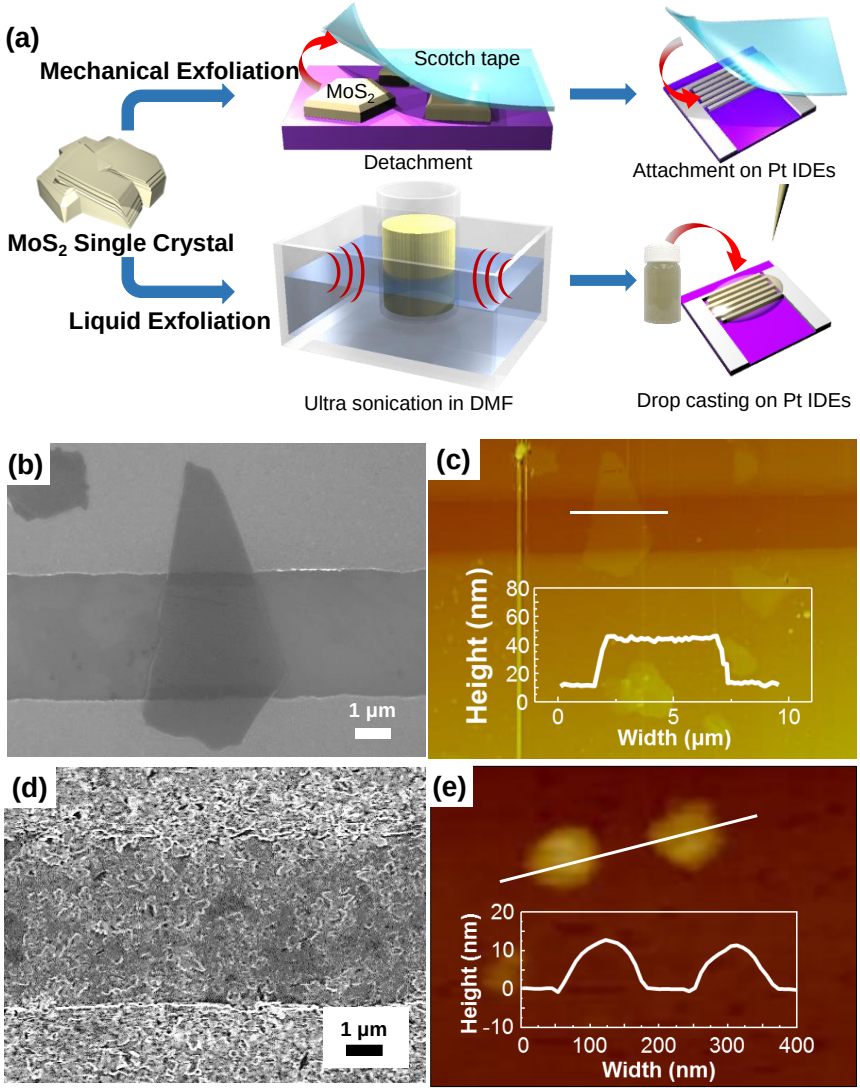

Figure 4.2. (a) Fabrication procedure of mechanically and liquid-exfoliated MoS_2 gas sensors. SEM and AFM images of (b,c) mechanically exfoliated MoS_2 microflakes and (d,e) liquid-exfoliated MoS_2 nanoparticles deposited between Pt IDEs.

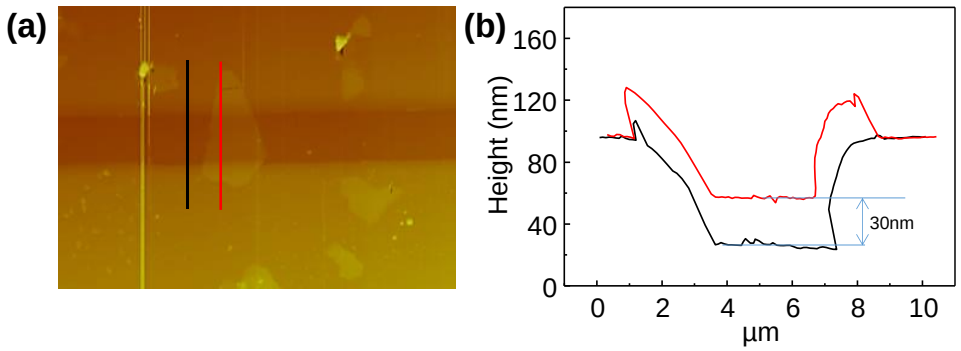

Figure 4.3. (a) AFM image and (b) height profiles of mechanically exfoliated MoS_2 microflake deposited between Pt IDEs (red line) and Pt IDEs without the MoS_2 microflakes (black line).

4.3.2. Characterization of liquid-exfoliated MoS_2 nanoparticles

Raman scattering was performed on a Raman spectrometer with excitation by 640 nm laser light. Figure 4.4a shows the Raman spectrum of the liquid-exfoliated MoS_2 nanoparticles, which reveals the in-plane vibrational modes of the Mo and S atoms (E^1_{2g}) and the out-of-plane vibrational mode of the S atoms (A_{1g}), respectively.[122, 123] Transmission electron microscopy (TEM) images were taken from different liquid-exfoliated MoS_2 nanoparticles (Figure 4.4b-d). The upper inset in each TEM image shows the corresponding electron diffraction pattern and the lower inset in Figure 4.4c is a high-resolution transmission electron microscopy (HRTEM) image of the liquid-exfoliated MoS_2 nanoparticles. The electron diffraction pattern obtained from the liquid-exfoliated MoS_2 nanoparticle reveals their single- crystalline nature. X-ray photoemission spectroscopy (XPS) was performed on as-deposited MoS_2 nanoparticles and the particles after heat treatment at 300 °C under ambient conditions (21% O_2 and 79% N_2). MoO_3 peak is observed after the heat treatment, which demonstrates the adsorption of oxygen on MoS_2 surfaces (Figure. 4.5).

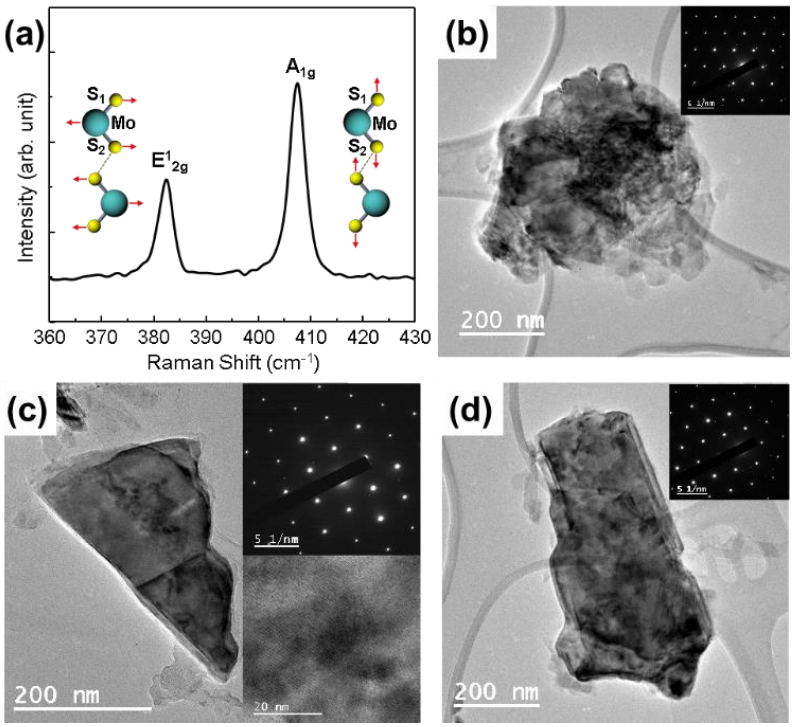

Figure 4.4. (a) Raman spectrum of liquid-exfoliated MoS_2. (b-d) TEM images of liquid-exfoliated MoS_2 nanoparticles with different shapes. Upper insets show corresponding electron diffraction pattern and lower inset in (c) is a HRTEM image of MoS_2 single crystal

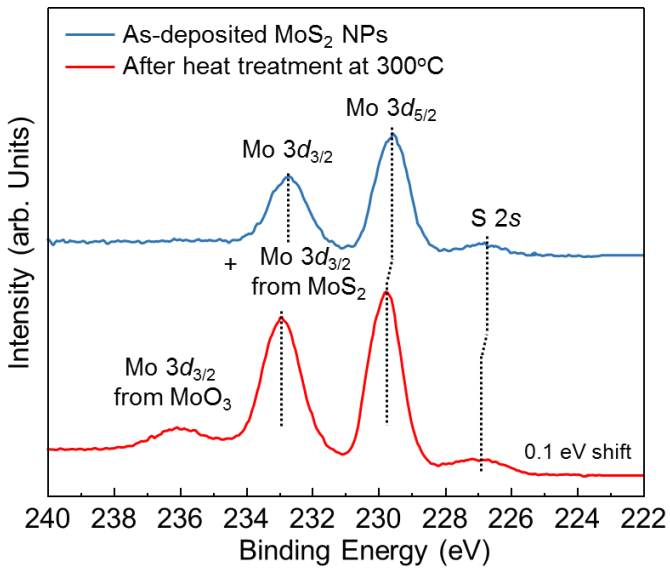

Figure 4.5. X-ray photoemission spectroscopy of as-deposited and after heat treatment liquid-exfoliated MoS_2.

4.3.3. Oxygen sensing properties

The response curves of the mechanically and liquid-exfoliated MoS_2 sensors were measured for O_2 concentrations up to 100% at elevated temperatures of 200, 300, and 400 °C (Figure 4.6a, b). The responses of the sensors were accurately determined by the ratio of the fully saturated resistances after exposure to the test gas (O_2) to the base resistances in nitrogen (N_2). The response is defined as R_{O2}/R_{N2} for the reducing gases where R_{O2} and R_{N2} denote resistances of the sensor in O_2 and in N_2, respectively. For the mechanically exfoliated MoS_2 sensor, the response to O_2 increased with increasing temperature but the response is as low as 1.5 at 400 °C and the sensor shows irreversible and retarded gas sensing behaviours. In addition, the sensor exhibits high electrical noise level with unstable base resistance. In contrast, the liquid-exfoliated MoS_2 sensor shows response as high as ~5700 at 400 °C. The liquid-exfoliated MoS_2 sensor exhibits higher responses to O_2 at all the elevated temperatures (Figure 4.6c). The sensors show huge differences in sensing properties according to their fabrication methods. It may be attributed to the modified surface-to-volume ratio and the consequent change in the number of edge sites.

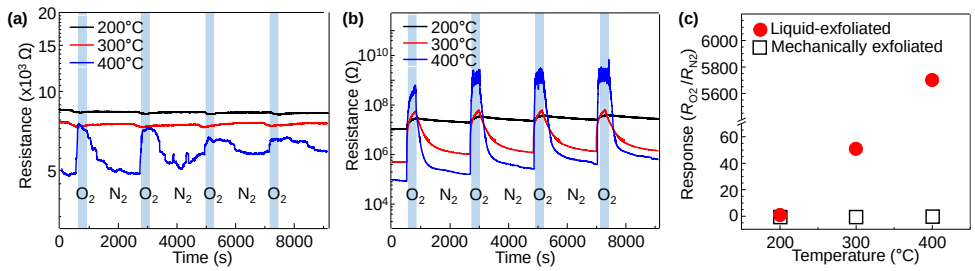

Figure 4.6. Response curves of a) mechanically exfoliated and b) liquid-exfoliated MoS_2 gas sensor to 100% O_2 at 200, 300, and 400 °C. c) Responses of mechanically and liquid-exfoliated MoS_2 gas sensors to 100% O_2 as a function of temperature.

Additional measurements were performed at 300 °C because the base resistance is unstable at the elevated temperature of 400 °C. Figure 4.7a shows a dynamic sensing transient of the liquid-exfoliated MoS_2 sensor to four consecutive pulses of 100% O_2 at 300 °C. The device shows high stability and full recovery to the four pulses of O_2 without shifting the base resistance or responses. The sensor was measured to 2—100% of O_2 at 300 °C as shown in Figure 4.7b. The responses of the liquid-exfoliated MoS_2 sensor were 8.69, 10.83, 12.25, 13.73, 17.4, 23.98, 29.96, 50.28, and 63.73 to 2, 5, 7, 10, 15, 25, 50, 75, and 100% O_2, respectively. The linear relationship between the response and O_2 gas concentration indicates that the operation capabilities of the sensor are reliable over a wide concentration range up to 100%. The slope of the plotted line, calculated to be 5453.6 ppm^{-1} represents the sensitivity of the sensor (Figure 4.7c). The plotted line does not seem to meet zero point when O_2 concentration goes to zero. However, the response will finally reach zero point because the response-concentration curve will not be in linear relationship for very low oxygen concentrations such as ppm levels.[124] This extremely high sensitivity and linearity to O_2 concentration are great merits of 2D MoS_2 with increased number of edge sites. As far as we are aware, oxygen gas sensors with these

outstanding sensing characteristics have never been achieved before this by chemoresistive method (Table 4.2).[125-129]

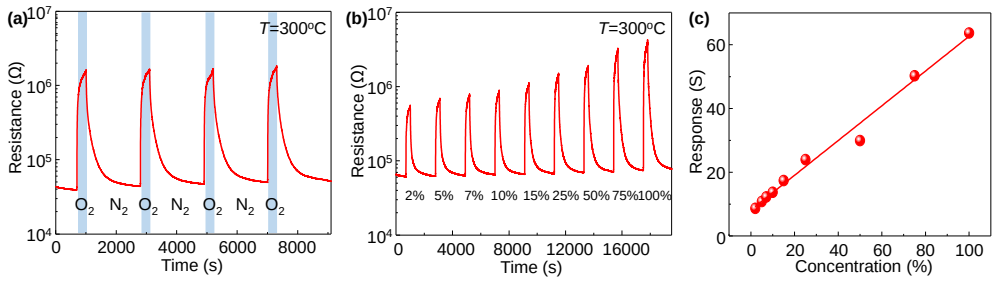

Figure 4.7. a) Response curves of liquid-exfoliated MoS_2 gas sensor to four pulses of 100% of O_2 at 300 °C. b) Response curves to different O_2 concentration at 300 °C. c) Linear fit of the responses as a function of O_2 at 300 °C.

Sensing material	**Synthesis method**	**Oxygen conc.**	**Response (S)**	**T_{sens} (°C)**	**Ref.**
MoS_2	Ultrasonication	100%	63.73	300	This study
$RBaCo_2O_5$	Solid state reaction	100%	~2	600	125
TiO_2	Sputtering	6000 ppm	~0.3	500	126
Ga_2O_3	Sputtering	60%	~4.5	900	127
CeO_2	Spray-pyrolysis	100%	~3	800	128
ZrO_2-doped CeO_2	Wet-chemical precipitation	100%	~ 1.1	800	129

Table 4.2. Gas sensing properties of different resistive oxygen gas sensors in the literatures.2-6

4.3.4. First-principles calculations

The experimental results suggest that the surface configurations of MoS_2 particles prepared by different exfoliation techniques are critical for gas-sensing properties, i.e., edge sites attract more O_2 molecules than clean surfaces. To confirm this, adsorption energies of O_2 on MoS_2 were investigated using first-principles calculations based on density functional theory (See Calculations).

First, we calculated the adsorption free energy (G_{ad}) of the O_2 molecule on the clean surface at temperature T and partial pressure of P as follows:

$$G_{\mathrm{ad}}(T,P) = G(MoS_2 + O_2) - G(MoS_2) - \mu_{O_2}(T,P) \quad (1)$$

where $G(MoS_2+O_2)$ and $G(MoS_2)$ indicate the free energies of the MoS_2 surface with an O_2 molecule adsorbed and clean MoS_2, respectively and $\mu_{O_2}(T,P)$ is the gas-phase chemical potential of the O_2 molecule. While $G(MoS_2+O_2)$ and $G(MoS_2)$ change little with respect to temperature and oxygen partial pressure, the experimental conditions are considered in $\mu_{O_2}(T,P)$ as follows:

$$\mu_{O_2}(T,P) = \mu_{O_2}(T,P^\circ) + k_B T \ln\left(\frac{P}{P^\circ}\right) \quad , \quad (2)$$

where P° is 1 atm. In addition,

$$\mu_{O_2}(T, P^\circ) = \Delta H + T\Delta S\, \mu_{O_2}(T, P^\circ) + \mu_{O_2}(O\ \mathrm{K}, P^\circ) \quad (3)$$

where ΔH and ΔS correspond to the enthalpy and entropy changes per molecule between T and 0 K at the standard pressure, respectively, and are obtained from thermodynamical tables.[130] In equation (3), $\mu_{O_2}(O\ \mathrm{K}, P^\circ)$ is equal to the total energy of the O_2 molecule. Because of the well- known overbinding of O_2 molecule in the density functional theory, we determined this value using the experimental binding energy of 5.23 eV.[131]

For the clean MoS_2 surface, the O_2 molecule was locally stable only at the top of S atoms. However, G_{ad}(300 °C, 1 atm) on this site is 1.72–3.21 eV, meaning that O_2 molecule would not bind to the clean MoS_2 surface (Figure 4.9, Table S3†). Next, we investigated energetics of O_2 adsorption on a semi-infinite stripe model of MoS_2. For the termination of MoS_2 edge, we considered clean Mo-edges (Figure 4.8a–c) and Mo-edges with S monomers (Figure 4.8d,e). We exclude S-edge model because the O_2 adsorption is locally unstable. The stable sites of O_2 adsorption on each MoS_2 edge are displayed in Figure 4.8a–e with respective G_{ad}(300 °C, 1atm) values shown under each figure. The G_{ad} values for Mo-edges (–3.30 to –2.51 eV) are much lower than those for

Mo-edges with S monomers (–0.57 to 1.30 eV) due to the strong affinity of oxygen to Mo.

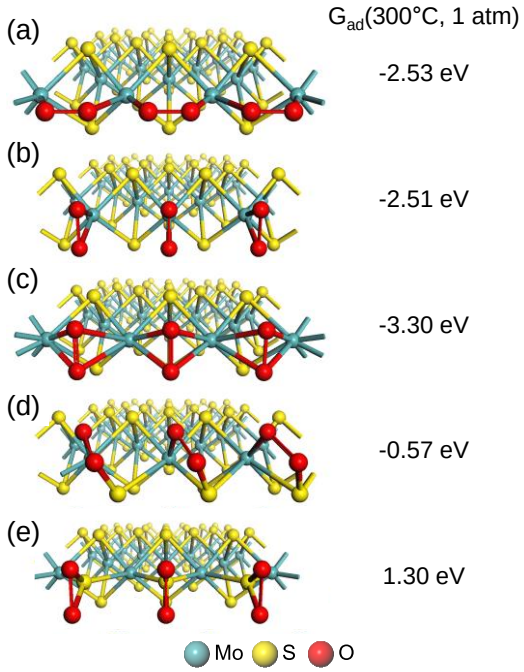

Figure 4.8. Stable sites of O_2 adsorption. (a-c) show locally stable configurations of O_2 adsorbed on clean Mo-edges. (d,e) show O_2 adsorption on Mo-edges with S monomers. The adsorption free energy at 300 °C and 1 atm [G_{ad}(300 °C, 1 atm)] is displayed

	(f)	(g)	(h)
G_{ads} (300°C, 1atm) (eV)	3.21	1.72	1.73

Table S3. Adsorption free energy of oxygen molecule on MoS_2 clean surface

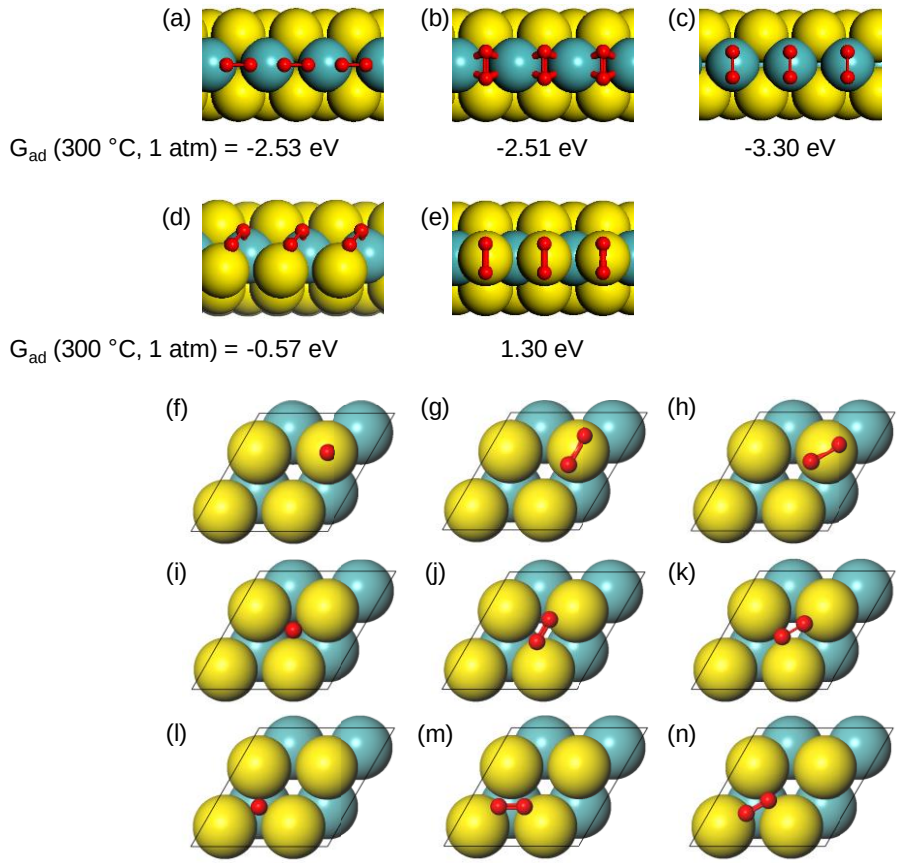

Figure 4.9. (a-e) Stable sites of O_2 adsorption.(a), (b) and (c) show locally stable configurations of O_2 adsorbed on clean Mo-edge. (d) and (e) show O_2 adsorption on Mo-edge with S monomer. The adsorption free energy at 300 °C and 1 atm [G_{ad}(300 °C, 1 atm)] is displayed under each figure. (f-n) Considered O_2 adsorption configurations on MoS_2 clean surface: (f) vertical O_2, (g) O_2 parallel to *a* axis, and (h) O_2 parallel to *a*+*b* axis on S top, (i) vertical O_2, (j) O_2 parallel to *a* axis, and (k) O_2 parallel to *a*+*b* axis on FCC center and (l) vertical O_2, (m) O_2 parallel to *a* axis, and (n) O_2 parallel to *a*+*b* axis on HCP center.

To consider the experimental condition more explicitly, we investigated the effect of oxygen partial pressure on G_{ad}'s at each temperature. Figure 4.10a, b show G_{ad} values on the Mo–S bridges (Figure 4.8d) and the S monomers (Figure 4.8e) of Mo-edges with S monomers, respectively. In Figure 4.10a, G_{ad} on the Mo–S bridges increases with decreasing P, crossing the zero point at low pressure. This indicates that O_2 desorbs from the Mo–S bridge sites. At lower temperatures of 200 and 300 °C, the crossing of the zero point occurs at much lower partial pressures. This is in qualitative agreement with the above experiment, in which the sensitivity of O_2 sensing improves at high temperatures. On the other hand, Figure 4.10b indicates that O_2 does not bind on the S monomers of Mo-edges with S monomers. The G_{ad} values on Mo-edges (not shown) confirm that O_2 binds at these edges too strongly to show reversible adsorption/desorption. Therefore, it is clear that, only the Mo–S bridges in Figure 4.8d allow for reversible O_2 adsorption/desorption among the considered binding sites. We have also conducted calculations for the dependence of O_2 adsorption energies for Mo-S bridge sites on O_2 coverage was investigated to explain the linear relationship at high oxygen concentrations (Figure 4.11).

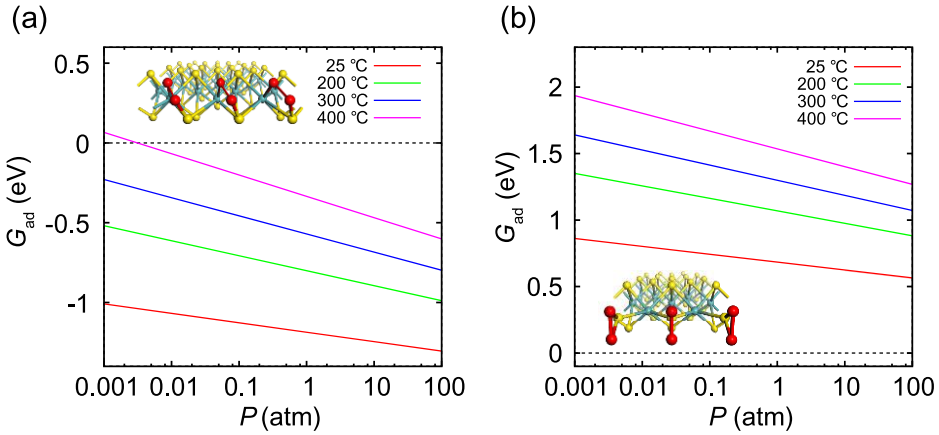

Figure 4.10. Adsorption energy of O_2 molecules on (a) Mo-S bridge sites of Mo-edges with S monomers and (b) S monomers of Mo-edges with S monomers with respect to temperature and oxygen partial pressure.

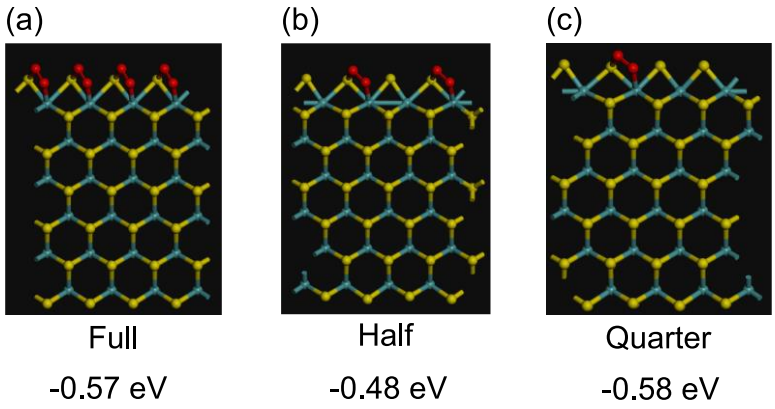

Figure 4.11. O_2 adsorption energy on Mo-S bridge sites of Mo-edges with S monomer: (a) full, (b) half and(c) quarter O_2 coverage.

O_2 adsorption energy on Mo-S bridge sites of Mo-edge with S monomer was calculated depending on O_2 coverage, defined as the ratio of the number of adsorbed oxygen to available adsorption sites. The adsorption free energy at 300 °C, 1 atm for O_2 coverage of 1, 0.5, and 0.25 are -0.57, -0.48 and -0.58 eV, respectively. This simulation demonstrates the adsorption free energies are hardly affected by O_2 coverage. Therefore, the concentration of O_2 does not influence on the linear relationship in large oxygen concentration.

To understand how O_2 adsorption influences the conductivity of a MoS_2 film, we examined the electronic structure of the clean Mo-edges with S monomers both with and without O_2 adsorption. Figure 4.12a, b show the band structure (left) and density of states projected on the edge atoms (right) for each model, respectively. The charge distribution near the Fermi level is shown in the bottom figures. In the band structure of the clean Mo–S bridges, the energy band crosses the Fermi level, indicating the metallic character. The colour intensity of the crossing band indicates that the metallic states are localized along the edges. The charge density distribution in the bottom figure shows that the metallic states originate mainly from the d orbitals of Mo atoms on the edges. This was also reported in previous theoretical studies.[132] On the other hand, with O_2 adsorption on the Mo–S bridge sites, the electronic structure undergoes substantial changes (Figure 4.12b). The metallic band in Figure 4.12a is significantly flattened, meaning that the effective electron mass becomes much higher than that for the clean edges. The large effective electron mass would directly lower the electrical conductivity according to the semiclassical Drude model. The charge distribution in the bottom of Figure 4.12b also shows that the electronic

states are more localized along the edges in comparison with Figure 4.12a.

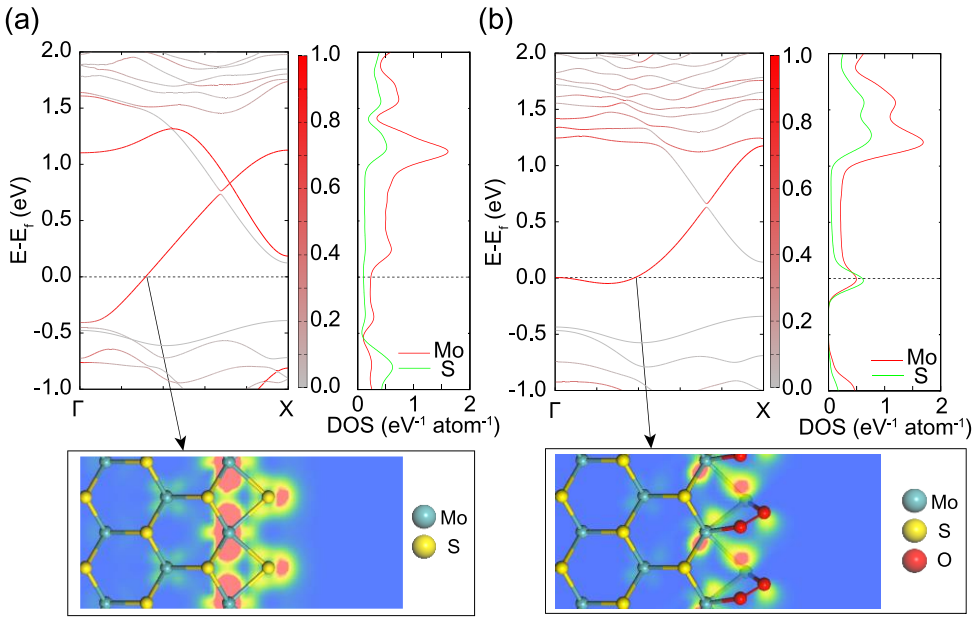

Figure 4.12. Band structure, density of states (DOS) of edge atoms and charge density distribution near the Fermi level of (a) clean Mo-edge with S monomer and (b) O_2 adsorbed Mo-edge with S monomer on Mo-S bridge site, respectively. The color intensity in band structure is proportional to the weight of the corresponding state on the edge atoms; red and gray mean edge atoms and the other atoms, respectively. Red and blue in charge density distribution indicate the maximum and zero electronic densities, respectively.

4.3.5. Sensing properties to other gases and the mechanisms

Figure 4.13a shows dynamic sensing transients of the liquid-exfoliated MoS_2 sensor and SnO_2 nanosphere sensor to 50 ppm of C_2H_5OH, CH_3COCH_3, C_7H_8, C_6H_6, CH_3CHO, CO, NH_3, and H_2, 3% of CO_2, 2 ppm of H_2S, and 5 ppm of NO_2 at 300 °C. The SnO_2 sensor was fabricated using sputter, experimental details of which were mentioned in our previous report.[133] Their responses are exhibited in Figure 4.13b. In previous studies, it has been demonstrated that pre-adsorbed O_2 molecules on semiconducting metal oxides play a major role in the sensing reaction to reducing gases.[112-118] Similarly, the liquid-exfoliated MoS_2 sensor exhibits high selectivity for C_2H_5OH, because of a large number of pre-adsorbed O_2 molecules on the MoS_2. On the other hand, the response of the liquid-exfoliated MoS_2 sensor to NO_2, 5, is lower than that of the SnO_2 sensor, 215. Direct adsorption is proposed for NO_2 without any interaction with pre-adsorbed molecules ($NO_2 + e^- \rightarrow NO_2^-$).[134] Since the liquid-exfoliated MoS_2 exhibits extremely high oxygen sensitivity, most adsorption sites may have been occupied with pre-adsorbed O_2 molecules. Accordingly, no unoccupied adsorption sites were left for NO_2. Thus, the liquid-exfoliated MoS_2 sensor has comparatively higher selectivity to C_2H_5OH and lower response to NO_2 than the SnO_2 sensor. Furthermore, to evaluate detection limit for C_2H_5OH, the response of the MoS_2 sensor was measured over 3–50 ppm

concentration range. The minimum detection limit of the proposed sensor for C_2H_5OH is determined to be 49.96 ppb at 300 °C (Figure 4.14).[5, 47]

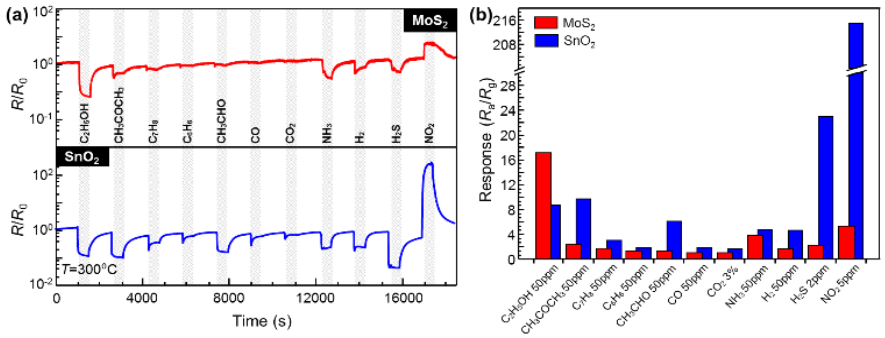

Figure 4.13. (a) Sensing transients of liquid-exfoliated MoS_2 and SnO_2 nanosphere gas sensors to various gases. (b) Response of liquid-exfoliated MoS_2 nanoparticle and SnO_2 nanosphere gas sensors to various gases

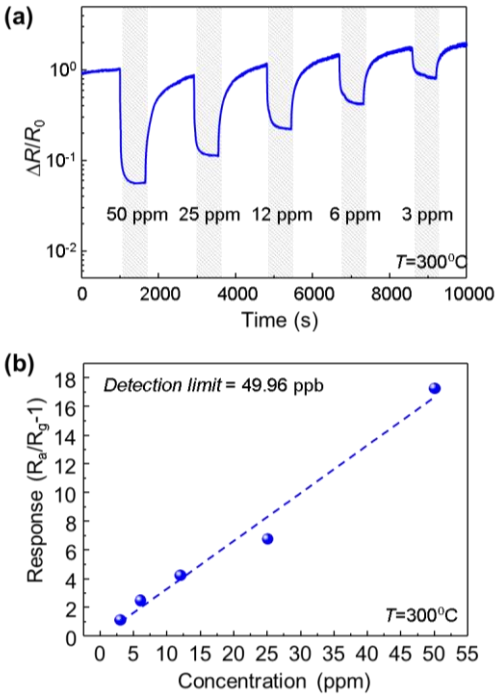

Figure 4.14. (a) Gas sensing transients of liquid-exfoliated MoS_2 to different C_2H_5OH concentration at 300ºC. (b) Linear fit of responses as a function of C_2H_5OH concentration at 300ºC.

4.4 Conclusion

In conclusion, we have reported the high oxygen sensitivity of liquid-exfoliated MoS_2 gas sensor prepared by facile fabrication steps. The liquid-exfoliated MoS_2 gas sensor demonstrates high responses with wide concentration range stability to O_2. The high response of liquid-exfoliated MoS_2 nanoparticles to O_2 molecules is attributed to the semiconducting nature of MoS_2 and the increased number of edge sites developed by the liquid exfoliation. First-principles calculations revealed the critical role in O_2 sensing played by the edge sites that can be easily modified by fabrication procedures. We believe that the outstanding device performance demonstrated in this study has proven the potential of MoS_2-based oxygen gas sensors in practical applications.

REERENCES

1. Wang, C.; Yin, L.; Zhang, L.; Xiang, D.; Gao, R. Metal Oxide Gas Sensors: Sensitivity and Influencing Factors. *Sensors* **2010**, *10*, 2088-2106.
2. Bochenkov, V.; Sergeev, G. Sensitivity, Selectivity, and Stability of Gas-Sensitive Metal-Oxide Nanostructures. *Metal oxide nanostructures and their applications* **2010**, *3*, 31-52.
3. Barsan, N.; Koziej, D.; Weimar, U. Metal Oxide-Based Gas Sensor Research: How to? *Sens. Actuators, B* **2007**, *121*, 18-35.
4. Choopun, S.; Hongsith, N.; Wongrat, E. Metal-Oxide Nanowires for Gas Sensors. In *Nanowires-Recent Advances*, InTech: 2012.
5. Li, J.; Lu, Y.; Ye, Q.; Cinke, M.; Han, J.; Meyyappan, M. Carbon Nanotube Sensors for Gas and Organic Vapor Detection. *Nano Lett.* **2003**, *3*, 929-933.
6. Schedin, F.; Geim, A.; Morozov, S.; Hill, E.; Blake, P.; Katsnelson, M.; Novoselov, K. Detection of Individual Gas Molecules Adsorbed on Graphene. *Nat. Mater.* **2007**, *6*, 652-655.
7. Lu, G.; Park, S.; Yu, K.; Ruoff, R. S.; Ocola, L. E.; Rosenmann, D.; Chen, J. Toward Practical Gas Sensing with Highly Reduced Graphene Oxide: A New Signal Processing Method to Circumvent Run-to-Run and Device-to-Device Variations. *ACS Nano* **2011**, *5*, 1154-1164.
8. Fowler, J. D.; Allen, M. J.; Tung, V. C.; Yang, Y.; Kaner, R. B.; Weiller, B. H. Practical Chemical Sensors from Chemically Derived Graphene. *ACS Nano* **2009**, *3*, 301-306.
9. Dan, Y.; Lu, Y.; Kybert, N. J.; Luo, Z.; Johnson, A. C. Intrinsic Response of Graphene Vapor Sensors. *Nano Lett.* **2009**, *9*, 1472-1475.

10. Robinson, J. T.; Perkins, F. K.; Snow, E. S.; Wei, Z.; Sheehan, P. E. Reduced Graphene Oxide Molecular Sensors. *Nano Lett.* **2008**, *8*, 3137-3140.
11. Lu, G.; Ocola, L. E.; Chen, J. Gas Detection Using Low-Temperature Reduced Graphene Oxide Sheets. *Appl. Phys. Lett.* **2009**, *94*, 083111.
12. Lipatov, A.; Varezhnikov, A.; Wilson, P.; Sysoev, V.; Kolmakov, A.; Sinitskii, A. Highly Selective Gas Sensor Arrays Based on Thermally Reduced Graphene Oxide. *Nanoscale* **2013**, *5*, 5426-5434.
13. Cui, S.; Pu, H.; Mattson, E. C.; Wen, Z.; Chang, J.; Hou, Y.; Hirschmugl, C. J.; Chen, J. Ultrasensitive Chemical Sensing Through Facile Tuning Defects and Functional Groups in Reduced Graphene Oxide. *Anal. Chem.* **2014**, *86*, 7516-7522.
14. Ou, J. Z.; Ge, W.; Carey, B.; Daeneke, T.; Rotbart, A.; Shan, W.; Wang, Y.; Fu, Z.; Chrimes, A. F.; Wlodarski, W. Physisorption-Based Charge Transfer in Two-dimensional SnS_2 for Selective and Reversible NO_2 Gas Sensing. *ACS Nano* **2015**, *9*, 10313-10323.
15. Medina, H.; Li, J.-G.; Su, T.-Y.; Lan, Y.-W.; Lee, S.-H.; Chen, C.-W.; Chen, Y.-Z.; Manikandan, A.; Tsai, S.-H.; Navabi, A. Wafer-Scale Growth of WSe2 Monolayers Toward Phase-Engineered Hybrid WO x/WSe_2 Films with Sub-ppb NO_x Gas Sensing by a Low-Temperature Plasma-Assisted Selenization Process. *Chem. Mater.* **2017**, *29*, 1587-1598.
16. Late, D. J.; Huang, Y.-K.; Liu, B.; Acharya, J.; Shirodkar, S. N.; Luo, J.; Yan, A.; Charles, D.; Waghmare, U. V.; Dravid, V. P. Sensing Behavior of Atomically Thin-Layered MoS_2 Transistors. *ACS Nano* **2013**, *7*, 4879-4891.

17. Jhon, Y. I.; Kim, Y.; Park, J.; Kim, J. H.; Lee, T.; Seo, M.; Jhon, Y. M. Significant Exciton Brightening in Monolayer Tungsten Disulfides via Fluorination: n-Type Gas Sensing Semiconductors. *Adv. Funct. Mater.* **2016**, *26*, 7551-7559.
18. Cho, S.-Y.; Kim, S. J.; Lee, Y.; Kim, J.-S.; Jung, W.-B.; Yoo, H.-W.; Kim, J.; Jung, H.-T. Highly Enhanced Gas Adsorption Properties in Vertically Aligned MoS_2 Layers. *ACS Nano* **2015**, *9*, 9314-9321.
19. Cho, S. Y.; Lee, Y.; Koh, H. J.; Jung, H.; Kim, J. S.; Yoo, H. W.; Kim, J.; Jung, H. T. Superior Chemical Sensing Performance of Black Phosphorus: Comparison with MoS_2 and Graphene. *Adv. Mater.* **2016**, *28*, 7020-7028.
20. Cho, B.; Kim, A. R.; Kim, D. J.; Chung, H.-S.; Choi, S. Y.; Kwon, J.-D.; Park, S. W.; Kim, Y.; Lee, B. H.; Lee, K. H. Two-Dimensional Atomic-Layered Alloy Junctions for High-Performance Wearable Chemical Sensor. *ACS Appl. Mater. Interfaces* **2016**, *8*, 19635-19642.
21. Cho, B.; Hahm, M. G.; Choi, M.; Yoon, J.; Kim, A. R.; Lee, Y.-J.; Park, S.-G.; Kwon, J.-D.; Kim, C. S.; Song, M. Charge-Transfer-Based Gas Sensing Using Atomic-Layer MoS_2. *Sci. Rep.* **2015**, *5*.
22. Swan, M. Sensor Mania! The Internet of Things, Wearable Computing, Objective Metrics, and the Quantified Self 2.0. *J. Sens. Actuator Networks* **2012**, *1*, 217-253.
23. Miorandi, D.; Sicari, S.; De Pellegrini, F.; Chlamtac, I. Internet of things: Vision, Applications and Research Challenges. *Ad Hoc Netw.* **2012**, *10*, 1497-1516.
24. Nanto, H.; Sokooshi, H.; Kawai, T. Aluminum-Doped ZnO Thin Film Gas Sensor Capable of Detecting Freshness of Sea Foods. *Sens. Actuators, B* **1993**, *14*, 715-717.

25. Yamazoe, N. Toward Innovations of Gas Sensor Technology. *Sens. Actuators, B* **2005**, *108*, 2-14.
26. Moos, R.; Müller, R.; Plog, C.; Knezevic, A.; Leye, H.; Irion, E.; Braun, T.; Marquardt, K.-J.; Binder, K. Selective Ammonia Exhaust Gas Sensor for Automotive Applications. *Sens. Actuators, B* **2002**, *83*, 181-189.
27. Capone, S.; Forleo, A.; Francioso, L.; Rella, R.; Siciliano, P.; Spadavecchia, J.; Presicce, D.; Taurino, A. Solid State Gas Sensors: State of the Art and Future Activities. *J. Optoelectron.: Adv. Mater. Devices* **2003**, *5*, 1335-1348.
28. Yamazoe, N.; Shimanoe, K. New Perspectives of Gas Sensor Technology. *Sens. Actuators, B* **2009**, *138*, 100-107.
29. Moon, H. G.; Shim, Y.-S.; Kim, D. H.; Jeong, H. Y.; Jeong, M.; Jung, J. Y.; Han, S. M.; Kim, J. K.; Kim, J.-S.; Park, H.-H. Self-Activated Ultrahigh Chemosensitivity of Oxide Thin Film Nanostructures for Transparent Sensors. *Sci. Rep.* **2012**, *2*.
30. Yamazoe, N. New Approaches for Improving Semiconductor Gas Sensors. *Sens. Actuators, B* **1991**, *5*, 7-19.
31. Eranna, G.; Joshi, B.; Runthala, D.; Gupta, R. Oxide Materials for Development of Integrated Gas Sensors—A Comprehensive Review. *Crit. Rev. Solid State Mater. Sci.* **2004**, *29*, 111-188.
32. He, Q.; Sudibya, H. G.; Yin, Z.; Wu, S.; Li, H.; Boey, F.; Huang, W.; Chen, P.; Zhang, H. Centimeter-Long and Large-Scale Micropatterns of Reduced Graphene Oxide Films: Fabrication and Sensing Applications. *ACS Nano* **2010**, *4*, 3201-3208.
33. Li, W.; Geng, X.; Guo, Y.; Rong, J.; Gong, Y.; Wu, L.; Zhang, X.; Li, P.; Xu, J.; Cheng, G. Reduced Graphene Oxide Electrically Contacted

Graphene Sensor for Highly Sensitive Nitric Oxide Detection. *ACS Nano* **2011**, *5*, 6955-6961.

34. Nomani, M. W.; Shishir, R.; Qazi, M.; Diwan, D.; Shields, V.; Spencer, M.; Tompa, G. S.; Sbrockey, N. M.; Koley, G. Highly Sensitive and Selective Detection of NO_2 Using Epitaxial Graphene on 6H-SiC. *Sens. Actuators, B* **2010**, *150*, 301-307.
35. Yu, K.; Wang, P.; Lu, G.; Chen, K.-H.; Bo, Z.; Chen, J. Patterning Vertically Oriented Graphene Sheets for Nanodevice Applications. *J. Phys. Chem. Lett.* **2011**, *2*, 537-542.
36. Tang, S.; Cao, Z. Adsorption of Nitrogen Oxides on Graphene and Graphene Oxides: Insights from Density Functional Calculations. *J. Chem. Phys.* **2011**, *134*, 044710.
37. Ueda, T.; Bhuiyan, M.; Norimatsu, H.; Katsuki, S.; Ikegami, T.; Mitsugi, F. Development of Carbon Nanotube-Based Gas Sensors for NO_x Gas Detection Working at Low Temperature. *Physica. E Low Dimens. Syst. Nanostruct.* **2008**, *40*, 2272-2277.
38. Choi, H.; Choi, J. S.; Kim, J. S.; Choe, J. H.; Chung, K. H.; Shin, J. W.; Kim, J. T.; Youn, D. H.; Kim, K. C.; Lee, J. I. Flexible and Transparent Gas Molecule Sensor Integrated with Sensing and Heating Graphene Layers. *Small* **2014**, *10*, 3685-3691.
39. Sui, D.; Huang, Y.; Huang, L.; Liang, J.; Ma, Y.; Chen, Y. Flexible and Transparent Electrothermal Film Heaters Based on Graphene Materials. *Small* **2011**, *7*, 3186-3192.
40. Cançado, L. G.; Jorio, A.; Ferreira, E. M.; Stavale, F.; Achete, C.; Capaz, R.; Moutinho, M.; Lombardo, A.; Kulmala, T.; Ferrari, A. Quantifying Defects in Graphene *via* Raman Spectroscopy at Different Excitation Energies. *Nano Lett.* **2011**, *11*, 3190-3196.

41. Kumar, B.; Min, K.; Bashirzadeh, M.; Farimani, A. B.; Bae, M.-H.; Estrada, D.; Kim, Y.; Yasaei, P.; Park, Y.; Pop, E. The Role of External Defects in Chemical Sensing of Graphene Field-Effect Transistors. *Nano Lett.* **2013**, *13*, 1962-1968.
42. Yavari, F.; Chen, Z.; Thomas, A. V.; Ren, W.; Cheng, H.-M.; Koratkar, N. High Sensitivity Gas Detection Using A Macroscopic Three-Dimensional Graphene Foam Network. *Sci. Rep.* **2011**, *1*.
43. Karaduman, I.; Er, E.; Çelikkan, H.; Acar, S. A New Generation Gas Sensing Material Based on High-Quality Graphene. *Sens. Actuators, B* **2015**, *221*, 1188-1194.
44. Jeong, H. Y.; Lee, D.-S.; Choi, H. K.; Lee, D. H.; Kim, J.-E.; Yong Lee, J.; Lee, W. J.; Kim, S. O.; Choi, S.-Y. Flexible Room-Temperature NO_2 Gas Sensors Based on Carbon Nanotubes/Reduced Graphene Hybrid Films. *Appl. Phys. Lett.* **2010**, *96*, 213105-213105-3.
45. Chung, M. G.; Kim, D. H.; Lee, H. M.; Kim, T.; Choi, J. H.; kyun Seo, D.; Yoo, J.-B.; Hong, S.-H.; Kang, T. J.; Kim, Y. H. Highly Sensitive NO_2 Gas Sensor Based on Ozone Treated Graphene. *Sens. Actuators, B* **2012**, *166*, 172-176.
46. Yasaei, P.; Kumar, B.; Hantehzadeh, R.; Kayyalha, M.; Baskin, A.; Repnin, N.; Wang, C.; Klie, R. F.; Chen, Y. P.; Král, P. Chemical Sensing with Switchable Transport Channels in Graphene Grain Boundaries. *Nat. Commun.* **2014**, *5*.
47. Dua, V.; Surwade, S. P.; Ammu, S.; Agnihotra, S. R.; Jain, S.; Roberts, K. E.; Park, S.; Ruoff, R. S.; Manohar, S. K. All-Organic Vapor Sensor Using Inkjet-Printed Reduced Graphene Oxide. *Angew. Chem., Int. Ed.* **2010**, *49*, 2154-2157.

48. Koziej, D.; Bârsan, N.; Weimar, U.; Szuber, J.; Shimanoe, K.; Yamazoe, N. Water–Oxygen Interplay on Tin Dioxide Surface: Implication on Gas Sensing. *Chem. Phys. Lett.* **2005**, *410*, 321-323.

49. Vlachos, D.; Skafidas, P.; Avaritsiotis, J. The Effect of Humidity on Tin-Oxide Thick-Film Gas Sensors in the Presence of Reducing and Combustible Gases. *Sens. Actuators, B* **1995**, *25*, 491-494.

50. Dieguez, A.; Vila, A.; Cabot, A.; Romano-Rodrıguez, A.; Morante, J.; Kappler, J.; Barsan, N.; Weimar, U.; Göpel, W. Influence on the Gas Sensor Performances of the Metal Chemical States Introduced by Impregnation of Calcinated SnO_2 Sol–Gel Nanocrystals. *Sens. Actuators, B* **2000**, *68*, 94-99.

51. Neri, G.; Bonavita, A.; Galvagno, S.; Siciliano, P.; Capone, S. CO and NO_2 Sensing Properties of Doped-Fe_2O_3 Thin Films Prepared by LPD. *Sens. Actuators, B* **2002**, *82*, 40-47.

52. Bae, S.; Kim, H.; Lee, Y.; Xu, X.; Park, J.-S.; Zheng, Y.; Balakrishnan, J.; Lei, T.; Kim, H. R.; Song, Y. I. Roll-to-Roll Production of 30-Inch Graphene Films for Transparent Electrodes. *Nat. Nanotechnol.* **2010**, *5*, 574-578.

53. Li, X.; Zhu, Y.; Cai, W.; Borysiak, M.; Han, B.; Chen, D.; Piner, R. D.; Colombo, L.; Ruoff, R. S. Transfer of Large-Area Graphene Films for High-Performance Transparent Conductive Electrodes. *Nano Lett.* **2009**, *9*, 4359-4363.

54. Kim, K. S.; Zhao, Y.; Jang, H.; Lee, S. Y.; Kim, J. M.; Kim, K. S.; Ahn, J.-H.; Kim, P.; Choi, J.-Y.; Hong, B. H. Large-Scale Pattern Growth of Graphene Films for Stretchable Transparent Electrodes. *Nature* **2009**, *457*, 706-710.

55. Simon, I.; Bârsan, N.; Bauer, M.; Weimar, U. Micromachined Metal Oxide Gas Sensors: Opportunities to Improve Sensor Performance. *Sens. Actuators, B* **2001**, *73*, 1-26.
56. Elmi, I.; Zampolli, S.; Cozzani, E.; Mancarella, F.; Cardinali, G. Development of Ultra-Low-Power Consumption MOX Sensors with Ppb-Level VOC Detection Capabilities for Emerging Applications. *Sens. Actuators, B* **2008**, *135*, 342-351.
57. Radovic, L. R. Active Sites in Graphene and the Mechanism of CO_2 Formation in Carbon Oxidation. *J. Am. Chem. Soc,* **2009**, *131*, 17166-17175.
58. Perkins, F. K.; Friedman, A. L.; Cobas, E.; Campbell, P.; Jernigan, G.; Jonker, B. T. Chemical Vapor Sensing with Monolayer MoS_2. *Nano Lett.* **2013**, *13*, 668-673.
59. Liu, B.; Chen, L.; Liu, G.; Abbas, A. N.; Fathi, M.; Zhou, C. High-Performance Chemical Sensing Using Schottky-Contacted Chemical Vapor Deposition Grown Monolayer MoS_2 Transistors. *ACS Nano* **2014**, *8*, 5304-5314.
60. Ko, K. Y.; Song, J.-G.; Kim, Y.; Choi, T.; Shin, S.; Lee, C. W.; Lee, K.; Koo, J.; Lee, H.; Kim, J. Improvement of Gas-Sensing Performance of Large-Area Tungsten Disulfide Nanosheets by Surface Functionalization. *ACS Nano* **2016**, *10*, 9287-9296.
61. Kim, Y. H.; Kim, K. Y.; Choi, Y. R.; Shim, Y.-S.; Jeon, J.-M.; Lee, J.-H.; Kim, S. Y.; Han, S.; Jang, H. W. Ultrasensitive Reversible Oxygen Sensing by Using Liquid-Exfoliated MoS_2 nanoparticles. *J. Mater. Chem. A* **2016**, *4*, 6070-6076.

62. Huo, N.; Yang, S.; Wei, Z.; Li, S.-S.; Xia, J.-B.; Li, J. Photoresponsive and Gas Sensing Field-Effect Transistors Based on Multilayer WS_2 Nnanoflakes. *Sci. Rep.* **2014**, *4*.

63. He, Q.; Zeng, Z.; Yin, Z.; Li, H.; Wu, S.; Huang, X.; Zhang, H. Fabrication of Flexible MoS_2 Thin-Film Transistor Arrays for Practical Gas-Sensing Applications. *Small* **2012**, *8*, 2994-2999.

64. Kim, Y. H.; Kim, S. J.; Kim, Y.-J.; Shim, Y.-S.; Kim, S. Y.; Hong, B. H.; Jang, H. W. Self-Activated Transparent All-Graphene Gas Sensor with Endurance to Humidity and Mechanical Bending. *ACS Nano* **2015**, *9*, 10453-10460.

65. Choi, Y. R.; Yoon, Y.-G.; Choi, K. S.; Kang, J. H.; Shim, Y.-S.; Kim, Y. H.; Chang, H. J.; Lee, J.-H.; Park, C. R.; Kim, S. Y. Role of Oxygen Functional Groups in Graphene Oxide for Reversible Room-Temperature NO_2 Sensing. *Carbon* **2015**, *91*, 178-187.

66. Yuan, W.; Liu, A.; Huang, L.; Li, C.; Shi, G. High-Performance NO_2 Sensors Based on Chemically Modified Graphene. *Adv. Mater.* **2013**, *25*, 766-771.

67. Wang, J.; Rathi, S.; Singh, B.; Lee, I.; Joh, H.-I.; Kim, G.-H. Alternating Current Dielectrophoresis Optimization of Pt-Decorated Graphene Oxide Nanostructures for Proficient Hydrogen Gas Sensor. *ACS Appl. Mater. Interfaces* **2015**, *7*, 13768-13775.

68. Song, H.; Zhang, L.; He, C.; Qu, Y.; Tian, Y.; Lv, Y. Graphene Sheets Decorated with SnO_2 Nanoparticles: In Situ Synthesis and Highly Efficient Materials for Cataluminescence Gas Sensors. *J. Mater. Chem.* **2011**, *21*, 5972-5977.

69. Kaniyoor, A.; Jafri, R. I.; Arockiadoss, T.; Ramaprabhu, S. Nanostructured Pt Decorated Graphene and Multi Walled Carbon

Nanotube Based Room Temperature Hydrogen Gas Sensor. *Nanoscale* **2009**, *1*, 382-386.

70. Withers, F.; Dubois, M.; Savchenko, A. K. Electron Properties of Fluorinated Single-Layer Graphene Transistors. *Phys. Rev. B* **2010**, *82*, 073403.
71. Wang, Z.; Wang, J.; Li, Z.; Gong, P.; Liu, X.; Zhang, L.; Ren, J.; Wang, H.; Yang, S. Synthesis of Fluorinated Graphene with Tunable Degree of Fluorination. *Carbon* **2012**, *50*, 5403-5410.
72. Wang, X.; Dai, Y.; Gao, J.; Huang, J.; Li, B.; Fan, C.; Yang, J.; Liu, X. High-Yield Production of Highly Fluorinated Graphene by Direct Heating Fluorination of Graphene-Oxide. *ACS Appl. Mater. Interfaces* **2013**, *5*, 8294-8299.
73. Sudeep, P. M.; Narayanan, T. N.; Ganesan, A.; Shaijumon, M. M.; Yang, H.; Ozden, S.; Patra, P. K.; Pasquali, M.; Vajtai, R.; Ganguli, S. Covalently Interconnected Three-Dimensional Graphene Oxide Solids. *ACS Nano* **2013**, *7*, 7034-7040.
74. Sudeep, P.; Taha-Tijerina, J.; Ajayan, P.; Narayanan, T.; Anantharaman, M. Nanofluids Based on Fluorinated Graphene Oxide for Efficient Thermal Management. *RSC Adv.* **2014**, *4*, 24887-24892.
75. Romero-Aburto, R.; Narayanan, T.; Nagaoka, Y.; Hasumura, T.; Mitcham, T. M.; Fukuda, T.; Cox, P. J.; Bouchard, R. R.; Maekawa, T.; Kumar, D. S. Fluorinated Graphene Oxide; A New Multimodal Material for Biological Applications. *Adv. Mater.* **2013**, *25*, 5632-5637.
76. Robinson, J. T.; Burgess, J. S.; Junkermeier, C. E.; Badescu, S. C.; Reinecke, T. L.; Perkins, F. K.; Zalalutdniov, M. K.; Baldwin, J. W.; Culbertson, J. C.; Sheehan, P. E. Properties of Fluorinated Graphene Films. *Nano Lett.* **2010**, *10*, 3001-3005.

77. Park, M.-S.; Kim, K. H.; Kim, M.-J.; Lee, Y.-S. NH_3 Gas Sensing Properties of a Gas Sensor Based on Fluorinated Graphene Oxide. *Colloids Surf., A* **2016**, *490*, 104-109.
78. Lee, W. H.; Suk, J. W.; Chou, H.; Lee, J.; Hao, Y.; Wu, Y.; Piner, R.; Akinwande, D.; Kim, K. S.; Ruoff, R. S. Selective-Area Fluorination of Graphene with Fluoropolymer and Laser Irradiation. *Nano Lett.* **2012**, *12*, 2374-2378.
79. Zhang, H.; Fan, L.; Dong, H.; Zhang, P.; Nie, K.; Zhong, J.; Li, Y.; Guo, J.; Sun, X. Spectroscopic Investigation of Plasma-Fluorinated Monolayer Graphene and Application for Gas Sensing. *ACS Appl. Mater. Interfaces* **2016**, *8*, 8652-8661.
80. Tang, S.; Cao, Z. Adsorption and Dissociation of Ammonia on Graphene Oxides: A First-Principles Study. *J. Phys. Chem. C* **2012**, *116*, 8778-8791.
81. Mattevi, C.; Eda, G.; Agnoli, S.; Miller, S.; Mkhoyan, K. A.; Celik, O.; Mastrogiovanni, D.; Granozzi, G.; Garfunkel, E.; Chhowalla, M. Evolution of Electrical, Chemical, and Structural Properties of Transparent and Conducting Chemically Derived Graphene Thin Films. *Adv. Funct. Mater.* **2009**, *19*, 2577-2583.
82. Loh, K. P.; Bao, Q.; Eda, G.; Chhowalla, M. Graphene Oxide as a Chemically Tunable Platform for Optical Applications. *Nat. Chem.* **2010**, *2*, 1015-1024.
83. Gómez-Navarro, C.; Meyer, J. C.; Sundaram, R. S.; Chuvilin, A.; Kurasch, S.; Burghard, M.; Kern, K.; Kaiser, U. Atomic Structure of Reduced Graphene Oxide. *Nano Lett.* **2010**, *10*, 1144-1148.
84. Kovtyukhova, N. I.; Ollivier, P. J.; Martin, B. R.; Mallouk, T. E.; Chizhik, S. A.; Buzaneva, E. V.; Gorchinskiy, A. D. Layer-by-Layer

Assembly of Ultrathin Composite Films from Micron-Sized Graphite Oxide Sheets and Polycations. *Chem. Mater.* **1999**, *11*, 771-778.

85. Hummers Jr, W. S.; Offeman, R. E. Preparation of Graphitic Oxide. *J. Am. Chem. Soc.* **1958**, *80*, 1339-1339.
86. Perdew, J. P.; Burke, K.; Ernzerhof, M. Generalized Gradient Approximation Made Simple. *Phys. Rev. Lett.* **1996**, *77*, 3865.
87. Blöchl, P. E. Projector Augmented-Wave Method. *Phys. Rev. B* **1994**, *50*, 17953.
88. Monkhorst, H. J.; Pack, J. D. Special Points for Brillouin-Zone Integrations. *Phys. Rev. B* **1976**, *13*, 5188.
89. Gao, W.; Alemany, L. B.; Ci, L.; Ajayan, P. M. New Insights into the Structure and Reduction of Graphite Oxide. *Nat. Chem.* **2009**, *1*, 403-408.
90. Choudhuri, I.; Patra, N.; Mahata, A.; Ahuja, R.; Pathak, B. B–N@ Graphene: Highly Sensitive and Selective Gas Sensor. *J. Phys. Chem. C* **2015**, *119*, 24827-24836.
91. J. Moulder, W. Stickle, P. Sobol and K. Bomben, Handbook of X-Ray Photoelectron Spectroscopy, Perkin Elmer, Eden Prairie, MN, 1992.
92. Mathkar, A.; Narayanan, T.; Alemany, L. B.; Cox, P.; Nguyen, P.; Gao, G.; Chang, P.; Romero-Aburto, R.; Mani, S. A.; Ajayan, P. Synthesis of Fluorinated Graphene Oxide and Its Amphiphobic Properties. *Part. Part. Syst. Char.* **2013**, *30*, 266-272.
93. Yang, D.; Velamakanni, A.; Bozoklu, G.; Park, S.; Stoller, M.; Piner, R. D.; Stankovich, S.; Jung, I.; Field, D. A.; Ventrice, C. A. Chemical Analysis of Graphene Oxide Films after Heat and Chemical Treatments by X-Ray Photoelectron and Micro-Raman Spectroscopy. *Carbon* **2009**, *47*, 145-152.

94. Wang, B.; Wang, J.; Zhu, J. Fluorination of graphene: A Spectroscopic and Microscopic Study. *ACS Nano* **2014**, *8*, 1862-1870.

95. Shirasaki, T.; Moguet, F.; Lozano, L.; Tressaud, A.; Nanse, G.; Papirer, E. Fluorination of Carbon Blacks: An X-Ray Photoelectron Spectroscopy Study: IV. Reactivity of Different Carbon Blacks in CF_4 Radiofrequency Plasma. *Carbon* **1999**, *37*, 1891-1900.

96. L'Heureux, A.; Beaulieu, F.; Bennett, C.; Bill, D. R.; Clayton, S.; LaFlamme, F.; Mirmehrabi, M.; Tadayon, S.; Tovell, D.; Couturier, M. Aminodifluorosulfinium Salts: Selective Fluorination Reagents with Enhanced Thermal Stability and Ease of Handling. *J. Org. Chem.* **2010**, *75*, 3401-3411.

97. Dresselhaus, M. S.; Jorio, A.; Hofmann, M.; Dresselhaus, G.; Saito, R. Perspectives on Carbon Nanotubes and Graphene Raman Spectroscopy. *Nano Lett.* **2010**, *10*, 751-758.

98. Timmer, B.; Olthuis, W.; Van Den Berg, A. Ammonia Sensors and Their Applications—A Review. *Sens. Actuators, B* **2005**, *107*, 666-677.

99. Hu, N.; Yang, Z.; Wang, Y.; Zhang, L.; Wang, Y.; Huang, X.; Wei, H.; Wei, L.; Zhang, Y. Ultrafast and Sensitive Room Temperature NH_3 Gas Sensors Based on Chemically Reduced Graphene Oxide. *Nanotechnology* **2013**, *25*, 025502.

100. Bo, Z.; Shuai, X.; Mao, S.; Yang, H.; Qian, J.; Chen, J.; Yan, J.; Cen, K. Green Preparation of Reduced Graphene Oxide for Sensing and Energy Storage Applications. *Sci. Rep.* **2014**, *4*.

101. Zhou, X.; Wang, X.; Wang, B.; Chen, Z.; He, C.; Wu, Y. Preparation, Characterization and NH_3-Sensing Properties of Reduced Graphene Oxide/Copper Phthalocyanine Hybrid Material. *Sens. Actuators, B* **2014**, *193*, 340-348.

102. Su, P.-G.; Yang, L.-Y. NH_3 Gas Sensor Based on Pd/SnO_2/RGO Ternary Composite Operated at Room-Temperature. *Sens. Actuators, B* **2016**, *223*, 202-208.
103. Duy, L. T.; Trung, T. Q.; Dang, V. Q.; Hwang, B. U.; Siddiqui, S.; Son, I. Y.; Yoon, S. K.; Chung, D. J.; Lee, N. E. Flexible Transparent Reduced Graphene Oxide Sensor Coupled with Organic Dye Molecules for Rapid Dual-Mode Ammonia Gas Detection. *Adv. Funct. Mater.* **2016**.
104. Wu, J.; Feng, S.; Wei, X.; Shen, J.; Lu, W.; Shi, H.; Tao, K.; Lu, S.; Sun, T.; Yu, L. Facile Synthesis of 3D Graphene Flowers for Ultrasensitive and Highly Reversible Gas Sensing. *Adv. Funct. Mater.* **2016**, *26*, 7462-7469.
105. Spengler, J. D.; Sexton, K. Indoor Air Pollution: A Public Health Perspective. *Science* **1983**, *221*, 9-17.
106. McManus, N. *Safety and health in confined spaces*. CRC Press: 1998.
107. Takeuchi, T. Oxygen Sensors. *Sens. Actuators, B* **1988**, *14*, 109-124.
108. Xu, W.; Lim, T. S.; Seo, H. K.; Min, S. Y.; Cho, H.; Park, M. H.; Kim, Y. H.; Lee, T. W. N-Doped Graphene Field-Effect Transistors with Enhanced Electron Mobility and Air-Stability. S*mall* **2014**, *10*, 1999-2005.
109. Xu, W.; Seo, H. K.; Min, S. Y.; Cho, H.; Lim, T. S.; Oh, C. y.; Lee, Y.; Lee, T. W. Rapid Fabrication of Designable Large-Scale Aligned Graphene Nanoribbons by Electro-hydrodynamic Nanowire Lithography. *Adv. Mater.* **2014**, *26*, 3459-3464.
110. Xu, W.; Wang, L.; Liu, Y.; Thomas, S.; Seo, H. K.; Kim, K. I.; Kim, K. S.; Lee, T. W. Controllable n-Type Doping on CVD-Grown Single-and Double-Layer Graphene Mixture. *Adv. Mater.* **2015**, *27*, 1619-1623.

111. Li, H.; Yin, Z.; He, Q.; Li, H.; Huang, X.; Lu, G.; Fam, D. W. H.; Tok, A. I. Y.; Zhang, Q.; Zhang, H. Fabrication of Single-and Multilayer MoS2 Film-Based Field-Effect Transistors for Sensing NO at Room Temperature. S*mall* **2012**, *8*, 63-67.
112. Chen, Y.; Xue, X.; Wang, Y.; Wang, T. Synthesis and Ethanol Sensing Characteristics of Single Crystalline SnO_2 Nanorods. *Appl. Phys. Lett.* **2005**, *87*, 233503-233503.
113. Gao, T.; Wang, T. Synthesis and Properties of Multipod-Shaped ZnO Nanorods for Gas-Sensor Applications. *Appl. Phys. A* **2005**, *80*, 1451-1454.
114. Hsueh, T.-J.; Hsu, C.-L.; Chang, S.-J.; Chen, I.-C. Laterally Grown ZnO Nanowire Ethanol Gas Sensors. *Sens. Actuators, B* **2007**, *126*, 473-477.
115. Liang, Y.; Chen, Y.; Wang, T. Low-Resistance Gas Sensors Fabricated from Multiwalled Carbon Nanotubes Coated with a Thin Tin Oxide Layer. *Appl. Phys. Lett.* **2004**, *85*, 666-668.
116. Scott, R. W.; Yang, S.; Chabanis, G.; Coombs, N.; Williams, D.; Ozin, G. Tin Dioxide Opals and Inverted Opals: Near-Ideal Microstructures for Gas Sensors. *Adv. Mater.* **2001**, *13*, 1468-1472.
117. Shimizu, Y.; Egashira, M. Basic Aspects and Challenges of Semiconductor Gas Sensors. *MRS Bullet.* **1999**, *24*, 18-24.
118. Wan, Q.; Li, Q.; Chen, Y.; Wang, T.-H.; He, X.; Li, J.; Lin, C. Fabrication and Ethanol Sensing Characteristics of ZnO Nanowire Gas Sensors. *Appl. Phys. Lett.* **2004**, *84*, 3654-3656.
119. Coleman, J. N.; Lotya, M.; O'Neill, A.; Bergin, S. D.; King, P. J.; Khan, U.; Young, K.; Gaucher, A.; De, S.; Smith, R. J. Two-Dimensional Nanosheets Produced by Liquid Exfoliation of Layered Materials. *Science* **2011**, *331*, 568-571.

120. Kresse, G.; Hafner, J. Ab Initio Molecular Dynamics for Liquid Metals. *Phys. Rev. B* **1993**, *47*, 558.
121. Novoselov, K.; Jiang, D.; Schedin, F.; Booth, T.; Khotkevich, V.; Morozov, S.; Geim, A. Two-Dimensional Atomic Crystals. *Proc. Natl. Acad. Sci. U. S. A.* **2005**, *102*, 10451-10453.
122. Lee, C.; Yan, H.; Brus, L. E.; Heinz, T. F.; Hone, J.; Ryu, S. Anomalous Lattice Vibrations of Single-and Few-Layer MoS_2. *ACS Nano* **2010**, *4*, 2695-2700.
123. Sandoval, S. J.; Yang, D.; Frindt, R.; Irwin, J. Raman Study and Lattice Dynamics of Single Molecular Layers of MoS_2. *Phys. Rev. B* **1991**, *44*, 3955.
124. Liu, Y.; Ding, Y.; Zhang, L.; Gao, P.-X.; Lei, Y. CeO_2 Nanofibers for Insitu O_2 and CO Sensing in Harsh Environments. *RSC Adv.* **2012**, *2*, 5193-5198.
125. Song, H.; Qin, Z.; Gao, F.; Jia, J.; Yang, D.; Hu, X. High Temperature Oxygen Sensing Properties of Oxygen Deficient $RBaCo_2O_{5+\delta}$ Thick Films. *Sens. Actuators, B* **2013**, *177*, 50-54.
126. Lu, C.-C.; Huang, Y.-S.; Huang, J.-W.; Chang, C.-K.; Wu, S.-P. A Macroporous TiO_2 Oxygen Sensor Fabricated Using Anodic Aluminium Oxide as an Etching Mask. *Sensors* **2010**, *10*, 670-683.
127. Ju, L.-T.; Ju, S.-L. Deposition of Ga_2O_3 Thin Film for High-Temperature Oxygen Sensing Applications. *J. Ovonic. Res.* **2012**, *8*, 73-79.
128. Chen, C.-Y.; Chang, K.-H.; Chiang, H.-Y.; Shih, S.-J. Preparation of a Porous Ceria Coating for a Resistive Oxygen Sensor. *Sens. Actuators, B* **2014**, *204*, 31-41.

129. Chen, C.-Y.; Chang, K.-H. Temperature Independent Resistive Oxygen Sensor Prepared Using Zirconia-Doped Ceria Powders. *Sens. Actuators, B* **2012**, *162*, 68-75.
130. Lemmon, E.; McLinden, M.; Friend, D.; Linstrom, P.; Mallard, W. NIST Chemistry Webbook, NIST Standard Reference Database Number 69, National Institute of Standards and Technology, Gaithersburg, MD, 2011, http://www.webbook.nist.gov/chemistry/.
131. Lee, J.; Han, S. Thermodynamics of Native Point Defects in α-Fe_2O_3: An ab Initio Study. *Phys. Chem. Chem. Phys.* **2013**, *15*, 18906-18914.
132. Bollinger, M.; Lauritsen, J.; Jacobsen, K. W.; Nørskov, J. K.; Helveg, S.; Besenbacher, F. One-Dimensional Metallic Edge States in MoS_2. *Phys. Rev. Lett.* **2001**, *87*, 196803.
133. Shim, Y.-S.; Zhang, L.; Kim, D. H.; Kim, Y. H.; Choi, Y. R.; Nahm, S. H.; Kang, C.-Y.; Lee, W.; Jang, H. W. Highly Sensitive and Selective H_2 and NO_2 Gas Sensors Based on Surface-Decorated WO_3 Nanoigloos. *Sens. Actuators, B* **2014**, *198*, 294-301.
134. Comini, E. Metal Oxide Nano-Crystals for Gas Sensing. *Anal. Chim. Acta* **2006**, *568*, 28-40.

국문초록

2차원 물질 기반 화학저항식 가스 감지 특성 연구

사물과 연결된 모든 사용자 및 기기와 정보교환을 가능케 하는 사물인터넷 기술의 발달에 따라 기기의 내외부 정보를 교환하는 스마트센서가 가장 중요한 기술로 자리매김 하고 있다. 특히, 가스 센서는 특정 가스의 존재 및 농도를 검지할 수 있고 인간의 생활, 안전, 건강, 환경, 에너지 절약에 달하는 수많은 영역에 적용 가능하므로 매우 큰 관심을 불러일으키고 있다. 사물인터넷 혹은 차세대 기기에 적용하려면 가스 센서는 저소비전력, 저가격, 소형화, 현존 기술과의 접목이 쉬워야하는 점 등 까다로운 요구사항을 전부 만족시켜야한다. 오늘날까지 반도체성 금속산화물은 대량생산, 소형화, 저가격, 고온에서의 높은 가스 반응성 등 여러 장점 덕분에 가스감지물질로 가장 많이 사용되어왔다. 하지만 여전히 고 소비전력, 외부히터의 사용, 취약한 장기 안정성, 낮은 습도 내구성 등의 주요 문제점 및 거론된 사물인터넷의

요구사항을 해결하지 못한 채, 대체 가능한 가스 감지물질을 탐색하는 연구가 활발히 진행되고 있다.

대안으로 제시되는 물질 중 대표적으로 그래핀, 전이금속 다이칼코게나이드, 금속산화물 나노시트 같은 2 차원 물질들이 가장 많은 관심을 받고 있다. 2 차원 물질들은 고유의 투명성, 유연성, 높은 비표면적, 많은 활성 사이트, 우수한 상온 가스감지 특성 등 독특하고 우수한 장점들로 인해 금속산화물을 대체하고 미래 기술에 적용 가능하다는 평가를 받는다. 표면 기능화, 귀금속 표면장식, 감지 메커니즘의 이해 등을 통해 2 차원 물질 고유 성질의 단점을 개선 및 해결하고, 장점은 극대화할 수 있기 때문에 차세대 가스감지물질로 주목을 받고 있다. 또한 상온 가스감지 특성을 보이며 저가격 대량생산 및 소형화가 쉽고, 기존 기술에 적용하기 쉬운 점 등 실제기기 적용의 요구사항을 만족한다. 하지만 2 차원 물질도 낮은 선택성, 긴 반응시간 및 회복시간, 비가역적 가스감지 특성과 같은 반드시 극복해야 할 약점들을 가지고 있다.

그러므로, 본 논문은 1)자가발열 그래핀 구조, 2)표면 불소화된 그래핀 산화물, 3)액상 박리법으로 제작한 이황화몰리브덴 나노파티클, 위의 세가지 샘플로 준비된 화학저항식 가스 센서의 감지 특성을 제시하며, 이를 통해 외부히터 사용으로 인한 소비전력과 열안정성 문제, 선택성이 낮은 문제, 그리고 아직까지 2 차원 물질에 대한 감지 메커니즘 연구가 잘 되지 않은 점 등을 해결했다. 각 가스 센서의 감지 메커니즘은 밀도 함수 이론을 기반으로 한 제 1 원리 계산을 통해 증명했다.

첫 번째로, 간단한 포토리쏘그래피 공정을 통해 제작 자가발열 그래핀의 가스 감지 특성을 확인하였다. 자가활성된 그래핀 센서는 전극과 감지표면이 모두 그래핀으로 구성됐으며, 별도의 히터 없이도 이산화질소에 대해 고 감도, 고 선택성, 가역적 감지 반응을 보였다. 이론적 감지한계는 약 6.87 ppb 수준으로 계산됐다. 이 센서는 자가활성을 통해 고습의 조건 및 휘어진 형태에서도 안정적인 구동을 보여줄 뿐만 아니라, 손쉬운 제조공정을 기반으로 사물인터넷 및 웨어러블 전자기기 등 차세대 기술에 실제 적용 잠재성을 넓혔다.

두 번째로, 간단한 용액 공정을 통해 표면 불소화 그래핀 산화물의 상온 암모니아 감지 특성을 확인하였다. 불소화 그래핀 산화물 센서는 이산화질소 가스보다 암모니아 가스에 향상된 반응성, 선택성, 가역성을 보여주었으며, 계산적 상온 감지 한계는 6 ppb 정도로 매우 민감했다. 감지 메커니즘에 미치는 불소기의 영향은 제1원리 계산을 통해 검증되었고, 그래핀 산화물에 도핑 된 불소가 근처 산소를 포함하는 기능기들의 전하 분포를 변화시키며 암모니아에 우선 선택적 흡탈착을 유발한다는 것을 밝혔다. 본 연구를 통한 우수한 암모니아 가스 감지 특성과 계산을 통한 가스 분자 흡탈착에 대한 메커니즘 검증은 기능화된 2차원 물질의 실제 가스 센서 적용 가능성을 확장시킨다.

세 번째로, 기계적 박리와 액상박리로 준비된 이황화몰리브덴 마이크로플레이크와 나노파티클의 산소 감지 특성을 분석하였다. 본 실험에서 액상박리 된 나노파티클은 엣지 사이트의 수가 증가하여 높은 감도와 함께 1–100%에 이르는 폭넓은 영역에서 선형적인 산소 반응성을 보였다. 산소의 가역적 반응성에 기여하는 선호 산소 흡착 사이트들은

제1원리 계산으로 확인하였다. 본 연구는 2차원 물질의 표면 배열 형태에 따라 달라지는 가스 감지 메커니즘의 개념정립 역할을 할 뿐만 아니라, 차세대 가스 감지 물질로써 2차원 이황화몰리브덴의 잠재성이 높음을 확인할 수 있는 연구이다.

학번: 2013-20586

성명: 김 연후

Keyword: 2 차원 물질, 그래핀, 화학저항식 가스센서, 사물인터넷, 제 1 원리 계산